IJCOE
INTERNATIONAL JOURNAL OF
COASTAL, OFFSHORE & ENVIRONMENTAL ENGINEERING

ISSN: 2980-4731 (online)

International Journal of Coastal, Offshore & Environmental Engineering

Since 2016

Volume 9 | Issue 1 | Feb 2024

International Journal of Coastal, Offshore and Environmental Engineering (IJCOE)

Vol. 9 / Issue. 1 / Feb 2024

www.ijcoe.org info@ijcoe.org 34 Volume 9 | Issue 1 | Feb 2024

International Journal of Coastal, Offshore & Environmental Engineering
Since 2015
ISSN: 2980-8721 (online)

In The Name of God

Message from the Editor-in-Chief

The IJCOE journal office was established in 2015,and its first issue was published in 2016. TheIJCOE covers a wide range of research in thefields of oceanography & ocean technology, aswell as marine industries & marine engineering.The editorial board of IJCOE consists of nearly130 of the greatest scientists and researchersfrom over 30 countries worldwide, and thejournal's review board comprises 1,000 membersfrom all five continents. The membership andapplication process for joining the editorial andreview boards of this journal is ongoing. IJCOE isa research-academic quarterly journal that haspublication and distribution permissions fromthe Press Organization and permission topublish scientific-research articles from theMinistry of Science, Research, and Technology(MSRT) with an "A" rating. It also holds a "Q1"rating from the ISC institute with an impactfactor (IF) of approximately 0.43 and isconsidered a "core journal" (prestigious andoutstanding journal). IJCOE is an open-accessjournal and allows the download and receipt ofaccepted articles in full text for free. It respectsand adheres to copyright and COPE regulations.The journal's office operates 24/7, providingservices to researchers. In addition to publishinga regular quarterly journal, IJCOE has 16 specialissues on specific topics in preparation. It alsoprovides conditions for publishing specializedbooks, references, and handbooks. Moreover, itis ready to cooperate with the secretariats ofreputable international conferences to publishtheir selected and outstanding articles. IJCOEevaluates, appraises, and publishes books,articles, and the scientific achievements andfindings of esteemed researchers and scientistsworldwide who are innovating and conductingin-depth research in the "important and strategicfield of the maritime technology & Oceanengineering." It welcomes any form of jointcooperation with universities, research institutes,and related research centers at the national,regional, and international levels, and extends ahand for collaboration.

Classification of Editorial Board in IJCOE

Editor-in-Chief

Director-in-Chief

Deputy Editor

Executive Managers

English Text Editor

Technical Editor

International Editorial Board

National Editorial Board

Editorial Board Associate

Editorial Board Assistant

Guest Editorial Board

Advisory Board

Administrative Coordinator

Honorary Board Member

Methodology Advisor

Author Benefits

- Open Access
- Rapid Publication
- Thorough Peer-Review
- No Copyright Constraints
- Coverage by Leading Indexing Services
- Discounts On Article Processing Charges (APC)
- No Space Constraints, No restriction on the maximum length of the papers, number of figures or colors

INTERNATIONAL JOURNAL OF IJCOE COASTAL, OFFSHORE & ENVIRONMENTAL ENGINEERING

Aims of IJCOE

Hydrodynamics

Marine equipment

Structural mechanics

Ocean environmental predictions

Stochastic calculations Experimental

Automatic Control of Marine Systems

Scope of IJCOE

Marine Hazards

Ocean Acoustics

Naval Architecture

Ocean Engineering

Coastal Engineering

Marine Meteorology

Marine Earth Sciences

Underwater Technology

Marine Renewable Energy

Polar & Arctic Engineering

Marine Renewable Energy

Marine Geography & Geodesy

Marine Environmental Engineering

Automatic Control of Marine Systems

Hydro Physics & Physical Oceanography

Type of papers

- Case Studies
- Book Reviews
- Review Article
- Letters to the Editor
- Methodology Papers
- Editorials and Commentaries
- Response or Rejoinder Papers
- Perspective or Opinion Papers
- Conceptual or Theoretical Papers
- Meta-Analysis and Systematic Reviews
- Short Communications or Brief Reports
- Research Articles (Original Research Papers)

Scientific Research Journal

Ministry of Science, Research And Technology (MSRT)

Jurnal Ranking 2023: A

Ministry Of Science, Research And Technology (ISC)

Citation Impact 2022: 0.429

Quartile 2022 : Q1

Core Collection

IJCOE is a Member of

Cantact Us

Office 1 | Research Institute of Meteorology and Atmospheric Science

Address | Tehran, Shahid Kharrazi Highway, Pajoohesh Blvd, Research Institute of Meteorology and Atmospheric Science, Sand and Dust Storm International Research Center (SDS-IRC), No. 13, 1st floor.

Phone | +982144787652

Postal code | 13611-14977

website | www.rimac.ac.ir

Office 2 | Iranian National Institute for Oceanography and Atmospheric Science

Address | Tehran, Dr. Fatemi Gharbi St., Shahid Etemadzade St., No. 3, third floor.

Phone | +982166944873

Postal code | 13389 – 14118

website | www.inio.ac.ir

Email | Info@ijcoe.org

Website | www.ijcoe.org

Follow Us

www.ijcoe.org

INTERNATIONAL JOURNAL OF IJCOE COASTAL, OFFSHORE & ENVIRONMENTAL ENGINEERING

Volume & Issue:

Volume 9, Issue 1, February 2024

Number of Articles: 6

Content

INTERNATIONAL JOURNAL OF
COASTAL. OFFSHORE & ENVIRONMENTAL ENGINEERING IJCOE Vol.9 /No.1 / winter 2024(1-24)

vailable online at: www. Ijcoe.org Manuscript Type: Original Research Article

A New Look at the Vertical Shear of the Geostrophic Current Part II: Thermal Current and Saline Current

Mohammad Taghi Zamanian

Member of Iranian Society of Marine Science and Technology (ISMST); zamanianmohammadtaghi@gmail.com

ARTICLE INFO

Article History:
Received: 14 Jan. 2024
Accepted: 09 Mar. 2024

Keywords:
Thermohaline circulation
Sensible heat transfer
Deep sea dynamics
Marine ecosystem
World climate balance

ABSTRACT

Many appropriate and necessary phenomena and mechanisms have essential roles for transfer and diffusion of arriving solar radiation. from tropical regions to high latitudes and low latitudes.
Atmospheric movements (winds) and oceanic movements (currents) are some parts of these mechanisms. Even different shear of them (movements) including vertical shear of them; have basic roles in the subject.
Our goal in this research is familiarizing with oceanic efforts for transfer of sensible heat via thermal current and saline current those are special cases of dense current and those are vertical shear of geostrophic current.
In connection with the subject; three versions of thermal current and three versions of saline current were introduced in Cartesian coordinates system and pressure coordinates system.
Furthermore; other subjects related to thermal current and saline current. have been discussed expanded upon the research. Also. study of thermal current and saline current can enlighten deep sea dynamics and help to better understanding climate of deep oceans.
Overall. these currents play a vital role in the ocean's ecosystem. climate and weather patterns. and human activities. They also have a major influence on the distribution of heat. carbon and other elements in the ocean. and they support marine life. Understanding these currents is important for managing resources and predicting future changes in the ocean's environment.

1. Introduction

In part I of "*A New Look at the Vertical Shear of the Geostrophic Current: Dense Current*" we referred to some theoretical aspects about vertical shear of the geostrophic current and number of basic ideas in connection with definition and deriving formulae to describe "*Dense Current*". [1]
Also. we pointed out majority of incoming solar radiation enter at tropical regions of the earth. Absorbed solar heat in tropical region. transfers or diffuses via some mechanisms. to high latitudes in northern hemisphere and low latitudes in southern hemisphere. The most important of these mechanisms are: winds. ocean currents. sensible heat. latent heat. monsoon phenomenon (as other type of latent heat transfer). tropical cyclones. meridional overturning circulation. Rossby waves and Antarctic circumpolar current.
These essential mechanisms; are agents of produce other sub-mechanisms or phenomena themselves too; those have a special role for heat transfer or heat diffusion directly or indirectly.
Especially; all atmospheric or oceanic movements. have a specific role or diverse roles for transferring heat from tropical regions to other parts of the earth. Even. variation of these movements. so that. assessed in this manner. For instance; variations of wind in vertical direction and variations of oceanic current with respect to depth; are inside of these struggles those arrived heat in the earth. doesn't remain in one region and transferred or diffused to another regions in order to earth will be usable for living human beings and other living beings.
Although variation of wind with respect to height investigated many times and. in this field. observational studies as well as researches have been

done since the beginning of the last century; variation of oceanic currents with respect to depth have been rarely investigated. For instance; recently. Zamanian introduced dense wind [2] and. thermal wind and moist wind [3] as results of vertical shear of geostrophic wind and showed how light air. dense air. heat or moisture advects in atmosphere to discover response time for returning of the; thermodynamic equilibrium.

Now. it is necessary to do researches and observational studies in this important field. i.e.. variations of oceanic currents with respect to depth. [1]

In the first place. variation of oceanic current is used for detection of advection of light or heavy seawater; and in the second stage. it helps to verify current observation and in the third place. detecting oceanic phenomenon type. because vertical shear of oceanic current will be happened in condition that ocean water is baroclinic and in this circumstance; we can track returning the oceanic thermodynamic equilibrium.

Now. some important points of part I are as follows:

1 – 1 – Theoretical study of vertical shear of the oceanic current is an urgent need for careful studies. to decipher many oceanic phenomena.

1 – 2 – We pointed out that various sensible heat flux or salinity flux can lead to produce baroclinic oceans and in turn; variation of geostrophic current in vertical direction. Furthermore. there is direct interaction between heat or salinity flux with current shear.

1 – 3 – After some description of geostrophic current; reason of variation of geostrophic current with respect to depth showed by logical argument and figure 1.

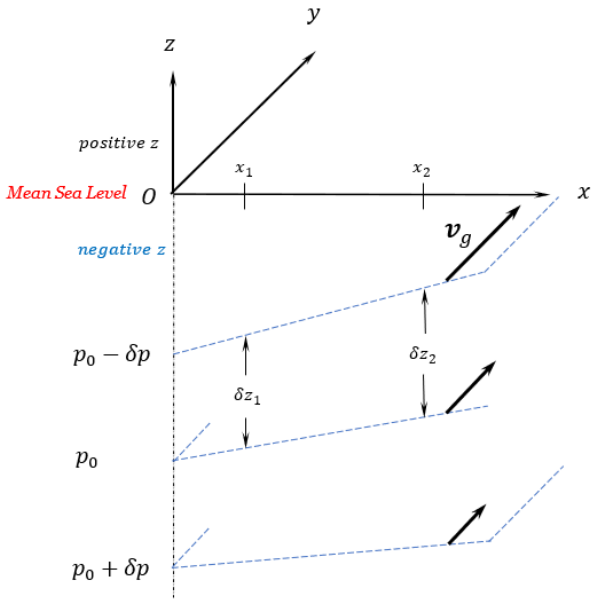

Figure 1. Relationship between vertical shear of the geostrophic current and horizontal thickness gradients. (Note that $0 < \delta p$) [1]

In subsequent time; we propounded pre-assumptions for dense current and focus to movement obtains power from horizontal gradient of density solely. In this manner; we excluded wind driven current. Ekman spiral. tidal current and river outflows. Likewise. we emphasized this current should start only by baroclinic ocean not other forces. Therefore; one can categorize dense current as deep current of ocean frequently.

Afterward; we defined "*Dense Current*" as**:**

"*Dense current is vectorial difference of geostrophic current vector at upper level and geostrophic current vector at lower level*" (of the oceanic layer). [see figure 2] providing no more forces to produce oceanic current same as wind. tidal force or river outflow exception horizontal gradient of density; that is:

$$\mathbb{v}_{\mathrm{D_c}} \equiv \mathbb{v}_{g(z_{2_a})} - \mathbb{v}_{g(z_{1_a})} \qquad \text{(1-Dc)}$$

where in equation (1-Dc) $\mathbb{v}_{\mathrm{D_c}}$ stands for dense current vector. $\mathbb{v}_{g(z_{2_a})}$ is geostrophic current at upper level (at less depth). and $\mathbb{v}_{g(z_{1_a})}$ is geostrophic current at lower level (at more depth) where z_{2_a} refers to level with less depth and z_{1_a} refers to level with more depth. i.e.. $z_{1_a} < z_{2_a}$. [see figure 2]

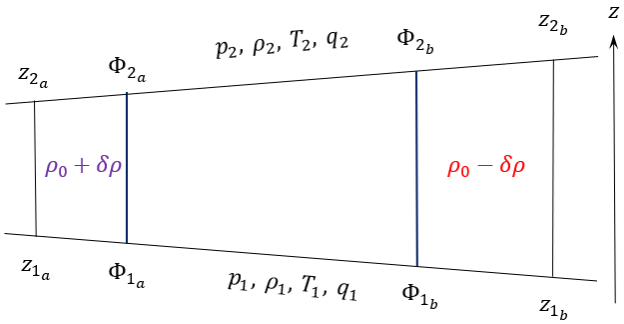

Figure 2. Typical cross section of atmospheric or oceanic layer. [1]

According to definition (1-Dc); eastward and northward components of dense current can be shown as following:

$$u_{\mathrm{D_c}} = u_{g(z_{2_a})} - u_{g(z_{1_a})} \qquad \text{(2-Dc-a)}$$

and

$$v_{\mathrm{D_c}} = v_{g(z_{2_a})} - v_{g(z_{1_a})} \qquad \text{(2-Dc-b)}$$

where in equation (2-Dc-a). $u_{\mathrm{D_c}}$ is eastward component of dense current. $u_{g(z_{2_a})}$ is eastward component of geostrophic current in less depth and $u_{g(z_{1_a})}$ is eastward component of geostrophic current in more depth.

In this manner; in equation (2-Dc-b). $v_{\mathrm{D_c}}$ is northward component of dense current. $v_{g(z_{2_a})}$ is northward component of geostrophic current in less depth and $v_{g(z_{1_a})}$ is northward component of geostrophic current in more depth.

Despite its name; dense current. while a vector. is not a true current. Instead. it is a geostrophic current shear. representing the change of geostrophic current with respect to depth (or height). causing some advections.

In the condition that wind blows on ocean surface; if environment is baroclinic. geostrophic current shear can obtain power from Ekman spiral as well as baroclinity[1] of domain. and variation of geostrophic current with respect to depth is resultant of both forces. In this condition; force of Ekman spiral – especially in less depth – has more power naturally; and furthermore. transfer of momentum from atmosphere to ocean frustrates geostrophic theory. However. in this work we assume wind doesn't blow on ocean surface and variations of geostrophic current with respect to depth. obtains power from baroclinity of domain solely. Particularly; this subject is true for neighborhood of 30 degrees latitudes both in northern hemisphere and southern hemisphere. when there is no atmospheric system and wind doesn't blow. Of course; observations should confirm this phenomenon.

Ekman spiral – dense current interaction is more precise discussion that is not the case for this work. and now we proceed to explain dense current only; on the conditions those are:

1 – 4 – Assuming that wind doesn't blow over ocean;

1 – 5 – Assuming that no more tidal force i.e.. in amphidromic region;

1 – 6 – Assuming that no more river's outflow;

1 – 7 – Assuming that no more other current in ocean's depths and

1 – 8 – Assuming the current is geostrophic and variation of geostrophic current with respect to depth enforces form baroclinic ocean only. (This case is true in the neighborhoods of latitudes -30 and +30. (But it should examine by observations.)

The above-mentioned assumptions are basics and true in the complete of this article.

1 – 9 – Furthermore. with using a number of formulae from a few text books same as text books of Pedlosky [4]. Holton and Hakim [5]. Apel [6]. Marshal and Plumb [7]. Gill [8]. Pedlosky [9]. Ghil and Simonnet [10] and Simmons [11]; we derived three versions of dense current's equations. vectors and components. [1]

1 – 10 – For the first version of dense current; dense current equation was:

$$\frac{\partial \mathbb{v}_g}{\partial z} = -\frac{g}{\rho f}(\mathbb{k} \times \nabla\rho) \qquad (3\text{-Dc-I})$$

We name equation (3-Dc-I) as the ***First version of dense current equation.*** Where in equation (3-Dc-I). $\mathbb{v}_g$ is geostrophic current. z is vertical axis of Cartesian coordinate system. g is acceleration due to gravity. ρ is density of seawater. f is Coriolis parameter. $\mathbb{k}$ stands for vertical unit vector in Cartesian coordinates system and ∇ is gradient operator in this coordinates system.

Equation (3-Dc-I) shows when geostrophic current can change in vertical direction. or when we have dense current that; we have horizontal gradient of density. In other word; in the case. ocean medium should be baroclinic.

Hereafter. we refer to z_1 as level with more depth of the oceanic layer and to z_2 as level with less depth of the oceanic layer. i.e.. $z_1 < z_2$.

Furthermore; we can derive ***the first version of dense current vector*** by integration of equation (3-Dc-I) from higher depth z_1 to lower depth z_2 in vertical direction as following: (by pay attention to figure 2)

$$\mathbb{v}_{D_{c_I}} = -\frac{g}{f}\int_{z_1}^{z_2}\frac{1}{\rho}(\mathbb{k} \times \nabla\rho)dz \qquad (4\text{-Dc-I})$$

In equation (4-Dc-I) or equation for the first version of dense current vector; $\mathbb{v}_{D_{c_I}}$ is the first version of dense current vector. z_1 is lower level of oceanic layer. z_2 is higher level of oceanic layer. ∇ is gradient operator and other parameters defined after equation (3-Dc-I). For equation (4-Dc-I) – that is the equation of the first version of dense current vector – we used definition (1-Dc).

Eastward and northward components of the first version of dense current were:

$$u_{D_{c_I}} = \frac{g}{f}\int_{z_1}^{z_2}\frac{1}{\rho}\frac{\partial\rho}{\partial y}dz \qquad (5\text{-Dc-I-a})$$

and:

$$v_{D_{c_I}} = -\frac{g}{f}\int_{z_1}^{z_2}\frac{1}{\rho}\frac{\partial\rho}{\partial x}dz \qquad (5\text{-Dc-I-b})$$

where in equation (5-Dc-I-a) $u_{D_{c_1}}$ is eastward component of the first version of dense current and in equation (5-Dc-I-b) $v_{D_{c_1}}$ is northward component of the first version of dense current. In addition. we used definitions (2-Dc-a) and (2-Dc-b) for deriving these formulae.

From the first version of dense current vector or its components; one can find out that:

1 – 10 – A: Whatever we go from pole to equator. dense current becomes stronger[2];

1 – 10 – B: If the oceanic layer has more thickness; then dense current becomes more powerful;

1 – 10 – C: Whatever oceanic layer is near to ocean surface. density would be lower and dense current becomes stronger as a result. and

1 – 10 – D: If the horizontal gradient of density would be greater. dense current becomes more powerful. because dense current is proportional to the horizontal gradient of density.

[1] Baroclinity is "*the existence of horizontal gradient of density.*" For oceanic medium; the horizontal gradient of density is related to the horizontal gradient of temperature. the horizontal gradient of salinity or the horizontal gradient of pressure; in general. all of them.

[2] Use of geostrophic current in tropical regions must be with careful deliberation because geostrophic current in these regions is magnified and especially on equator is meaningless.

In this manner. the first version of dense current vector. i.e.. equation (4-Dc-I) shows that: "*The first version of dense current flows parallel to Isopycnals. so that. low density is located at the right side of downstream.*" (In the northern hemisphere)
Furthermore; In this case. counterclockwise turning of geostrophic current with respect to depth (backing) is associated with lower density of seawater advection by geostrophic current in the layer.
In other words; backing of geostrophic current with respect to depth associated with advection of lower density of seawater – that may be from warmer or fresher seawater – in the oceanic layer.
Conversely; clockwise turning of geostrophic current with respect to depth (veering) implies advection of seawater with higher density by geostrophic current in the oceanic layer. In other words; veering of geostrophic current with respect to depth associated with advection of seawater with higher density – that may be from colder or saltier seawater – in the oceanic layer. [1]
1 – 11 – For the second version of dense current; dense current equation was:

$$\mathbb{v}_{\mathrm{D}_{\mathrm{c_{II}}}} = -\frac{1}{f}\int_{z_1}^{z_2}\frac{1}{\rho}(\mathbb{k}\times\nabla\rho)\,d\Phi \qquad \text{(4-Dc-II)}$$

In equation (4-Dc-II) that is: <u>*The second version of dense current vector*</u>: $\mathbb{v}_{\mathrm{D}_{\mathrm{c_{II}}}}$ is the second version of dense current vector. f is Coriolis parameter. z_1 is depth of lower level of oceanic layer. z_2 is depth of higher level of oceanic layer. ρ is density of seawater. $\mathbb{k}$ is vertical unit vector in Cartesian coordinates system. ∇ is gradient operator in Cartesian coordinates system and Φ is geopotential. Equation (4-Dc-II) is the second version of equation of dense current vector and we have used definition (1-Dc) for extracting it.
Eastward and northward components of the second version of dense current were:

$$u_{\mathrm{D}_{\mathrm{c_{II}}}} = \frac{1}{f}\int_{z_1}^{z_2}\frac{1}{\rho}\frac{\partial\rho}{\partial y}d\Phi \qquad \text{(5-Dc-II-a)}$$

and:

$$v_{\mathrm{D}_{\mathrm{c_{II}}}} = -\frac{1}{f}\int_{z_1}^{z_2}\frac{1}{\rho}\frac{\partial\rho}{\partial x}d\Phi \qquad \text{(5-Dc-II-b)}$$

where in equation (5-Dc-II-a). $u_{\mathrm{D}_{\mathrm{c_{II}}}}$ is eastward component of the second version of dense current and we have used definition (2-Dc-a) for deriving it. And in equation (5-Dc-II-b). $v_{\mathrm{D}_{\mathrm{c_{II}}}}$ is northward component of the second version of dense current and we have used definition (2-Dc-b) for extracting this equation.

All specifications. properties and figures of the second version of dense current are the same as the first version of dense current approximately. [1]
1 – 12 – For the third version of dense current; dense current vector was:

$$\mathbb{v}_{\mathrm{D}_{\mathrm{c_{III}}}} = f^{-1}\mathbb{k}\times\nabla_p(\Phi_2-\Phi_1) \qquad \text{(4-Dc-III)}$$

where. in equation (4-Dc-III). $\mathbb{v}_{\mathrm{D}_{\mathrm{c_{III}}}}$ is: <u>*The third version of dense current vector*</u>. f is Coriolis parameter. $\mathbb{k}$ is vertical unit vector in pressure coordinates system[3]. ∇_p is gradient operator in pressure coordinates system. Φ_2 is geopotential of higher level of the oceanic layer. Φ_1 is geopotential of lower level of the oceanic layer and $(\Phi_2-\Phi_1)$ is geopotential thickness of the oceanic layer.
Also; eastward component of the third version of dense current is:

$$u_{\mathrm{D}_{\mathrm{c_{III}}}} = -\frac{1}{f}\frac{\partial}{\partial y}(\Phi_2-\Phi_1) \qquad \text{(5-Dc-III-a)}$$

In equation (5-Dc-III-a). $u_{\mathrm{D}_{\mathrm{c_{III}}}}$ is eastward component of the third version of dense current and we used definition (2-Dc-a) for deriving this equation.
And northward component of the third version of dense current is:

$$v_{\mathrm{D}_{\mathrm{c_{III}}}} = \frac{1}{f}\frac{\partial}{\partial x}(\Phi_2-\Phi_1) \qquad \text{(5-Dc-III-b)}$$

In equation (5-Dc-III-b). $v_{\mathrm{D}_{\mathrm{c_{III}}}}$ is northward component of the third version of dense current and we used definition (2-Dc-b) for deriving this equation.
From the third version of dense current vector or its components; one can find out that:
1 – 12 – A: Whatever we go from pole to equator. the third version of dense current becomes stronger (with pay attention to footnote No. 2)
1 – 12 – B: If the oceanic layer has more geopotential thickness; then the third version of the dense current becomes more powerful. and
1 – 12 – C: If the horizontal gradient of geopotential thickness of the oceanic layer would be greater; then the third version of the dense current becomes more powerful. because this version of dense current is proportional to the horizontal gradient of geopotential thickness.
In this manner. the third version of dense current vector. i.e.. equation (4-Dc-III) shows that: "*The third version of dense current flows parallel to isopleths of geopotential thickness of the oceanic layer so that. high thickness of the layer is located at the right side of downstream.*" (In the northern hemisphere)

[3] In this work; whenever we refer to *"pressure coordinates system*" our purpose is "*Cartesian coordinates system with pressure as vertical coordinate"*. Note this coordinates system is "*Left-handed system*" and some text book referred to it as "*Isobaric coordinates system*"

In connection with the third version of dense current; counterclockwise turning of geostrophic current with respect to depth (backing) is associated with more thickness of oceanic layer advection by geostrophic current in the layer.
And; clockwise rotation of geostrophic current with respect to depth (veering) implies advection of less thickness of oceanic layer.
Therefore. it is possible to obtain a reasonable estimate of the horizontal advection of oceanic layer thickness and its vertical dependence at a given location solely from data on the vertical profile of the current given by current meter. Alternatively. the geostrophic current at any level of the oceanic layer can be estimated from the advection of less or more thickness of oceanic layer. provided that the geostrophic velocity is known at other level of that oceanic layer. [1]
Dense current is outstanding example of thermohaline circulation. Because. thermohaline circulation is the circulation of ocean water that is driven by differences in water density.
Now. following part I; in this part; we focus on special cases of dense current.

2. Special cases of Dense Current

The equation of state of seawater shows seawater density is depended on salinity. temperature and pressure. i.e.: [1]. [6]. [8]. [12] and [13]

$$\rho = \rho(s.T.p) \tag{6}$$

Equation of state for seawater is introduced in many texts same as [6]. [8] and [13] from origin [14] by following equation:

$$\rho = \rho(s.T.p) = \frac{\rho(s.T.0)}{1 - {}^{p}/_{K_T(s.T.p)}} \tag{7}$$

where in equation (7). ρ is density of seawater measuring by kgm^{-3}. s is salinity of seawater measuring by psu. T is temperature of seawater measuring by Celsius degrees ℃. p is pressure of seawater at defined level (depth) measuring by bar (10^5 Pa = $10^5 \mathrm{Nm}^{-2}$ = 1 bar). $K_T = K_T(s.T.p)$ is the mean bulk modulus which is inversely proportional to the compressibility of seawater and 0 in $\rho(s.T.0)$ refers to zero pressure at ocean surface. Each quantity on the right-hand side of (7). except pressure. is expressed as a polynomial series in s and T. expanded about values for zero salinity and a pressure of 1 bar.
The seawater density at the surface pressure ($p = 0$) is given by polynomial form:

$$\rho(s.T.0) = A + Bs + Cs^{3/2} + Ds^2 \tag{8}$$

And the mean bulk modulus is given by:

$$K_T(s.T.p) = E + Fs + Gs^{3/2} + \left(H + Is + Js^{3/2}\right)p + (M + Ns)p^2 \tag{9}$$

The coefficients $A.B.\ldots N$ in (8) and (9) are polynomial up to fifth degree in temperature. [14] The equation of state for seawater is very complicated and has accuracy about $0.009\ \mathrm{kgm}^{-3}$ over the entire oceanic pressure range. Some text introduces simple empirical expression for this equation. anyhow. [12]
The coefficients of polynomials are described as following:

$$A = 9.99842594 \times 10^2 + 6.793952 \times 10^{-2}T - 9.095290 \times 10^{-3}T^2 + 1.001685 \times 10^{-4}T^3 - 1.120083 \times 10^{-6}T^4 + 6.536332 \times 10^{-9}T^5 \tag{10}$$

$$B = 8.24493 \times 10^{-1} - 4.0899 \times 10^{-3}T + 7.6438 \times 10^{-5}T^2 - 8.2467 \times 10^{-7}T^3 + 5.3875 \times 10^{-9}T^4 \tag{11}$$

$$C = -5.72466 \times 10^{-3} + 1.0227 \times 10^{-4}T - 1.6546 \times 10^{-6}T^2 \tag{12}$$

$$D = 4.8314 \times 10^{-4} \tag{13}$$

$$E = 1.965221 \times 10^4 + 1.484206 \times 10^2T - 2.327105T^2 + 1.360477 \times 10^{-2}T^3 - 5.155288 \times 10^{-5}T^4 \tag{14}$$

$$F = 5.46746 \times 10^1 - 6.03459 \times 10^{-1}T + 1.09987 \times 10^{-2}T^2 - 6.1670 \times 10^{-5}T^3 \tag{15}$$

$$G = 7.944 \times 10^{-2} + 1.6483 \times 10^{-2}T - 5.3009 \times 10^{-4}T^2 \tag{16}$$

$$H = 3.239908 + 1.43713 \times 10^{-3}T + 1.16092 \times 10^{-4}T^2 - 5.77905 \times 10^{-7}T^3 \tag{17}$$

$$I = 2.2838 \times 10^{-3} - 1.0981 \times 10^{-5}T - 1.6078 \times 10^{-6}T^2 \tag{18}$$

$$J = 1.91075 \times 10^{-4} \tag{19}$$

$$M = 8.50935 \times 10^{-5} - 6.12293 \times 10^{-6}T + 5.2787 \times 10^{-8}T^2 \tag{20}$$

and:

$$N = -9.9348 \times 10^{-7} + 2.0816 \times 10^{-8}T + 9.1697 \times 10^{-10}T^2 \tag{21}$$

In part I of "*A New Look at the Vertical Shear of Geostrophic Current: Dense Current*" we referred to eastward and northward components of the first version of dense current as following [1]:

$$u_{\mathrm{D_{c_I}}} = \frac{g}{f}\int_{z_1}^{z_2} \frac{1}{\rho}\frac{\partial \rho}{\partial y}dz \tag{5-Dc-I-a}$$

and:

$$v_{\mathrm{D}_{\mathrm{c_I}}} = -\frac{g}{f}\int_{\mathrm{z}_1}^{\mathrm{z}_2}\frac{1}{\rho}\frac{\partial\rho}{\partial x}dz \qquad \text{(5-Dc-I-b)}$$

At the present time; we substitute equivalent of density ρ from equations (8) and (9) by substituting coefficients introduced in equations (10) – (21) into equation (5-Dc-I-a) and get:

$$u_{\mathrm{D}_{\mathrm{c_I}}} = \frac{g}{f}\int_{\mathrm{z}_1}^{\mathrm{z}_2}\frac{1}{\rho}\frac{\partial\rho}{\partial y}dz = \frac{g}{f}\int_{\mathrm{z}_1}^{\mathrm{z}_2}\frac{1}{\frac{\rho(s.T.0)}{1-{}^{p}/_{K_T(s.T.p)}}}\frac{\partial}{\partial y}\left[\frac{\rho(s.T.0)}{1-{}^{p}/_{K_T(s.T.p)}}\right]dz \qquad \text{(22-a)}$$

or:

$$u_{\mathrm{D}_{\mathrm{c_I}}} = \frac{g}{f}\int_{z_1}^{z_2}\frac{1}{\frac{\rho(s.T.0)}{1-{}^{p}/_{K_T(s.T.p)}}}\times\frac{\frac{\partial}{\partial y}\rho(s.T.0)\left[1-{}^{p}/_{K_T(s.T.p)}\right]-\rho(s.T.0)\frac{\partial}{\partial y}\left[1-{}^{p}/_{K_T(s.T.p)}\right]}{\left[1-{}^{p}/_{K_T(s.T.p)}\right]^2}dz \qquad \text{(23-a)}$$

But:

$$\frac{\partial}{\partial y}\left[1-{}^{p}/_{K_T(s.T.p)}\right] = -\frac{\partial}{\partial y}\left[{}^{p}/_{K_T(s.T.p)}\right] = \frac{p\frac{\partial}{\partial y}K_T(s.T.p)-\frac{\partial p}{\partial y}K_T(s.T.p)}{[K_T(s.T.p)]^2} \qquad \text{(24-a)}$$

Accordingly:

$$u_{\mathrm{D}_{\mathrm{c_I}}} = \frac{g}{f}\int_{z_1}^{z_2}\frac{1}{\frac{\rho(s.T.0)}{1-{}^{p}/_{K_T(s.T.p)}}}\times\frac{\frac{\partial}{\partial y}\rho(s.T.0)\left[1-{}^{p}/_{K_T(s.T.p)}\right]-\rho(s.T.0)(24-\mathrm{a})}{\left[1-{}^{p}/_{K_T(s.T.p)}\right]^2}dz \qquad \text{(25-a)}$$

where in equation (25-a). (24-a) refers to equation with the same name.
Now we will proceed every term. one by one.
By aid of equation (8). we have:

$$\frac{\partial}{\partial y}\rho(s.T.0) = \frac{\partial}{\partial y}\left(A+Bs+Cs^{3}/_{2}+Ds^2\right) = \frac{\partial}{\partial y}A+\frac{\partial}{\partial y}(Bs)+\frac{\partial}{\partial y}\left(Cs^{3}/_{2}\right)+\frac{\partial}{\partial y}(Ds^2) \qquad \text{(26-a)}$$

With pay attention to equation (10):

$$\frac{\partial}{\partial y}A = \frac{\partial}{\partial y}(9.99842594\times10^{2}+6.793952\times10^{-2}T-9.095290\times10^{-3}T^2+1.001685\times10^{-4}T^3-1.120083\times10^{-6}T^4+6.536332\times10^{-9}T^5) \qquad (27)$$

Therefore:

$$\frac{\partial}{\partial y}A = 6.793952\times10^{-2}\frac{\partial T}{\partial y}-1.819058\times10^{-2}T\frac{\partial T}{\partial y}+3.005055\times10^{-4}T^2\frac{\partial T}{\partial y}-4.480332\times10^{-4}T^3\frac{\partial T}{\partial y}+3.268166\times10^{-8}T^4\frac{\partial T}{\partial y} \qquad \text{(28-a)}$$

And with pay attention to equation (11):

$$\frac{\partial}{\partial y}(Bs) = \frac{\partial B}{\partial y}s+B\frac{\partial s}{\partial y} = \frac{\partial}{\partial y}(8.24493\times10^{-1}-4.0899\times10^{-3}T+7.6438\times10^{-5}T^2-8.2467\times10^{-7}T^3+5.3875\times10^{-9}T^4)s+(8.24493\times10^{-1}-4.0899\times10^{-3}T+7.6438\times10^{-5}T^2-8.2467\times10^{-7}T^3+5.3875\times10^{-9}T^4)\frac{\partial s}{\partial y} \qquad (29)$$

Consequently:

$$\frac{\partial}{\partial y}(Bs) = \left(-4.0899\times10^{-3}\frac{\partial T}{\partial y}+1.52876\times10^{-4}T\frac{\partial T}{\partial y}-2.47401\times10^{-6}T^2\frac{\partial T}{\partial y}+2.155\times10^{-8}T^3\frac{\partial T}{\partial y}\right)s+(8.24493\times10^{-1}-4.0899\times10^{-3}T+7.6438\times10^{-5}T^2-8.2467\times10^{-7}T^3+5.3875\times10^{-9}T^4)\frac{\partial s}{\partial y} \qquad \text{(30-a)}$$

In addition. by pay attention to equation (12):

$$\frac{\partial}{\partial y}\left(Cs^{3}/_{2}\right) = \frac{\partial C}{\partial y}\left(s^{3}/_{2}\right)+C\frac{\partial}{\partial y}\left(s^{3}/_{2}\right) = \frac{\partial}{\partial y}(-5.72466\times10^{-3}+1.0227\times10^{-4}T-1.6546\times10^{-6}T^2)\left(s^{3}/_{2}\right)+(-5.72466\times10^{-3}+1.0227\times10^{-4}T-1.6546\times10^{-6}T^2)\frac{\partial}{\partial y}\left(s^{3}/_{2}\right) \qquad (31)$$

Accordingly:

$$\frac{\partial}{\partial y}\left(Cs^{3}/_{2}\right) = \left(1.0227\times10^{-4}\frac{\partial T}{\partial y}-3.3092\times10^{-6}T\frac{\partial T}{\partial y}\right)\left(s^{3}/_{2}\right)+(-5.72466\times10^{-3}+1.0227\times10^{-4}T-1.6546\times10^{-6}T^2)\left(\frac{3}{2}\,s^{1}/_{2}\frac{\partial s}{\partial y}\right) \qquad \text{(32-a)}$$

And with pay attention to equation (13):

$$\frac{\partial}{\partial y}(Ds^2) = \frac{\partial}{\partial y}[(4.8314\times10^{-4})s^2] = 9.6628\times10^{-4}s\frac{\partial s}{\partial y} \qquad \text{(33-a)}$$

Therefore. derivative of seawater density at surface of ocean with respect to y. is organized by addition of equations (28-a). (30-a). (32-a) and (33-a). i.e.:

$$\frac{\partial}{\partial y}\rho(s.T.0) = (28-\mathrm{a})+(30-\mathrm{a})+(32-\mathrm{a})+(33-\mathrm{a}) \qquad \text{(34-a)}$$

Furthermore. with aid of equation (9) we have:

$$\frac{\partial}{\partial y}[K_T(s.T.p)] = \frac{\partial}{\partial y}(E) + \frac{\partial}{\partial y}(Fs) + \frac{\partial}{\partial y}\left(Gs^{3}/_{2}\right) + \frac{\partial}{\partial y}(Hp) + \frac{\partial}{\partial y}(Isp) + \frac{\partial}{\partial y}\left(Js^{3}/_{2}p\right) + \frac{\partial}{\partial y}(Mp^2) + \frac{\partial}{\partial y}(Nsp^2) \quad (35\text{-a})$$

And with aid of equation (l4). we have:

$$\frac{\partial}{\partial y}(E) = \frac{\partial}{\partial y}(1.965221 \times 10^4 + 1.484206 \times 10^2 T - 2.327105T^2 + 1.360477 \times 10^{-2}T^3 - 5.155288 \times 10^{-5}T^4) = 1.484206 \times 10^2 \frac{\partial T}{\partial y} - 4.65421T\frac{\partial T}{\partial y} + 4.081431 \times 10^{-2}T^2\frac{\partial T}{\partial y} - 2.0621152 \times 10^{-4}T^3\frac{\partial T}{\partial y} \quad (36\text{-a})$$

With help of equation (15). we get:

$$\frac{\partial}{\partial y}(Fs) = \frac{\partial F}{\partial y}s + F\frac{\partial s}{\partial y} = \frac{\partial}{\partial y}(5.46746 \times 10^1 - 6.03459 \times 10^{-1}T + 1.09987 \times 10^{-2}T^2 - 6.1670 \times 10^{-5}T^3)s + (5.46746 \times 10^1 - 6.03459 \times 10^{-1}T + 1.09987 \times 10^{-2}T^2 - 6.1670 \times 10^{-5}T^3)\frac{\partial s}{\partial y} \quad (37)$$

or:

$$\frac{\partial}{\partial y}(Fs) = \left(-6.03459 \times 10^{-1}\frac{\partial T}{\partial y} + 2.19974 \times 10^{-2}T\frac{\partial T}{\partial y} - 1.8501 \times 10^{-4}T^2\frac{\partial T}{\partial y}\right)s + (5.46746 \times 10^1 - 6.03459 \times 10^{-1}T + 1.09987 \times 10^{-2}T^2 - 6.1670 \times 10^{-5}T^3)\frac{\partial s}{\partial y} \quad (38\text{-a})$$

And with aid of equation (16). we have:

$$\frac{\partial}{\partial y}\left(Gs^{3}/_{2}\right) = \frac{\partial G}{\partial y}s^{3}/_{2} + G\frac{\partial}{\partial y}\left(s^{3}/_{2}\right) = \frac{\partial}{\partial y}(7.944 \times 10^{-2} + 1.6483 \times 10^{-2}T - 5.3009 \times 10^{-4}T^2)s^{3}/_{2} + (7.944 \times 10^{-2} + 1.6483 \times 10^{-2}T - 5.3009 \times 10^{-4}T^2)\frac{\partial}{\partial y}\left(s^{3}/_{2}\right) \quad (39)$$

Therefore:

$$\frac{\partial}{\partial y}\left(Gs^{3}/_{2}\right) = \left(1.6483 \times 10^{-2}\frac{\partial T}{\partial y} - 1.06018 \times 10^{-3}T\frac{\partial T}{\partial y}\right)s^{3}/_{2} + (7.944 \times 10^{-2} + 1.6483 \times 10^{-2}T - 5.3009 \times 10^{-4}T^2)\frac{3}{2}s^{1}/_{2}\frac{\partial s}{\partial y} \quad (40\text{-a})$$

Likewise. with help of equation (17). we get:

$$\frac{\partial}{\partial y}(Hp) = \frac{\partial H}{\partial y}p + H\frac{\partial p}{\partial y} = \frac{\partial}{\partial y}(3.239908 + 1.43713 \times 10^{-3}T + 1.16092 \times 10^{-4}T^2 - 5.77905 \times 10^{-7}T^3)p + (3.239908 + 1.43713 \times 10^{-3}T + 1.16092 \times 10^{-4}T^2 - 5.77905 \times 10^{-7}T^3)\frac{\partial p}{\partial y} \quad (41)$$

Consequently:

$$\frac{\partial}{\partial y}(Hp) = \left(1.43713 \times 10^{-3}\frac{\partial T}{\partial y} + 2.32184 \times 10^{-4}T\frac{\partial T}{\partial y} - 1.733715 \times 10^{-6}T^2\frac{\partial T}{\partial y}\right)p + (3.239908 + 1.43713 \times 10^{-3}T + 1.16092 \times 10^{-4}T^2 - 5.77905 \times 10^{-7}T^3)\frac{\partial p}{\partial y} \quad (42\text{-a})$$

And with assistance of equation (18):

$$\frac{\partial}{\partial y}(Isp) = \frac{\partial I}{\partial y}sp + I\frac{\partial s}{\partial y}p + Is\frac{\partial p}{\partial y} = \frac{\partial}{\partial y}(2.2838 \times 10^{-3} - 1.0981 \times 10^{-5}T - 1.6078 \times 10^{-6}T^2)sp + (2.2838 \times 10^{-3} - 1.0981 \times 10^{-5}T - 1.6078 \times 10^{-6}T^2)\frac{\partial s}{\partial y}p + (2.2838 \times 10^{-3} - 1.0981 \times 10^{-5}T - 1.6078 \times 10^{-6}T^2)s\frac{\partial p}{\partial y} \quad (43)$$

Accordingly:

$$\frac{\partial}{\partial y}(Isp) = \left(-1.0981 \times 10^{-5}\frac{\partial T}{\partial y} - 3.2156 \times 10^{-6}T\frac{\partial T}{\partial y}\right)sp + (2.2838 \times 10^{-3} - 1.0981 \times 10^{-5}T - 1.6078 \times 10^{-6}T^2)\frac{\partial s}{\partial y}p + (2.2838 \times 10^{-3} - 1.0981 \times 10^{-5}T - 1.6078 \times 10^{-6}T^2)s\frac{\partial p}{\partial y} \quad (44\text{-a})$$

And with aid of equation (19):

$$\frac{\partial}{\partial y}\left(Js^{3}/_{2}p\right) = \frac{\partial J}{\partial y}s^{3}/_{2}p + J\frac{\partial\left(s^{3}/_{2}\right)}{\partial y}p + Js^{3}/_{2}\frac{\partial p}{\partial y} = 2.866125 \times 10^{-4}s^{1}/_{2}\frac{\partial s}{\partial y}p + (1.91075 \times 10^{-4})s^{3}/_{2}\frac{\partial p}{\partial y} \quad (45\text{-a})$$

By help of equation (20):

$$\frac{\partial}{\partial y}(Mp^2) = \frac{\partial M}{\partial y}p^2 + M\frac{\partial}{\partial y}(p^2) = \frac{\partial}{\partial y}(8.50935 \times 10^{-5} - 6.12293 \times 10^{-6}T + 5.2787 \times 10^{-8}T^2)p^2 + (8.50935 \times 10^{-5} - 6.12293 \times 10^{-6}T + 5.2787 \times 10^{-8}T^2)\frac{\partial(p^2)}{\partial y} \quad (46)$$

Therefore:

$$\frac{\partial}{\partial y}(Mp^2) = \left(-6.12293 \times 10^{-6}\frac{\partial T}{\partial y} + 1.05574 \times 10^{-7}T\frac{\partial T}{\partial y}\right)p^2 + 2.0 \times (8.50935 \times 10^{-5} - 6.12293 \times 10^{-6}T + 5.2787 \times 10^{-8}T^2)p\frac{\partial p}{\partial y} \quad (47\text{-a})$$

Also. with help of equation (21):

$$\frac{\partial}{\partial y}(Nsp^2) = \frac{\partial N}{\partial y}sp^2 + N\frac{\partial s}{\partial y}p^2 + Ns\frac{\partial}{\partial y}(p^2) = \frac{\partial}{\partial y}(-9.9348 \times 10^{-7} + 2.0816 \times 10^{-8}T + 9.1697 \times 10^{-10}T^2)sp^2 + (-9.9348 \times 10^{-7} + 2.0816 \times 10^{-8}T + 9.1697 \times 10^{-10}T^2)\frac{\partial s}{\partial y}p^2 + 2.0 \times$$

$$(-9.9348 \times 10^{-7} + 2.0816 \times 10^{-8}T + 9.1697 \times 10^{-10}T^2)sp\frac{\partial p}{\partial y} \quad (48)$$

Consequently:

$$\frac{\partial}{\partial y}(Nsp^2) = \left(2.0816 \times 10^{-8}\frac{\partial T}{\partial y} + 1.83394 \times 10^{-9}T\frac{\partial T}{\partial y}\right)sp^2 + (-9.9348 \times 10^{-7} + 2.0816 \times 10^{-8}T + 9.1697 \times 10^{-10}T^2)\frac{\partial s}{\partial y}p^2 + 2.0 \times (-9.9348 \times 10^{-7} + 2.0816 \times 10^{-8}T + 9.1697 \times 10^{-10}T^2)sp\frac{\partial p}{\partial y} \quad (49\text{-a})$$

Therefore; according to equations (35-a). (36-a). (38-a). (40-a). (42-a). (44-a). (45-a). (47-a) and (49-a):

$$\frac{\partial}{\partial y}[K_T(s.T.p)] = \text{(36-a) + (38-a) + (40-a) + (42-a) + (44-a) + (45-a) + (47-a) + (49-a).} \quad (50\text{-a})$$

Furthermore. considering equation (24-a). we have:

$$\frac{\partial}{\partial y}\left[1 - {}^{p}/_{K_T(s.T.p)}\right] = \frac{p\frac{\partial}{\partial y}K_T(s.T.p) - \frac{\partial p}{\partial y}K_T(s.T.p)}{[K_T(s.T.p)]^2} = \frac{p(50\text{-a}) - \frac{\partial p}{\partial y}K_T(s.T.p)}{[K_T(s.T.p)]^2} \quad (51\text{-a})$$

Substituting (34-a) and (51-a) in (25-a) yields:

$$u_{D_{c_I}} = \frac{g}{f}\int_{z_1}^{z_2} \frac{1}{\frac{\rho(s.T.0)}{1-{}^{p}/_{K_T(s.T.p)}}} \times \frac{(34\text{-a})\left[1-{}^{p}/_{K_T(s.T.p)}\right] - \rho(s.T.0)(51\text{-a})}{\left[1-{}^{p}/_{K_T(s.T.p)}\right]^2}dz \quad (52\text{-a})$$

where in equation (52-a). $u_{D_{c_I}}$ is eastward component of the first version of dense current. g is acceleration due to gravity. f is Coriolis parameter. z_1 is lower level of the oceanic layer. z_2 is higher level of the oceanic layer. $\rho(s.T.0)$ is density of surface ocean defined in (8). p is pressure of seawater at any point considered. $K_T(s.T.p)$ is mean bulk modulus defined in (9). (34-a) is equation with the same number and (51-a) is also equation with the same number and z stands for vertical axis of Cartesian coordinates system.

Now; we substitute equivalent of density ρ from equations (8) and (9) by substituting coefficients introduced in equations (10) – (21) into equation (5-Dc-I-b) and get:

$$v_{D_{c_I}} = -\frac{g}{f}\int_{z_1}^{z_2}\frac{1}{\rho}\frac{\partial \rho}{\partial x}dz = -\frac{g}{f}\int_{z_1}^{z_2}\frac{1}{\frac{\rho(s.T.0)}{1-{}^{p}/_{K_T(s.T.p)}}}\frac{\partial}{\partial x}\left[\frac{\rho(s.T.0)}{1-{}^{p}/_{K_T(s.T.p)}}\right]dz \quad (22\text{-b})$$

or:

$$v_{D_{c_I}} = -\frac{g}{f}\int_{z_1}^{z_2}\frac{1}{\frac{\rho(s.T.0)}{1-{}^{p}/_{K_T(s.T.p)}}} \times \frac{\frac{\partial}{\partial x}\rho(s.T.0)\left[1-{}^{p}/_{K_T(s.T.p)}\right] - \rho(s.T.0)\frac{\partial}{\partial x}\left[1-{}^{p}/_{K_T(s.T.p)}\right]}{\left[1-{}^{p}/_{K_T(s.T.p)}\right]^2}dz \quad (23\text{-b})$$

But:

$$\frac{\partial}{\partial x}\left[1 - {}^{p}/_{K_T(s.T.p)}\right] = -\frac{\partial}{\partial x}\left[{}^{p}/_{K_T(s.T.p)}\right] = \frac{p\frac{\partial}{\partial x}K_T(s.T.p) - \frac{\partial p}{\partial x}K_T(s.T.p)}{[K_T(s.T.p)]^2} \quad (24\text{-b})$$

Accordingly:

$$v_{D_{c_I}} = -\frac{g}{f}\int_{z_1}^{z_2}\frac{1}{\frac{\rho(s.T.0)}{1-{}^{p}/_{K_T(s.T.p)}}} \times \frac{\frac{\partial}{\partial x}\rho(s.T.0)\left[1-{}^{p}/_{K_T(s.T.p)}\right] - \rho(s.T.0)(24\text{-b})}{\left[1-{}^{p}/_{K_T(s.T.p)}\right]^2}dz \quad (25\text{-b})$$

where in equation (25-b). (24-b) refers to equation with the same name.

Now. we will proceed every term. one by one.

By aid of equation (8). we have:

$$\frac{\partial}{\partial x}\rho(s.T.0) = \frac{\partial}{\partial x}\left(A + Bs + Cs^{3}/_{2} + Ds^2\right) = \frac{\partial}{\partial x}A + \frac{\partial}{\partial x}(Bs) + \frac{\partial}{\partial x}\left(Cs^{3}/_{2}\right) + \frac{\partial}{\partial x}(Ds^2) \quad (26\text{-b})$$

With similar manner for eastward component of the first version of dense current. we get:

$$\frac{\partial}{\partial x}A = 6.793952 \times 10^{-2}\frac{\partial T}{\partial x} - 1.819058 \times 10^{-2}T\frac{\partial T}{\partial x} + 3.005055 \times 10^{-4}T^2\frac{\partial T}{\partial x} - 4.480332 \times 10^{-4}T^3\frac{\partial T}{\partial x} + 3.268166 \times 10^{-8}T^4\frac{\partial T}{\partial x} \quad (28\text{-b})$$

And:

$$\frac{\partial}{\partial x}(Bs) = \left(-4.0899 \times 10^{-3}\frac{\partial T}{\partial x} + 1.52876 \times 10^{-4}T\frac{\partial T}{\partial x} - 2.47401 \times 10^{-6}T^2\frac{\partial T}{\partial x} + 2.155 \times 10^{-8}T^3\frac{\partial T}{\partial x}\right)s + (8.24493 \times 10^{-1} - 4.0899 \times 10^{-3}T + 7.6438 \times 10^{-5}T^2 - 8.2467 \times 10^{-7}T^3 + 5.3875 \times 10^{-9}T^4)\frac{\partial s}{\partial x} \quad (30\text{-b})$$

Also:

$$\frac{\partial}{\partial x}\left(Cs^{3}/_{2}\right) = \left(1.0227 \times 10^{-4}\frac{\partial T}{\partial x} - 3.3092 \times 10^{-6}T\frac{\partial T}{\partial x}\right)\left(s^{3}/_{2}\right) + (-5.72466 \times 10^{-3} + 1.0227 \times 10^{-4}T - 1.6546 \times 10^{-6}T^2)\left(\frac{3}{2}\,s^{1}/_{2}\frac{\partial s}{\partial x}\right) \quad (32\text{-b})$$

And:

$$\frac{\partial}{\partial x}(D_S^2) = \frac{\partial}{\partial x}[(4.8314 \times 10^{-4})s^2] = 9.6628 \times 10^{-4} s \frac{\partial s}{\partial x} \quad (33\text{-b})$$

Therefore. derivative of seawater density at surface of ocean with respect to x. is organized by addition of equations (28-b). (30-b). (32-b) and (33-b). i.e.:

$$\frac{\partial}{\partial x}\rho(s.T.0) = (28\text{-b}) + (30\text{-b}) + (32\text{-b}) + (33\text{-b}) \quad (34\text{-b})$$

Furthermore. with aid of equation (9) we have:

$$\frac{\partial}{\partial x}[K_T(s.T.p)] = \frac{\partial}{\partial x}(E) + \frac{\partial}{\partial x}(Fs) + \frac{\partial}{\partial x}\left(Gs^{3/2}\right) + \frac{\partial}{\partial x}(Hp) + \frac{\partial}{\partial x}(Isp) + \frac{\partial}{\partial x}\left(Js^{3/2}p\right) + \frac{\partial}{\partial x}(Mp^2) + \frac{\partial}{\partial x}(Nsp^2) \quad (35\text{-b})$$

And with help of equation (l4). we have:

$$\frac{\partial}{\partial x}(E) = \frac{\partial}{\partial x}(1.965221 \times 10^4 + 1.484206 \times 10^2 T - 2.327105T^2 + 1.360477 \times 10^{-2}T^3 - 5.155288 \times 10^{-5}T^4) = 1.484206 \times 10^2 \frac{\partial T}{\partial x} - 4.65421T\frac{\partial T}{\partial x} + 4.081431 \times 10^{-2}T^2\frac{\partial T}{\partial x} - 2.0621152 \times 10^{-4}T^3\frac{\partial T}{\partial x} \quad (36\text{-b})$$

And:

$$\frac{\partial}{\partial x}(Fs) = \left(-6.03459 \times 10^{-1}\frac{\partial T}{\partial x} + 2.19974 \times 10^{-2}T\frac{\partial T}{\partial x} - 1.8501 \times 10^{-4}T^2\frac{\partial T}{\partial x}\right)s + (5.46746 \times 10^1 - 6.03459 \times 10^{-1}T + 1.09987 \times 10^{-2}T^2 - 6.1670 \times 10^{-5}T^3)\frac{\partial s}{\partial x} \quad (38\text{-b})$$

In addition:

$$\frac{\partial}{\partial x}\left(Gs^{3/2}\right) = \left(1.6483 \times 10^{-2}\frac{\partial T}{\partial x} - 1.06018 \times 10^{-3}T\frac{\partial T}{\partial x}\right)s^{3/2} + (7.944 \times 10^{-2} + 1.6483 \times 10^{-2}T - 5.3009 \times 10^{-4}T^2)\frac{3}{2}s^{1/2}\frac{\partial s}{\partial x} \quad (40\text{-b})$$

And:

$$\frac{\partial}{\partial x}(Hp) = \left(1.43713 \times 10^{-3}\frac{\partial T}{\partial x} + 2.32184 \times 10^{-4}T\frac{\partial T}{\partial x} - 1.733715 \times 10^{-6}T^2\frac{\partial T}{\partial x}\right)p + (3.239908 + 1.43713 \times 10^{-3}T + 1.16092 \times 10^{-4}T^2 - 5.77905 \times 10^{-7}T^3)\frac{\partial p}{\partial x} \quad (42\text{-b})$$

Also:

$$\frac{\partial}{\partial x}(Isp) = \left(-1.0981 \times 10^{-5}\frac{\partial T}{\partial x} - 3.2156 \times 10^{-6}T\frac{\partial T}{\partial x}\right)sp + (2.2838 \times 10^{-3} - 1.0981 \times 10^{-5}T - 1.6078 \times 10^{-6}T^2)\frac{\partial s}{\partial x}p + (2.2838 \times 10^{-3} - 1.0981 \times 10^{-5}T - 1.6078 \times 10^{-6}T^2)s\frac{\partial p}{\partial x} \quad (44\text{-b})$$

In addition:

$$\frac{\partial}{\partial x}\left(Js^{3/2}p\right) = \frac{\partial J}{\partial x}s^{3/2}p + J\frac{\partial}{\partial x}\left(s^{3/2}\right)p + Js^{3/2}\frac{\partial p}{\partial x} = 2.866125 \times 10^{-4}s^{1/2}\frac{\partial s}{\partial x}p + (1.91075 \times 10^{-4})s^{3/2}\frac{\partial p}{\partial x} \quad (45\text{-b})$$

And:

$$\frac{\partial}{\partial x}(Mp^2) = \left(-6.12293 \times 10^{-6}\frac{\partial T}{\partial x} + 1.05574 \times 10^{-7}T\frac{\partial T}{\partial x}\right)p^2 + 2.0 \times (8.50935 \times 10^{-5} - 6.12293 \times 10^{-6}T + 5.2787 \times 10^{-8}T^2)p\frac{\partial p}{\partial x} \quad (47\text{-b})$$

Also:

$$\frac{\partial}{\partial x}(Nsp^2) = \left(2.0816 \times 10^{-8}\frac{\partial T}{\partial x} + 1.83394 \times 10^{-9}T\frac{\partial T}{\partial x}\right)sp^2 + (-9.9348 \times 10^{-7} + 2.0816 \times 10^{-8}T + 9.1697 \times 10^{-10}T^2)\frac{\partial s}{\partial x}p^2 + 2.0 \times (-9.9348 \times 10^{-7} + 2.0816 \times 10^{-8}T + 9.1697 \times 10^{-10}T^2)sp\frac{\partial p}{\partial x} \quad (49\text{-b})$$

According to equations (35-b). (36-b). (38-b). (40-b). (42-b). (44-b). (45-b). (47-b) and (49-b):

$$\frac{\partial}{\partial x}[K_T(s.T.p)] = (36\text{-b}) + (38\text{-b}) + (40\text{-b}) + (42\text{-b}) + (44\text{-b}) + (45\text{-b}) + (47\text{-b}) + (49\text{-b}). \quad (50\text{-b})$$

Furthermore. substituting (50-b) into equation (24-b) yields:

$$\frac{\partial}{\partial x}\left[1 - {}^{p}/_{K_T(s.T.p)}\right] = \frac{{}^{p}\frac{\partial}{\partial x}K_T(s.T.p) - \frac{\partial p}{\partial x}K_T(s.T.p)}{[K_T(s.T.p)]^2} = \frac{p(50\text{-b}) - \frac{\partial p}{\partial y}K_T(s.T.p)}{[K_T(s.T.p)]^2} \quad (51\text{-b})$$

Substituting (34-b) and (51-b) in (25-b) yields:

$$v_{D_{c_I}} = -\frac{g}{f}\int_{z_1}^{z_2}\frac{1}{\frac{\rho(s.T.0)}{1 - {}^{p}/_{K_T(s.T.p)}}} \times \frac{(34\text{-b})\left[1 - {}^{p}/_{K_T(s.T.p)}\right] - \rho(s.T.0)(51\text{-b})}{\left[1 - {}^{p}/_{K_T(s.T.p)}\right]^2}dz \quad (52\text{-b})$$

where in equation (52-b). $v_{D_{c_I}}$ is northward component of the first version of dense current. g is acceleration due to gravity. f is Coriolis parameter. z_1 is lower level of the oceanic layer. z_2 is higher level of the oceanic layer. $\rho(s.T.0)$ is density of surface ocean defined in (8). p is pressure of seawater at any point considered. $K_T(s.T.p)$ is mean bulk modulus defined in (9). (34-b) is equation with the same number and (51-b) is also

equation with the same number and z stands for vertical axis of Cartesian coordinates system.

2.1. First special case of dense current: Thermal Current

We know that baroclinity of seawater is depending on horizontal gradient of seawater density. But if:

$$s = constant \text{ or } \left(\frac{\partial s}{\partial x} = 0 \ \wedge \ \frac{\partial s}{\partial y} = 0\right) \qquad (53\text{-}1)$$

and

$$p = constant \text{ or } \left(\frac{\partial p}{\partial x} = 0 \ \wedge \ \frac{\partial p}{\partial y} = 0\right) \qquad (53\text{-}2)$$

then. baroclinity of seawater related only to the horizontal gradient of seawater temperature.

By existing conditions (53-1) and (53-2). horizontal gradient of seawater temperature causes to produce baroclinity of ambience solely.

In these conditions; i.e.. conditions (53-1) and (53-2); the variation of density in the horizontal direction is merely related to variation of seawater temperature in horizontal direction causing baroclinity of the ocean. In these circumstances. we define the vectorial difference of geostrophic current vector at upper level and geostrophic current vector at lower level of the oceanic layer as. *Thermal Current*. i.e.:

$$\mathbb{v}_{\mathrm{T_c}} \equiv \mathbb{v}_{g(z_2)} - \mathbb{v}_{g(z_1)} \qquad (1\text{-Tc})$$

where in Equation (1-Tc) $\mathbb{v}_{\mathrm{T_c}}$ stands for thermal current vector. $\mathbb{v}_{g(z_2)}$ is geostrophic current at upper level of the oceanic layer (at less depth). and $\mathbb{v}_{g(z_1)}$ is geostrophic current at lower level of the oceanic layer (at more depth) where z_2 refers to level with less depth and z_1 refers to level with more depth. i.e.. $z_1 < z_2$. [see figure 2]

According to definition (1-Tc). eastward and northward components of thermal current can be shown as following:

$$u_{\mathrm{T_c}} = u_{g(z_2)} - u_{g(z_1)} \qquad (2\text{-Tc-a})$$

and

$$v_{\mathrm{T_c}} = v_{g(z_2)} - v_{g(z_1)} \qquad (2\text{-Tc-b})$$

where in equation (2-Tc-a). $u_{\mathrm{T_c}}$ is eastward component of thermal current. $u_{g(z_2)}$ is eastward component of geostrophic current at upper level of the oceanic layer. $u_{g(z_1)}$ is eastward component of geostrophic current at lower level of the oceanic layer; and in equation (2-Tc-b) $v_{\mathrm{T_c}}$ is northward component of thermal current. $v_{g(z_2)}$ is northward component of geostrophic current at upper level of the oceanic layer. $v_{g(z_1)}$ stands for northward component of geostrophic current at lower level of the oceanic layer and $z_1 < z_2$.

2.1.1 The first version of thermal current

For deriving formulae for the eastward component of the first version of thermal current. we should omit terms including $\frac{\partial s}{\partial y}$ and $\frac{\partial p}{\partial y}$ in equations (30-a). (32-a) and (33-a) for first step by accepting conditions (53-1) and (53-2). Now. we have following equations for deriving some part of eastward component of the first version of thermal current:

$$\frac{\partial}{\partial y}A = 6.793952 \times 10^{-2}\frac{\partial T}{\partial y} - 1.819058 \times 10^{-2}T\frac{\partial T}{\partial y} + 3.005055 \times 10^{-4}T^2\frac{\partial T}{\partial y} - 4.480332 \times 10^{-4}T^3\frac{\partial T}{\partial y} + 3.268166 \times 10^{-8}T^4\frac{\partial T}{\partial y} \qquad (28\text{-T-a})$$

And:

$$\frac{\partial}{\partial y}(Bs) = \left(-4.0899 \times 10^{-3}\frac{\partial T}{\partial y} + 1.52876 \times 10^{-4}T\frac{\partial T}{\partial y} - 2.47401 \times 10^{-6}T^2\frac{\partial T}{\partial y} + 2.155 \times 10^{-8}T^3\frac{\partial T}{\partial y}\right)s \qquad (30\text{-T-a})$$

Also:

$$\frac{\partial}{\partial y}\left(Cs^{3/2}\right) = \left(1.0227 \times 10^{-4}\frac{\partial T}{\partial y} - 3.3092 \times 10^{-6}T\frac{\partial T}{\partial y}\right)\left(s^{3/2}\right) \qquad (32\text{-T-a})$$

Therefore. derivative of seawater density at surface of ocean with respect to y. considering conditions (53-1) and (53-2); is organized by addition of equations (28-T-a). (30-T-a) and (32-T-a). i.e.:

$$\frac{\partial}{\partial y}\rho(s.T.0) = (28\text{-T-a}) + (30\text{-T-a}) + (32\text{-T-a}) = \rho_{0_{\mathrm{T_a}}} \qquad (34\text{-T-a})$$

In equation (34-T-a). the $\rho_{0_{\mathrm{T_a}}}$ is derivative of surface density of seawater with respect to y after imposing conditions (53-1) and (53-2) and subscript "T" in equations' number refers to "Thermal".

Likewise. omitting terms including $\frac{\partial s}{\partial y}$ and $\frac{\partial p}{\partial y}$ in equations (38-a). (40-a). (42-a). (44-a). (45-a). (47-a) and (49-a) by accepting conditions (53-1) and (53-2) is necessary. And we have remained following equations for deriving eastward component of the first version of thermal current:

$$\frac{\partial}{\partial y}(E) = \frac{\partial}{\partial y}(1.965221 \times 10^4 + 1.484206 \times 10^2T - 2.327105T^2 + 1.360477 \times 10^{-2}T^3 - 5.155288 \times 10^{-5}T^4) = 1.484206 \times 10^2\frac{\partial T}{\partial y} - 4.65421T\frac{\partial T}{\partial y} + 4.081431 \times 10^{-2}T^2\frac{\partial T}{\partial y} - 2.0621152 \times 10^{-4}T^3\frac{\partial T}{\partial y} \qquad (36\text{-T-a})$$

And:

$$\frac{\partial}{\partial y}(Fs) = \left(-6.03459 \times 10^{-1}\frac{\partial T}{\partial y} + 2.19974 \times 10^{-2}T\frac{\partial T}{\partial y} - 1.8501 \times 10^{-4}T^2\frac{\partial T}{\partial y}\right)s \quad (38\text{-T-a})$$

In addition:

$$\frac{\partial}{\partial y}\left(Gs^{3/2}\right) = \left(1.6483 \times 10^{-2}\frac{\partial T}{\partial y} - 1.06018 \times 10^{-3}T\frac{\partial T}{\partial y}\right)s^{3/2} \quad (40\text{-T-a})$$

Also:

$$\frac{\partial}{\partial y}(Hp) = \left(1.43713 \times 10^{-3}\frac{\partial T}{\partial y} + 2.32184 \times 10^{-4}T\frac{\partial T}{\partial y} - 1.733715 \times 10^{-6}T^2\frac{\partial T}{\partial y}\right)p \quad (42\text{-T-a})$$

And:

$$\frac{\partial}{\partial y}(Isp) = \left(-1.0981 \times 10^{-5}\frac{\partial T}{\partial y} - 3.2156 \times 10^{-6}T\frac{\partial T}{\partial y}\right)sp \quad (44\text{-T-a})$$

In addition:

$$\frac{\partial}{\partial y}(Mp^2) = \left(-6.12293 \times 10^{-6}\frac{\partial T}{\partial y} + 1.05574 \times 10^{-7}T\frac{\partial T}{\partial y}\right)p^2 \quad (47\text{-T-a})$$

Also:

$$\frac{\partial}{\partial y}(Nsp^2) = \left(2.0816 \times 10^{-8}\frac{\partial T}{\partial y} + 1.83394 \times 10^{-9}T\frac{\partial T}{\partial y}\right)sp^2 \quad (49\text{-T-a})$$

Equations (28-T-a). (30-T-a). (32-T-a). (36-T-a). (38-T-a). (40-T-a). (42-T-a). (44-T-a). (47-T-a) and (49-T-a); are equations those prepared by imposing conditions (53-1) and (53-2) for eastward component of the first version of thermal current.

Now. according to equations. (36-T-a). (38-T-a). (40-T-a). (42-T-a). (44-T-a). (47-T-a) and (49-T-a) plus imposing conditions (53-1) and (53-2); equation (50-a) will be:

$$\frac{\partial}{\partial y}[K_T(s.T.p)] = \text{(36-T-a) + (38-T-a) + (40-T-a) + (42-T-a) + (44-T-a) + (47-T-a) + (49-T-a).} \quad (50\text{-T-a})$$

Imposing conditions (53-1) and (53-2) into (24-a). we get:

$$\frac{\partial}{\partial y}\left[1 - {}^{p}/_{K_T(s.T.p)}\right] = \frac{p\frac{\partial}{\partial y}K_T(s.T.p)}{[K_T(s.T.p)]^2} \quad (24\text{-T-a})$$

Substituting (50-T-a) into (24-T-a) has following result:

$$\frac{\partial}{\partial y}\left[1 - {}^{p}/_{K_T(s.T.p)}\right] = \frac{p\,(50\text{-T-a})}{[K_T(s.T.p)]^2} \quad (51\text{-T-a})$$

And substituting (34-T-a) and (51-T-a) in equation (23-a); modify it from eastward component of the first version of dense current. to eastward component of the first version of thermal current. i.e.:

$$u_{T_{c_I}} = \frac{g}{f}\int_{z_1}^{z_2}\frac{\frac{1}{\rho(s.T.0)}}{1-{}^{p}/_{K_T(s.T.p)}} \times \frac{(34\text{-T-a})\left[1-{}^{p}/_{K_T(s.T.p)}\right]-\rho(s.T.0)(51\text{-T-a})}{\left[1-{}^{p}/_{K_T(s.T.p)}\right]^2}dz \quad (5\text{-Tc-I-a})$$

In equation (5-Tc-I-a). $u_{T_{c_I}}$ is eastward component of the first version of thermal current. g is acceleration due to gravity. f is Coriolis parameter. z_1 is depth of lower level of the oceanic layer. z_2 is upper level of the oceanic layer. $\rho(s.T.0)$ is density of surface ocean defined in (8). p is pressure of water at any point considered. $K_T(s.T.p)$ is mean bulk modulus defined in (9). (34-T-a) is equation with the same number and (51-T-a) is also equation with the same number.

And for deriving formulae for the northward component of the first version of thermal current. we should omit terms including $\frac{\partial s}{\partial x}$ and $\frac{\partial p}{\partial x}$ in equations (30-b). (32-b) and (33-b) for first step by accepting conditions (53-1) and (53-2). Now. we have following equations for deriving some part of northward component of the first version of thermal current:

$$\frac{\partial}{\partial x}A = 6.793952 \times 10^{-2}\frac{\partial T}{\partial x} - 1.819058 \times 10^{-2}T\frac{\partial T}{\partial x} + 3.005055 \times 10^{-4}T^2\frac{\partial T}{\partial x} - 4.480332 \times 10^{-4}T^3\frac{\partial T}{\partial x} + 3.268166 \times 10^{-8}T^4\frac{\partial T}{\partial x} \quad (28\text{-T-b})$$

And:

$$\frac{\partial}{\partial x}(Bs) = \left(-4.0899 \times 10^{-3}\frac{\partial T}{\partial x} + 1.52876 \times 10^{-4}T\frac{\partial T}{\partial x} - 2.47401 \times 10^{-6}T^2\frac{\partial T}{\partial x} + 2.155 \times 10^{-8}T^3\frac{\partial T}{\partial x}\right)s \quad (30\text{-T-b})$$

Also:

$$\frac{\partial}{\partial x}\left(Cs^{3/2}\right) = \left(1.0227 \times 10^{-4}\frac{\partial T}{\partial x} - 3.3092 \times 10^{-6}T\frac{\partial T}{\partial x}\right)\left(s^{3/2}\right) \quad (32\text{-T-b})$$

Therefore. derivative of seawater density at surface of ocean with respect to x. considering conditions (53-1) and (53-2); is organized by addition of equations (28-T-b). (30-T-b) and (32-T-b). i.e.:

$$\frac{\partial}{\partial x}\rho(s.T.0) = \text{(28-T-b) + (30-T-b) + (32-T-b)} = \rho_{0_{T_b}}. \quad (34\text{-T-b})$$

In equation (34-T-b). the $\rho_{0_{T_b}}$ is derivative of surface density of seawater with respect to x after imposing

conditions (53-1) and (53-2) and subscript "T" in equations' number refers to "Thermal".

Likewise. omitting terms including $\frac{\partial s}{\partial x}$ and $\frac{\partial p}{\partial x}$ in equations (38-b). (40-b). (42-b). (44-b). (45-b). (47-b) and (49-b) by accepting conditions (53-1) and (53-2) is necessary. And we have remained following equations for deriving northward component of the first version of thermal current:

$$\frac{\partial}{\partial x}(E) = \frac{\partial}{\partial x}(1.965221 \times 10^4 + 1.484206 \times 10^2 T - 2.327105T^2 + 1.360477 \times 10^{-2}T^3 - 5.155288 \times 10^{-5}T^4) = 1.484206 \times 10^2 \frac{\partial T}{\partial x} - 4.65421T\frac{\partial T}{\partial x} + 4.081431 \times 10^{-2}T^2\frac{\partial T}{\partial x} - 2.0621152 \times 10^{-4}T^3\frac{\partial T}{\partial x} \quad \text{(36-T-b)}$$

And:

$$\frac{\partial}{\partial x}(Fs) = \left(-6.03459 \times 10^{-1}\frac{\partial T}{\partial x} + 2.19974 \times 10^{-2}T\frac{\partial T}{\partial x} - 1.8501 \times 10^{-4}T^2\frac{\partial T}{\partial x}\right)s \quad \text{(38-T-b)}$$

In addition:

$$\frac{\partial}{\partial x}\left(Gs^{3/2}\right) = \left(1.6483 \times 10^{-2}\frac{\partial T}{\partial x} - 1.06018 \times 10^{-3}T\frac{\partial T}{\partial x}\right)s^{3/2} \quad \text{(40-T-b)}$$

Also:

$$\frac{\partial}{\partial x}(Hp) = \left(1.43713 \times 10^{-3}\frac{\partial T}{\partial x} + 2.32184 \times 10^{-4}T\frac{\partial T}{\partial x} - 1.733715 \times 10^{-6}T^2\frac{\partial T}{\partial x}\right)p \quad \text{(42-T-b)}$$

And:

$$\frac{\partial}{\partial x}(Isp) = \left(-1.0981 \times 10^{-5}\frac{\partial T}{\partial x} - 3.2156 \times 10^{-6}T\frac{\partial T}{\partial x}\right)sp \quad \text{(44-T-b)}$$

In addition:

$$\frac{\partial}{\partial x}(Mp^2) = \left(-6.12293 \times 10^{-6}\frac{\partial T}{\partial x} + 1.05574 \times 10^{-7}T\frac{\partial T}{\partial x}\right)p^2 \quad \text{(47-T-b)}$$

Also:

$$\frac{\partial}{\partial x}(Nsp^2) = \left(2.0816 \times 10^{-8}\frac{\partial T}{\partial x} + 1.83394 \times 10^{-9}T\frac{\partial T}{\partial x}\right)sp^2 \quad \text{(49-T-b)}$$

Equations (28-T-b). (30-T-b). (32-T-b). (36-T-b). (38-T-b). (40-T-b). (42-T-b). (44-T-b). (47-T-b) and (49-T-b); are equations those prepared by imposing conditions (53-1) and (53-2) for northward component of the first version of thermal current.

Now. according to equations. (36-T-b). (38-T-b). (40-T-b). (42-T-b). (44-T-b). (47-T-b) and (49-T-b) plus imposing conditions (53-1) and (53-2); equation (50-b) will be:

$$\frac{\partial}{\partial x}[K_T(s.T.p)] = \text{(36-T-b) + (38-T-b) + (40-T-b) + (42-T-b) + (44-T-b) + (47-T-b) + (49-T-b).} \quad \text{(50-T-b)}$$

By imposing conditions (53-1) and (53-2) into (24-b). we get:

$$\frac{\partial}{\partial x}\left[1 - {}^{p}/_{K_T(s.T.p)}\right] = \frac{p\frac{\partial}{\partial x}K_T(s.T.p)}{[K_T(s.T.p)]^2} \quad \text{(24-T-b)}$$

Substituting (50-T-b) into (24-T-b) has following result:

$$\frac{\partial}{\partial x}\left[1 - {}^{p}/_{K_T(s.T.p)}\right] = \frac{p\ (50-\text{T}-\text{b})}{[K_T(s.T.p)]^2} \quad \text{(51-T-b)}$$

And substituting (34-T-b) and (51-T-b) in equation (23-b); modify it from northward component of the first version of dense current. to northward component of the first version of thermal current. i.e.:

$$v_{\text{T}_{\text{c}_\text{I}}} = -\frac{g}{f}\int_{z_1}^{z_2} \frac{1}{\frac{\rho(s.T.0)}{1-{}^{p}/_{K_T(s.T.p)}}} \times \frac{(34-\text{T}-\text{b})\left[1-{}^{p}/_{K_T(s.T.p)}\right]-\rho(s.T.0)(51-\text{T}-\text{b})}{\left[1-{}^{p}/_{K_T(s.T.p)}\right]^2}dz \quad \text{(5-Tc-I-b)}$$

In equation (5-Tc-I-b). $v_{\text{T}_{\text{c}_\text{I}}}$ is northward component of the first version of thermal current. g is acceleration due to gravity. f is Coriolis parameter. z_1 is depth of lower level of the oceanic layer. z_2 is upper level of the oceanic layer. $\rho(s.T.0)$ is density of surface ocean defined in (8). p is pressure of seawater at any point considered. $K_T(s.T.p)$ is mean bulk modulus defined in (9). (34-T-b) is equation with the same number and (51-T-b) is also equation with the same number.

Also. considering conditions (53-1) and (53-2). then combining equations (22-a) and (22-b) yields:

$$\mathbb{v}_{\text{T}_{\text{c}_\text{I}}} = -\frac{g}{f}\int_{z_1}^{z_2} \frac{1}{\frac{\rho(s.T.0)}{1-{}^{p}/_{K_T(s.T.p)}}} \mathbb{k} \times \nabla\left[\frac{\rho(s.T.0)}{1-{}^{p}/_{K_T(s.T.p)}}\right]dz \quad \text{(4-Tc-I)}$$

Equation (4-Tc-I) is *The first version of thermal current vector* where in it. $\mathbb{v}_{\text{T}_{\text{c}_\text{I}}}$ is the first version of thermal current vector. g is acceleration due to gravity. f is Coriolis parameter. z_1 is depth of lower level of the oceanic layer. z_2 is upper level of the oceanic layer. $\rho(s.T.0)$ is density of surface ocean defined in (8). p is pressure of seawater at any point considered. $K_T(s.T.p)$ is mean bulk modulus defined in (9). $\mathbb{k}$ is vertical unit vector in Cartesian coordinates system. ∇ is gradient operator in Cartesian coordinates system and z is vertical axis in Cartesian coordinates system.

Eastward component of the first version of thermal current vector is introduced in equation (5-Tc-I-a) and northward component of it. is presented in equation

(5-Tc-I-b). Furthermore. in equation (5-Tc-I-b). derivative of seawater density with respect to x and in equation (5-Tc-I-a) derivative of seawater density with respect to y have done considering conditions (53-1) and (53-2)[4]

From the first version of thermal current vector or its components. one can perceive:

2 – 1 – 1 – A: Whatever we go from pole to equator. the first version of thermal current becomes stronger (with pay attention to footnote No. 2)

2 – 1 – 1 – B: If the oceanic layer has more thickness; then the first version of the thermal current becomes more powerful;

2 – 1 – 1 – C: Whatever oceanic layer is near to ocean surface. density would be lower and the first version of the thermal current becomes stronger as a result;

2 – 1 – 1 – D: if the temperature of the oceanic layer would be high – due to decreasing seawater density – the first version of thermal current is more powerful and

2 – 1 – 1 – E: If the horizontal gradient of seawater temperature would be greater. the first version of thermal current becomes more powerful. because the first version of the thermal current is proportional to the horizontal gradient of implicit seawater temperature.

In this manner. the first version of thermal current vector. i.e.. equation (4-Tc-I) shows that: "*The first version of thermal current flows parallel to Isopycnals and Isopleths of implicit seawater temperature so that. low values of density (high values of temperature) are located at the right side of downstream.*" (In the northern hemisphere) This fact is demonstrated in figures 3 and 4.

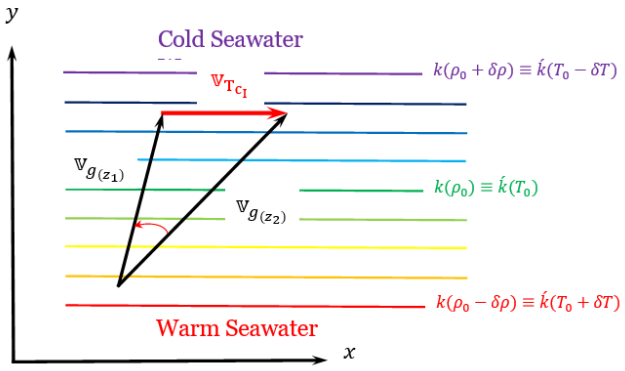

Figure 3. Counterclockwise rotation of geostrophic current with respect to depth (Backing) and warm seawater advection.

Coefficient $k=-\frac{g}{f}\langle\frac{1}{\frac{\rho(s.T.0)}{1-{}^{p}/_{K_T(s.T.p)}}}\rangle(z_2-z_1)$ and $\acute{k}$ is proportional to k in such a manner that – for instance – $k(\rho_0-\delta\rho)$ is identical to $\acute{k}(T_0+\delta T)$. [The first version of thermal current]

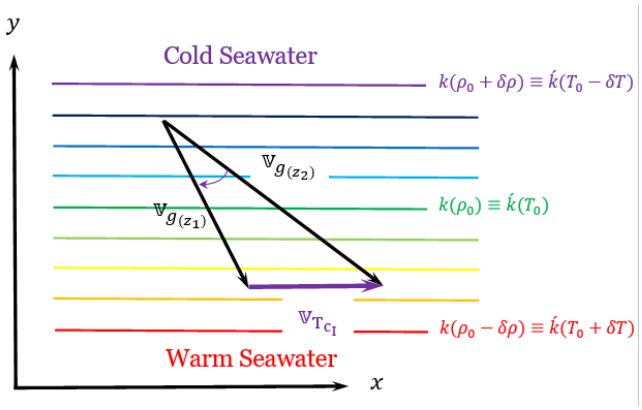

Figure 4. Clockwise rotation of geostrophic current with respect to depth (Veering) and cold seawater advection. Coefficient $k=-\frac{g}{f}\langle\frac{1}{\frac{\rho(s.T.0)}{1-{}^{p}/_{K_T(s.T.p)}}}\rangle(z_2-z_1)$ and $\acute{k}$ is proportional to k in such a manner that – for instance – $k(\rho_0+\delta\rho)$ is identical to $\acute{k}(T_0-\delta T)$. [The first version of thermal current]

In connection with figure 3. counterclockwise turning of geostrophic current with respect to depth (backing) is associated with warmer seawater advection by geostrophic current in the layer.

Conversely; as shown in figure 4. clockwise turning of geostrophic current with respect to depth (veering) implies advection of colder seawater by geostrophic current in the oceanic layer. Also $\langle\frac{1}{\frac{\rho(s.T.0)}{1-{}^{p}/_{K_T(s.T.p)}}}\rangle$ under explanations of figures 3 and 4 is vertical average of specific volume of seawater in the oceanic layer[5].

2.1.2 The second version of thermal current

Regarding to conditions (53-1) and (53-2). we had:

$$u_{T_{c_I}}=\frac{g}{f}\int_{z_1}^{z_2}\frac{1}{\frac{\rho(s.T.0)}{1-{}^{p}/_{K_T(s.T.p)}}}\times\frac{(34-\mathrm{T}-\mathrm{a})\left[1-{}^{p}/_{K_T(s.T.p)}\right]-\rho(s.T.0)(51-\mathrm{T}-\mathrm{a})}{\left[1-{}^{p}/_{K_T(s.T.p)}\right]^2}dz \quad \text{(5-Tc-I-a)}$$

Equation (5-Tc-I-a) was eastward component of the first version of thermal current.

[4] Note that limit ${}^{p}/_{K_T(s.T.p)}$ when it goes to zero from right hand is near but greater than zero. Therefore. for every p and every $K_T(s.T.p)$. we have:

$$0<1-{}^{p}/_{K_T(s.T.p)}\leq 1$$

[5] There are many procedures about averaging in meteorology and subbranches. Every method for averaging particular parameter or term. is related to position. time and specifications of the domain. All meteorological or oceanographical parameters; decreases logarithmic or semi-logarithmic and increases exponentially or semi-exponentially with respect to height or depth. Therefore. for every case. we need to use special manner for averaging. As a simple example. if we consider a layer of seawater between 200- and 300-meters depth; the easiest way is using linear averaging. i.e.. adding the value of parameters or terms of above and below levels of the oceanic layer and dividing the result by 2.

In almost all meteorological purposes. we regard acceleration due to gravity as constant. Consequently. we can enter it inside integral sign. considering conditions (53-1) and (53-2); to get eastward component of the second version of thermal current i.e.:

$$u_{T_{c_{II}}} = \frac{1}{f}\int_{z_1}^{z_2} \frac{1}{\frac{\rho(s.T.0)}{1-{}^{p}/_{K_T(s.T.p)}}} \times \frac{(34-\mathrm{T}-\mathrm{a})\left[1-{}^{p}/_{K_T(s.T.p)}\right]-\rho(s.T.0)(51-\mathrm{T}-\mathrm{a})}{\left[1-{}^{p}/_{K_T(s.T.p)}\right]^2} d\Phi_{\mathrm{T}} \quad \text{(5-Tc-II-a)}$$

where in equation (5-Tc-II-a). $u_{T_{c_{II}}}$ is eastward component of the second version of thermal current. f is Coriolis parameter. $z_1$is lower level of the oceanic layer. z_2 is higher level of the oceanic layer. $\rho(s.T.0)$ is density of surface ocean defined in (8). p is pressure of seawater at any point considered. $K_T(s.T.p)$ is mean bulk modulus defined in (9). (34-T-a) is equation with the same number and (51-T-a) is also equation with the same number. Φ is geopotential and subscript "T" refers to this fact that variation of seawater geopotential is affiliated to seawater temperature solely. with due attention to: [3]

$$\Phi = \Phi(s.T.p) \quad (35)$$

And for deriving formula for the northward component of the second version of thermal current. by considering conditions (53-1) and (53-2); we fix the mind on equation (5-Tc-I-b) that was northward component of the first version of thermal current i.e.:

$$v_{T_{c_I}} = -\frac{g}{f}\int_{z_1}^{z_2} \frac{1}{\frac{\rho(s.T.0)}{1-{}^{p}/_{K_T(s.T.p)}}} \times \frac{(34-\mathrm{T}-\mathrm{b})\left[1-{}^{p}/_{K_T(s.T.p)}\right]-\rho(s.T.0)(51-\mathrm{T}-\mathrm{b})}{\left[1-{}^{p}/_{K_T(s.T.p)}\right]^2} dz \quad \text{(5-Tc-I-b)}$$

Equation (5-Tc-I-b) was northward component of the first version of thermal current. and we can enter acceleration due to gravity inside integral sign to get northward component of the second version of thermal current. i.e.:

$$v_{T_{c_{II}}} = -\frac{1}{f}\int_{z_1}^{z_2} \frac{1}{\frac{\rho(s.T.0)}{1-{}^{p}/_{K_T(s.T.p)}}} \times \frac{(34-\mathrm{T}-\mathrm{b})\left[1-{}^{p}/_{K_T(s.T.p)}\right]-\rho(s.T.0)(51-\mathrm{T}-\mathrm{b})}{\left[1-{}^{p}/_{K_T(s.T.p)}\right]^2} d\Phi_{\mathrm{T}} \quad \text{(5-Tc-II-b)}$$

where in equation (5-Tc-II-b). $v_{T_{c_{II}}}$ is northward component of the second version of thermal current. f is Coriolis parameter. $z_1$is lower level of the oceanic layer. z_2 is higher level of the oceanic layer. $\rho(s.T.0)$ is density of surface ocean defined in (8). p is pressure of seawater at any point considered. $K_T(s.T.p)$ is mean bulk modulus defined in (9). (34-T-b) is equation with the same number and (51-T-b) is also equation with the same number. Φ is geopotential and subscript "T" refers to this fact that variation of seawater geopotential is affiliated to seawater temperature solely. with due attention to (35)

The first version of thermal current vector was:

$$\mathbb{v}_{T_{c_I}} = -\frac{g}{f}\int_{z_1}^{z_2} \frac{1}{\frac{\rho(s.T.0)}{1-{}^{p}/_{K_T(s.T.p)}}} \mathbb{k} \times \nabla\left[\frac{\rho(s.T.0)}{1-{}^{p}/_{K_T(s.T.p)}}\right] dz \quad \text{(4-Tc-I)}$$

If we enter acceleration due to gravity inside integral sign. we get the second version of thermal current: i.e.:

$$\mathbb{v}_{T_{c_{II}}} = -\frac{1}{f}\int_{z_1}^{z_2} \frac{1}{\frac{\rho(s.T.0)}{1-{}^{p}/_{K_T(s.T.p)}}} \mathbb{k} \times \nabla\left[\frac{\rho(s.T.0)}{1-{}^{p}/_{K_T(s.T.p)}}\right] d\Phi_{\mathrm{T}} \quad \text{(4-Tc-II)}$$

Equation (4-Tc-II) is <u>*The second version of thermal current vector*</u> where in it. $\mathbb{v}_{T_{c_{II}}}$ is the second version of thermal current vector. f is Coriolis parameter. z_1 is depth of lower level of the oceanic layer. z_2 is upper level of the oceanic layer. $\rho(s.T.0)$ is density of surface ocean defined in (8). p is pressure of seawater at any point considered. $K_T(s.T.p)$ is mean bulk modulus defined in (9). $\mathbb{k}$ is vertical unit vector in Cartesian coordinates system. ∇ is gradient operator in Cartesian coordinates system. Φ is geopotential and subscript " T " refers to this fact that variation of seawater geopotential is affiliated to seawater temperature solely.

Eastward component of the second version of thermal current vector is introduced in equation (5-Tc-II-a) and northward component of it. is presented in equation (5-Tc-II-b).

From the second version of thermal current vector or its components. one can perceive:

2 – 1 – 2 – A: Whatever we go from pole to equator. the second version of thermal current becomes stronger (with pay attention to footnote No. 2)

2 – 1 – 2 – B: If the oceanic layer has more geopotential thickness; then the second version of the thermal current becomes more powerful;

2 – 1 – 2 – C: Whatever oceanic layer is near to ocean surface; density would be lower and the second version of the thermal current becomes stronger as a result;

2 – 1 – 2 – D: if the temperature of the oceanic layer would be high. the second version of thermal current is more powerful and

2 – 1 – 2 – E: If the horizontal gradient of seawater temperature would be greater. the second version of thermal current becomes more powerful. because the second version of the thermal current is proportional to the horizontal gradient of implicit seawater temperature.

In this manner. the second version of thermal current vector. i.e.. equation (4-Tc-II) shows that: "*The second version of thermal current flows parallel to Isopycnals and Isopleths of implicit seawater temperature as well as isopleths of geopotentials so that. low values of density (high values of temperature or high values of geopotentials) are located at the right side of downstream.*" (In the northern hemisphere) This fact is illustrated in figures 5 and 6.

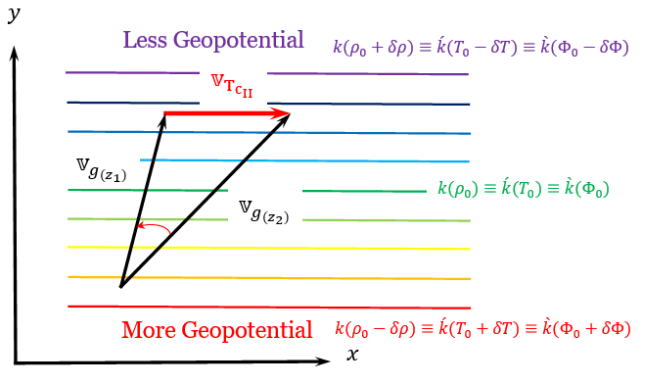

Figure 5. Counterclockwise rotation of geostrophic current with respect to depth (Backing) and more geopotential advection. Coefficient $k=-\frac{1}{f}\langle\frac{1}{\frac{\rho(s.T.0)}{1-{}^{p}/_{K_T(s.T.p)}}}\rangle(\Phi_2-\Phi_1)$. $\acute{k}$ is proportional to k in such a manner that – for instance – $k(\rho_0-\delta\rho)$ is identical to $\acute{k}(T_0+\delta T)$ and $\grave{k}$ is proportional to k in style that – for example – $k(\rho_0-\delta\rho)$ is similar in very detail to $\grave{k}(\Phi_0+\delta\Phi)$ [The second version of thermal current]

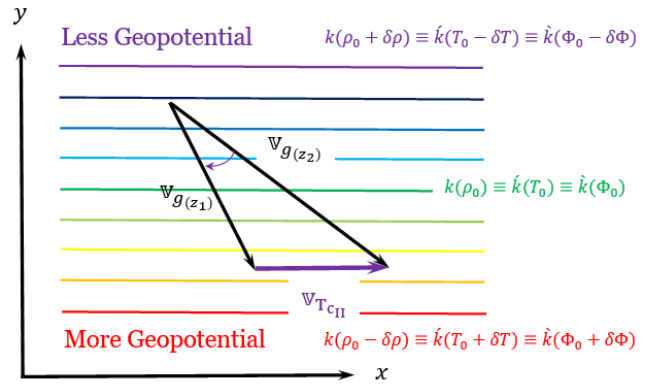

Figure 6. Clockwise rotation of geostrophic current with respect to depth (Veering) and less geopotential advection. Coefficient $k=-\frac{1}{f}\langle\frac{1}{\frac{\rho(s.T.0)}{1-{}^{p}/_{K_T(s.T.p)}}}\rangle(\Phi_2-\Phi_1)$. $\acute{k}$ is proportional to k in such a manner that – for instance – $k(\rho_0+\delta\rho)$ is identical to $\acute{k}(T_0-\delta T)$ and $\grave{k}$ is proportional to k in style that – for example – $k(\rho_0+\delta\rho)$ is similar in very detail to $\grave{k}(\Phi_0-\delta\Phi)$ [The second version of thermal current]

In connection with figure 5 – considering conditions (53-1) and (53-2) – counterclockwise turning of geostrophic current with respect to depth (backing) is associated with more geopotential advection in the ocean by geostrophic current in the layer.
Conversely; as shown in figure 6 – considering conditions (53-1) and (53-2) – clockwise turning of geostrophic current with respect to depth (veering) implies less geopotential advection in the ocean by geostrophic current in the oceanic layer.

2.1.3 The third version of thermal current

For deriving formulae for the third version of thermal current by considering conditions (53-1). (53-2) and this fact that. variation of geopotential is related to variation of seawater temperature only; first we fix the mind on equation (5-Dc-III-a) that was eastward components of the third version of dense current i.e.:

$$u_{D_{c_{III}}}=-\frac{1}{f}\frac{\partial}{\partial y}(\Phi_2-\Phi_1) \qquad \text{(5-Dc-III-a)}$$

In equation (5-Dc-III-a). $u_{D_{c_{III}}}$ is eastward component of the third version of dense current and we used definition (2-Dc-a) for deriving this equation.
And northward component of the third version of dense current was:

$$v_{D_{c_{III}}}=\frac{1}{f}\frac{\partial}{\partial x}(\Phi_2-\Phi_1) \qquad \text{(5-Dc-III-b)}$$

In equation (5-Dc-III-b). $v_{D_{c_{III}}}$ is northward component of the third version of dense current and we used definition (2-Dc-b) for extracting this equation.
With due attention to: [3]

$$\Phi=\Phi(s.T.p) \qquad (35)$$

and emphasis on conditions (53-1) and (53-2) based upon that horizontal variation of seawater density is related to horizontal variation of seawater temperature solely. and implies variation of seawater geopotential height only by horizontal variation of seawater temperature. we get:

$$u_{T_{c_{III}}}=-\frac{1}{f}\frac{\partial}{\partial y}\left(\Phi_{T_2}-\Phi_{T_1}\right) \qquad \text{(5-Tc-III-a)}$$

where. in equation (5-Tc-III-a). $u_{T_{c_{III}}}$ is eastward component of the third version of thermal current. f is Coriolis parameter. y is northward axis of Cartesian coordinates system. Φ_{T_2} is geopotential of higher level of the oceanic layer. Φ_{T_1} is geopotential of lower level of the oceanic layer and $\left(\Phi_{T_2}-\Phi_{T_1}\right)$ is geopotential thickness of the oceanic layer. Furthermore. subscript "T" refers to this fact that increasing or decreasing of geopotential thickness is related on seawater temperature only. with due attention to (35).
Also:

$$v_{T_{c_{III}}}=\frac{1}{f}\frac{\partial}{\partial x}\left(\Phi_{T_2}-\Phi_{T_1}\right) \qquad \text{(5-Tc-III-b)}$$

where. in equation (5-Tc-III-b). $v_{T_{c_{III}}}$ is northward component of the third version of thermal current. f is Coriolis parameter. x is eastward axis of Cartesian coordinates system. Φ_{T_2} is geopotential of higher level

of the oceanic layer. Φ_{T_1} is geopotential of lower level of the oceanic layer and $(\Phi_{T_2} - \Phi_{T_1})$ is geopotential thickness of the oceanic layer. Furthermore. subscript "T" refers to this fact that increasing or decreasing of geopotential thickness is related on seawater temperature only. with due attention to (35).
In addition. by joining (5-Tc-III-a) and (5-Tc-III-b) as vector. we obtain:

$$\mathbb{v}_{T_{c_{III}}} = f^{-1}\mathbb{k} \times \nabla_p(\Phi_{T_2} - \Phi_{T_1}) \qquad (4\text{-Tc-III})$$

where. in equation (4-Tc-III). $\mathbb{v}_{T_{c_{III}}}$ is: *The third version of thermal current vector*. f is Coriolis parameter. $\mathbb{k}$ is vertical unit vector in pressure coordinates system. ∇_p is gradient operator in pressure coordinates system. Φ_{T_2} is geopotential of higher level of the oceanic layer. Φ_{T_1} is geopotential of lower level of the oceanic layer and $(\Phi_{T_2} - \Phi_{T_1})$ is geopotential thickness of the oceanic layer. Furthermore. subscript "T" refers to this fact that increasing or decreasing of geopotential is related on seawater temperature only. with due attention to (35).
From the third version of thermal current vector or its components. one can perceive:
2 – 1 – 3 – A: Whatever we go from pole to equator. the third version of thermal current becomes stronger (with pay attention to footnote No. 2)
2 – 1 – 3 – B: If the oceanic layer has more geopotential thickness; then the third version of the thermal current becomes more powerful. and
2 – 1 – 3 – C: If the horizontal gradient of seawater geopotential thickness would be greater. the third version of thermal current becomes more powerful. because the third version of the thermal current is proportional to the horizontal gradient of seawater geopotential thickness.
In this manner. the third version of thermal current vector. i.e.. equation (4-Tc-III) shows that: "*The third version of thermal current flows parallel to Isopleths of geopotential thickness of the oceanic layer* i.e.. $(\Phi_{T_2} - \Phi_{T_1})$ *so that. high values of geopotential thickness are located at the right side of downstream.*" (In the northern hemisphere) This fact is demonstrated in figures 7 and 8.

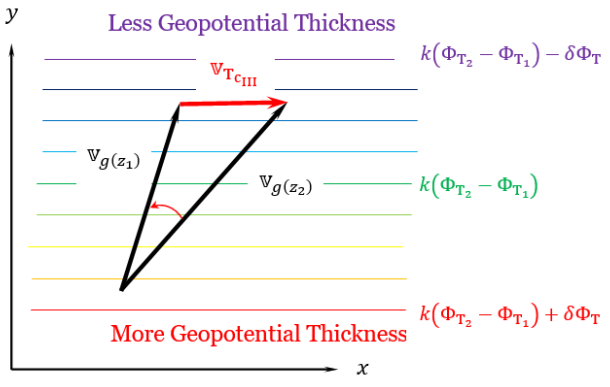

Figure 7. Counterclockwise rotation of geostrophic current with respect to depth (Backing) and more geopotential thickness advection. Coefficient $k = \frac{1}{f}$ [The third version of thermal current]

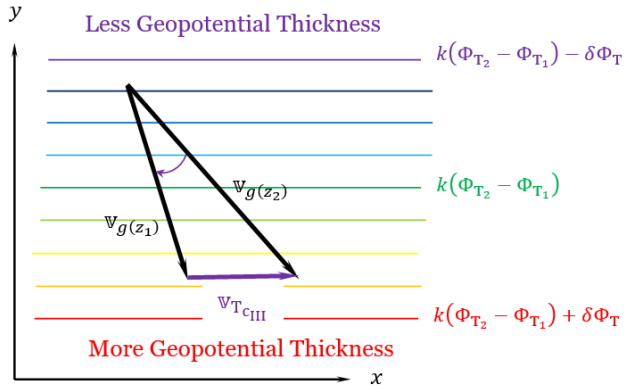

Figure 8. Clockwise rotation of geostrophic current with respect to depth (Veering) and less geopotential thickness advection. Coefficient $k = \frac{1}{f}$ [The third version of thermal current]

In connection with figure 7 – considering conditions (53-1) and (53-2) – counterclockwise turning of geostrophic current with respect to depth (backing) is associated with more geopotential thickness advection of the oceanic layer by geostrophic current in the layer. Conversely; as shown in figure 8 – considering conditions (53-1) and (53-2) – clockwise turning of geostrophic current with respect to depth (veering) implies less geopotential thickness advection of oceanic layer by geostrophic current in the oceanic layer.

2.2. Second special case of dense current: Saline Current

As we memorize; baroclinity of seawater is depending on horizontal gradient of seawater density. But if:

$$p = constant \text{ or } \left(\frac{\partial p}{\partial x} = 0 \ \wedge \ \frac{\partial p}{\partial y} = 0\right) \qquad (53\text{-}2)$$

and

$$T = constant \text{ or } \left(\frac{\partial T}{\partial x} = 0 \ \wedge \ \frac{\partial T}{\partial y} = 0\right) \qquad (53\text{-}3)$$

then. baroclinity of seawater related only to the horizontal gradient of seawater salinity.
By existing conditions (53-2) and (53-3). horizontal gradient of seawater salinity causes to produce baroclinity of ambience solely.
In these conditions; i.e.. conditions (53-2) and (53-3); the variation of density in the horizontal direction is merely related to variation of seawater salinity in horizontal direction causing baroclinity of the ocean. In these circumstances. we define the vectorial difference of geostrophic current vector at upper level and geostrophic current vector at lower level of the oceanic

layer as. *Saline Current*. (by pay attention to figure 2) i.e.:

$$\mathbb{v}_{S_c} \equiv \mathbb{v}_{g(z_2)} - \mathbb{v}_{g(z_1)} \qquad \text{(1-Sc)}$$

where in Equation (1-Sc) $\mathbb{v}_{S_c}$ stands for saline current vector. $\mathbb{v}_{g(z_2)}$ is geostrophic current at upper level of the oceanic layer (at less depth). and $\mathbb{v}_{g(z_1)}$ is geostrophic current at lower level of the oceanic layer (at more depth) where z_2 refers to level with less depth and z_1 refers to level with more depth. i.e.. $z_1 < z_2$. [see figure 2]

According to definition (1-Sc). eastward and northward components of saline current can be shown as following:

$$u_{S_c} = u_{g(z_2)} - u_{g(z_1)} \qquad \text{(2-Sc-a)}$$

and

$$v_{S_c} = v_{g(z_2)} - v_{g(z_1)} \qquad \text{(2-Sc-b)}$$

where in equation (2-Sc-a). u_{S_c} is eastward component of saline current. $u_{g(z_2)}$ is eastward component of geostrophic current at upper level of the oceanic layer. $u_{g(z_1)}$ is eastward component of geostrophic current at lower level of the oceanic layer; and in equation (2-Sc-b) v_{S_c} is northward component of saline current. $v_{g(z_2)}$ is northward component of geostrophic current at upper level of the oceanic layer. $v_{g(z_1)}$ stands for northward component of geostrophic current at lower level of the oceanic layer and $z_1 < z_2$.

2.2.1 The first version of saline current

For deriving formulae for the first version of saline current. first bear in mind equation (23-a) that was eastward component of the first version of dense current:

$$u_{D_{c_I}} = \frac{g}{f}\int_{z_1}^{z_2} \frac{1}{\frac{\rho(s.T.0)}{1-{}^{p}/_{K_T(s.T.p)}}} \times \frac{\frac{\partial\rho}{\partial y}(s.T.0)\left[1-{}^{p}/_{K_T(s.T.p)}\right] - \rho(s.T.0)\frac{\partial}{\partial y}\left[1-{}^{p}/_{K_T(s.T.p)}\right]}{\left[1-{}^{p}/_{K_T(s.T.p)}\right]^2} dz \qquad \text{(23-a)}$$

And we remind equations (26-a). (28-a). (30-a). (32-a). (33-a). (34-a). (35-a). (36-a). (38-a). (40-a). (42-a). (44-a). (45-a). (47-a). (49-a). (50-a). (51-a) and (52-a); and applying conditions (53-2) and (53-3) on them. The results are as following:

$$\frac{\partial}{\partial y}(Bs) = (8.24493 \times 10^{-1} - 4.0899 \times 10^{-3}T + 7.6438 \times 10^{-5}T^2 - 8.2467 \times 10^{-7}T^3 + 5.3875 \times 10^{-9}T^4)\frac{\partial s}{\partial y} \qquad \text{(30-s-a)}$$

And:

$$\frac{\partial}{\partial y}\left(Cs^{3}/_{2}\right) = (-5.72466 \times 10^{-3} + 1.0227 \times 10^{-4}T - 1.6546 \times 10^{-6}T^2)\left(\frac{3}{2}\, s^{1}/_{2}\frac{\partial s}{\partial y}\right) \qquad \text{(32-s-a)}$$

Also:

$$\frac{\partial}{\partial y}(Ds^2) = \frac{\partial}{\partial y}[(4.8314 \times 10^{-4})s^2] = 9.6628 \times 10^{-4} s\frac{\partial s}{\partial y} \qquad \text{(33-s-a)}$$

Therefore. derivative of seawater density at surface of ocean with respect to y. is organized by addition of equations (30-s-a). (32-s-a) and (33-s-a) and considering conditions (53-2) and (53-3). i.e.:

$$\frac{\partial}{\partial y}\rho(s.T.0) = \text{(30-s-a)} + \text{(32-s-a)} + \text{(33-s-a)} = \rho_{0_{s_a}} \qquad \text{(34-s-a)}$$

In equation (34-s-a). the $\rho_{0_{s_a}}$ is derivative of surface density of seawater with respect to y after imposing conditions (53-2) and (53-3) and subscript "s" in equations' number refers to "Saline".

Furthermore:

$$\frac{\partial}{\partial y}(Fs) = (5.46746 \times 10^{1} - 6.03459 \times 10^{-1}T + 1.09987 \times 10^{-2}T^2 - 6.1670 \times 10^{-5}T^3)\frac{\partial s}{\partial y} \qquad \text{(38-s-a)}$$

And:

$$\frac{\partial}{\partial y}\left(Gs^{3}/_{2}\right) = (7.944 \times 10^{-2} + 1.6483 \times 10^{-2}T - 5.3009 \times 10^{-4}T^2)\frac{3}{2}s^{1}/_{2}\frac{\partial s}{\partial y} \qquad \text{(40-s-a)}$$

In addition:

$$\frac{\partial}{\partial y}(Isp) = (2.2838 \times 10^{-3} - 1.0981 \times 10^{-5}T - 1.6078 \times 10^{-6}T^2)\frac{\partial s}{\partial y}p \qquad \text{(44-s-a)}$$

And with aid of equation (19):

$$\frac{\partial}{\partial y}\left(Js^{3}/_{2}p\right) = 2.866125 \times 10^{-4}s^{1}/_{2}\frac{\partial s}{\partial y}p \qquad \text{(45-s-a)}$$

Also:

$$\frac{\partial}{\partial y}(Nsp^2) = (-9.9348 \times 10^{-7} + 2.0816 \times 10^{-8}T + 9.1697 \times 10^{-10}T^2)\frac{\partial s}{\partial y}p^2 \qquad \text{(49-s-a)}$$

According to equations (35-a). (38-s-a). (40-s-a). (44-s-a). (45-s-a) and (49-s-a). we have:

$$\frac{\partial}{\partial y}[K_T(s.T.p)] = \text{(38-s-a)} + \text{(40-s-a)} + \text{(44-s-a)} + \text{(45-s-a)} + \text{(49-s-a)}. \qquad \text{(50-s-a)}$$

Contemplate conditions (53-2) and (53-3) and considering equation (50-s-a); equation (24-a) will be:

$$\frac{\partial}{\partial y}\left[1-{}^{p}/_{K_T(s.T.p)}\right]=\frac{p(50-\mathrm{s}-\mathrm{a})-\frac{\partial p}{\partial y}K_T(s.T.p)}{[K_T(s.T.p)]^2} \quad (51\text{-s-a})$$

Substituting (34-s-a) and (51-s-a) in (25-a) yields eastward component of the first version of the saline current. i.e.:

$$u_{S_{c_I}}=\frac{g}{f}\int_{z_1}^{z_2}\frac{1}{\frac{\rho(s.T.0)}{1-{}^{p}/_{K_T(s.T.p)}}}\times \frac{(34-\mathrm{s}-\mathrm{a})\left[1-{}^{p}/_{K_T(s.T.p)}\right]-\rho(s.T.0)(51-\mathrm{s}-\mathrm{a})}{\left[1-{}^{p}/_{K_T(s.T.p)}\right]^2}dz \quad (5\text{-Sc-I-a})$$

where in equation (5-Sc-I-a). $u_{S_{c_I}}$ is eastward component of the first version of saline current. g is acceleration due to gravity. f is Coriolis parameter. z_1 is lower level of the oceanic layer. z_2 is higher level of the oceanic layer. $\rho(s.T.0)$ is density of surface ocean defined in (8). p is pressure of seawater at any point considered. $K_T(s.T.p)$ is mean bulk modulus defined in (9). (34-s-a) is equation with the same number and (51-s-a) is also equation with the same number and z stands for vertical axis of Cartesian coordinates system.

And for deriving formulae for the northward component of the first version of saline current. first we fix the mind on equation (23-b) that was northward component of the first version of dense current:

$$v_{D_{c_I}}=-\frac{g}{f}\int_{z_1}^{z_2}\frac{1}{\frac{\rho(s.T.0)}{1-{}^{p}/_{K_T(s.T.p)}}}\times \frac{\frac{\partial}{\partial x}\rho(s.T.0)\left[1-{}^{p}/_{K_T(s.T.p)}\right]-\rho(s.T.0)\frac{\partial}{\partial x}\left[1-{}^{p}/_{K_T(s.T.p)}\right]}{\left[1-{}^{p}/_{K_T(s.T.p)}\right]^2}dz \quad (23\text{-b})$$

And we remind equations (26-b). (28-b). (30-b). (32-b). (33-b). (34-b). (35-b). (36-b). (38-b). (40-b). (42-b). (44-b). (45-b). (47-b). (49-b). (50-b). (51-b) and (52-b); and applying conditions (53-2) and (53-3) on them. The results are as following:

$$\frac{\partial}{\partial x}(Bs)=(8.24493\times10^{-1}-4.0899\times10^{-3}T+7.6438\times10^{-5}T^2-8.2467\times10^{-7}T^3+5.3875\times10^{-9}T^4)\frac{\partial s}{\partial x} \quad (30\text{-s-b})$$

And:

$$\frac{\partial}{\partial x}\left(Cs^{3}/_{2}\right)=(-5.72466\times10^{-3}+1.0227\times10^{-4}T-1.6546\times10^{-6}T^2)\left(\frac{3}{2}\,s^{1}/_{2}\frac{\partial s}{\partial x}\right) \quad (32\text{-s-b})$$

In addition:

$$\frac{\partial}{\partial x}(Ds^2)=\frac{\partial}{\partial x}[(4.8314\times10^{-4})s^2]=9.6628\times10^{-4}s\frac{\partial s}{\partial x} \quad (33\text{-s-b})$$

Therefore. derivative of seawater density at surface of ocean with respect to x. is organized by addition of equations (30-s-b). (32-s-b) and (33-s-b) considering conditions (53-2) and (53-3). i.e.:

$$\frac{\partial}{\partial x}\rho(s.T.0)=(30\text{-s-b})+(32\text{-s-b})+(33\text{-s-b})=\rho_{0_{s_b}} \quad (34\text{-s-b})$$

In equation (34-s-b). the $\rho_{0_{s_b}}$ is derivative of surface density of seawater with respect to x after imposing conditions (53-2) and (53-3) and subscript "s" in equations' number refers to "Saline".

Furthermore. contemplating conditions (53-2) and (53-3). we have:

$$\frac{\partial}{\partial x}(Fs)=(5.46746\times10^{1}-6.03459\times10^{-1}T+1.09987\times10^{-2}T^2-6.1670\times10^{-5}T^3)\frac{\partial s}{\partial x} \quad (38\text{-s-b})$$

And:

$$\frac{\partial}{\partial x}\left(Gs^{3}/_{2}\right)=(7.944\times10^{-2}+1.6483\times10^{-2}T-5.3009\times10^{-4}T^2)\frac{3}{2}s^{1}/_{2}\frac{\partial s}{\partial x} \quad (40\text{-s-b})$$

Also:

$$\frac{\partial}{\partial x}(Isp)=(2.2838\times10^{-3}-1.0981\times10^{-5}T-1.6078\times10^{-6}T^2)\frac{\partial s}{\partial x}p \quad (44\text{-s-b-})$$

In addition:

$$\frac{\partial}{\partial x}\left(Js^{3}/_{2}p\right)=2.866125\times10^{-4}s^{1}/_{2}\frac{\partial s}{\partial x}p \quad (45\text{-s-b})$$

And:

$$\frac{\partial}{\partial x}(Nsp^2)=(-9.9348\times10^{-7}+2.0816\times10^{-8}T+9.1697\times10^{-10}T^2)\frac{\partial s}{\partial x}p^2 \quad (49\text{-s-b})$$

According to equations (38-s-b). (40-s-b). (44-s-b). (45-s-b) and (49-s-b) by having in mind conditions (53-2) and (53-3):

$$\frac{\partial}{\partial x}[K_T(s.T.p)]=(38\text{-s-b})+(40\text{-s-b})+(44\text{-s-b})+(45\text{-s-b})+(49\text{-s-b}). \quad (50\text{-s-b})$$

Considering conditions (53-2) and (53-3) and substituting (50-s-b) into equation (24-b) yields:

$$\frac{\partial}{\partial x}\left[1-{}^{p}/_{K_T(s.T.p)}\right]=\frac{p(50-\mathrm{s}-\mathrm{b})}{[K_T(s.T.p)]^2} \quad (51\text{-s-b})$$

Substituting (34-s-b) and (51-s-b) in (23-b) yields northward component of the first version of saline current. i.e.:

$$v_{S_{c_I}} = -\frac{g}{f}\int_{z_1}^{z_2} \frac{1}{\frac{\rho(s.T.0)}{1-{}^{p}/_{K_T(s.T.p)}}} \times \frac{(34-s-b)\left[1-{}^{p}/_{K_T(s.T.p)}\right]-\rho(s.T.0)(51-s-b)}{\left[1-{}^{p}/_{K_T(s.T.p)}\right]^2} dz \quad \text{(5-Sc-I-b)}$$

where in equation (5-Sc-I-b). $v_{S_{c_I}}$ is northward component of the first version of saline current. g is acceleration due to gravity. f is Coriolis parameter. z_1 is lower level of the oceanic layer. z_2 is higher level of the oceanic layer. $\rho(s.T.0)$ is density of surface ocean defined in (8). p is pressure of seawater at any point considered. $K_T(s.T.p)$ is mean bulk modulus defined in (9). (34-s-b) is equation with the same number and (51-s-b) is also equation with the same number and z stands for vertical axis of Cartesian coordinates system.

Also. considering conditions (53-2) and (53-3). then combining equations (22-a) and (22-b) yields:

$$\mathbb{v}_{S_{c_I}} = -\frac{g}{f}\int_{z_1}^{z_2} \frac{1}{\frac{\rho(s.T.0)}{1-{}^{p}/_{K_T(s.T.p)}}} \mathbb{k} \times \nabla\left[\frac{\rho(s.T.0)}{1-{}^{p}/_{K_T(s.T.p)}}\right] dz \quad \text{(4-Sc-I)}$$

Equation (4-Sc-I) is <u>*The first version of saline current vector*</u> where in it. $\mathbb{v}_{S_{c_I}}$ is the first version of saline current vector. g is acceleration due to gravity. f is Coriolis parameter. z_1 is depth of lower level of the oceanic layer. z_2 is upper level of the oceanic layer. $\rho(s.T.0)$ is density of surface ocean defined in (8). p is pressure of seawater at any point considered. $K_T(s.T.p)$ is mean bulk modulus defined in (9). $\mathbb{k}$ is vertical unit vector in Cartesian coordinates system. ∇ is gradient operator in Cartesian coordinates system and z is vertical axis in Cartesian coordinates system.

Eastward component of the first version of saline current vector is introduced in equation (5-Sc-I-a) and northward component of it. is presented in equation (5-Sc-I-b). Furthermore. in equation (5-Sc-I-b). derivative of seawater density with respect to x and in equation (5-Sc-I-a) derivative of seawater density with respect to y have done considering conditions (53-2) and (53-3) [by attention to note No. 4]

From the first version of saline current vector or its components. one can see:

2 – 2 – 1 – A: Whatever we go from pole to equator. the first version of saline current becomes stronger (with pay attention to footnote No. 2)

2 – 2 – 1 – B: If the oceanic layer has more thickness; then the first version of the saline current becomes more powerful;

2 – 2 – 1 – C: Whatever oceanic layer is near to ocean surface; density would be lower and the first version of the saline current becomes stronger as a result;

2 – 2 – 1 – D: if the salinity of the oceanic layer would be less – due to decreasing seawater density – the first version of saline current is more powerful and

2 – 2 – 1 – E: If the horizontal gradient of seawater salinity would be greater. the first version of saline current becomes more powerful. because the first version of the saline current is proportional to the horizontal gradient of implicit seawater salinity.

In this manner. the first version of saline current vector. i.e.. equation (4-Sc-I) shows that: "*The first version of saline current flows parallels to Isopycnals and Isopleths of implicit seawater salinity so that. low values of density (low values of salinity) are located at the right side of downstream.*" (In the northern hemisphere) This fact is illustrated in figures 9 and 10.

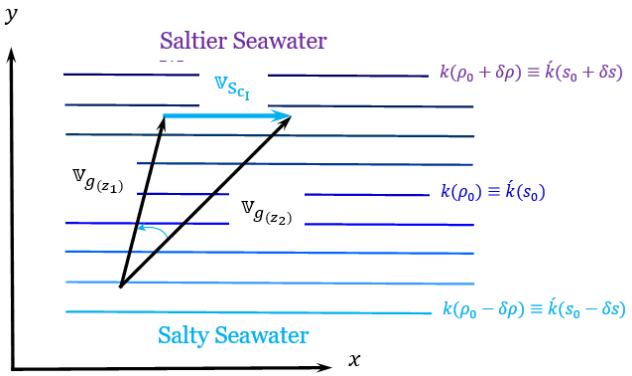

Figure 9. Counterclockwise rotation of geostrophic current with respect to depth (Backing) and less saltiness seawater advection. Coefficient $k = -\frac{g}{f}\langle\frac{1}{\frac{\rho(s.T.0)}{1-{}^{p}/_{K_T(s.T.p)}}}\rangle(z_2 - z_1)$ and $\acute{k}$ is proportional to k in such a manner that – for instance – $k(\rho_0 - \delta\rho)$ is identical to $\acute{k}(s_0 - \delta s)$. [The first version of saline current]

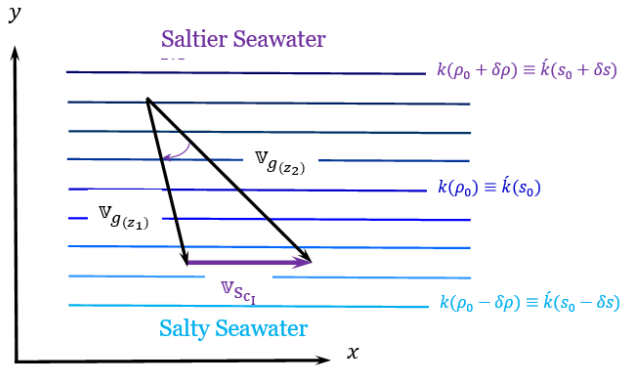

Figure 10. Clockwise rotation of geostrophic current with respect to depth (Veering) and saltier seawater advection. Coefficient $k = -\frac{g}{f}\langle\frac{1}{\frac{\rho(s.T.0)}{1-{}^{p}/_{K_T(s.T.p)}}}\rangle(z_2 - z_1)$ and $\acute{k}$ is proportional to k in such a manner that – for instance – $k(\rho_0 + \delta\rho)$ is identical to $\acute{k}(s_0 + \delta s)$. [The first version of saline current]

In connection with figure 9. counterclockwise turning of geostrophic current with respect to depth (backing) is associated with less saltier seawater advection by geostrophic current in the layer.

Conversely; as shown in figure 10. clockwise turning of geostrophic current with respect to depth (veering) implies advection of saltier seawater by geostrophic

current in the oceanic layer. Also $\langle \frac{1}{\frac{\rho(s.T.0)}{1-{}^{p}/_{K_T(s.T.p)}}} \rangle$ under explanations of figures 9 and 10 is vertical average of specific volume of seawater in the oceanic layer.

2.2.2 The second version of saline current

Regarding to conditions (53-2) and (53-3). we had:

$$u_{S_{c_I}} = \frac{g}{f}\int_{z_1}^{z_2} \frac{1}{\frac{\rho(s.T.0)}{1-{}^{p}/_{K_T(s.T.p)}}} \times \frac{(34-\text{s}-\text{a})\left[1-{}^{p}/_{K_T(s.T.p)}\right]-\rho(s.T.0)(51-\text{s}-\text{a})}{\left[1-{}^{p}/_{K_T(s.T.p)}\right]^2} dz \quad \text{(5-Sc-I-a)}$$

Equation (5-Dc-I-a) was eastward component of the first version of saline current.

In almost all meteorological purposes. we regard acceleration due to gravity as constant. Consequently. we can enter it inside integral sign. considering conditions (53-2) and (53-3); to get eastward component of the second version of saline current i.e.:

$$u_{S_{c_{II}}} = \frac{1}{f}\int_{z_1}^{z_2} \frac{1}{\frac{\rho(s.T.0)}{1-{}^{p}/_{K_T(s.T.p)}}} \times \frac{(34-\text{s}-\text{a})\left[1-{}^{p}/_{K_T(s.T.p)}\right]-\rho(s.T.0)(51-\text{s}-\text{a})}{\left[1-{}^{p}/_{K_T(s.T.p)}\right]^2} d\Phi_{\text{s}} \quad \text{(5-Sc-II-a)}$$

where in equation (5-Sc-II-a). $u_{S_{c_{II}}}$ is eastward component of the second version of saline current. f is Coriolis parameter. $z_1$is lower level of the oceanic layer. z_2 is higher level of the oceanic layer. $\rho(s.T.0)$ is density of surface ocean defined in (8). p is pressure of seawater at any point considered. $K_T(s.T.p)$ is mean bulk modulus defined in (9). (34-s-a) is equation with the same number and (51-s-a) is also equation with the same number. Φ is geopotential and subscript "s" refers to this fact that variation of seawater geopotential is affiliated to seawater salinity solely. with due attention to: [3]

$$\Phi = \Phi(s.T.p) \quad (35)$$

And for deriving formula for the northward component of the second version of saline current. by considering conditions (53-2) and (53-3); we fix the mind on equation (5-Sc-I-b) that was northward component of the first version of saline current i.e.:

$$v_{S_{c_I}} = -\frac{g}{f}\int_{z_1}^{z_2} \frac{1}{\frac{\rho(s.T.0)}{1-{}^{p}/_{K_T(s.T.p)}}} \times \frac{(34-\text{s}-\text{b})\left[1-{}^{p}/_{K_T(s.T.p)}\right]-\rho(s.T.0)(51-\text{s}-\text{b})}{\left[1-{}^{p}/_{K_T(s.T.p)}\right]^2} dz \quad \text{(5-Sc-I-b)}$$

Equation (5-Sc-I-b) was northward component of the first version of saline current. and we can enter acceleration due to gravity inside integral sign to get northward component of the second version of saline current. i.e.:

$$v_{S_{c_{II}}} = -\frac{1}{f}\int_{z_1}^{z_2} \frac{1}{\frac{\rho(s.T.0)}{1-{}^{p}/_{K_T(s.T.p)}}} \times \frac{(34-\text{s}-\text{b})\left[1-{}^{p}/_{K_T(s.T.p)}\right]-\rho(s.T.0)(51-\text{s}-\text{b})}{\left[1-{}^{p}/_{K_T(s.T.p)}\right]^2} d\Phi_{\text{s}} \quad \text{(5-Sc-II-b)}$$

where in equation (5-Sc-II-b). $v_{S_{c_{II}}}$ is northward component of the second version of saline current. f is Coriolis parameter. $z_1$is lower level of the oceanic layer. z_2 is higher level of the oceanic layer. $\rho(s.T.0)$ is density of surface ocean defined in (8). p is pressure of seawater at any point considered. $K_T(s.T.p)$ is mean bulk modulus defined in (9). (34-s-b) is equation with the same number and (51-s-b) is also equation with the same number. Φ is geopotential and subscript "s" refers to this fact that variation of seawater geopotential is affiliated to seawater salinity solely. with due attention to (35)

The first version of saline current vector was:

$$\mathbb{v}_{S_{c_I}} = -\frac{g}{f}\int_{z_1}^{z_2} \frac{1}{\frac{\rho(s.T.0)}{1-{}^{p}/_{K_T(s.T.p)}}} \mathbb{k} \times \nabla\left[\frac{\rho(s.T.0)}{1-{}^{p}/_{K_T(s.T.p)}}\right] dz \quad \text{(4-Sc-I)}$$

If we enter acceleration due to gravity inside integral sign. we get the second version of saline current: i.e.:

$$\mathbb{v}_{S_{c_{II}}} = -\frac{1}{f}\int_{z_1}^{z_2} \frac{1}{\frac{\rho(s.T.0)}{1-{}^{p}/_{K_T(s.T.p)}}} \mathbb{k} \times \nabla\left[\frac{\rho(s.T.0)}{1-{}^{p}/_{K_T(s.T.p)}}\right] d\Phi_{\text{s}} \quad \text{(4-Sc-II)}$$

Equation (4-Sc-II) is <u>*The second version of saline current vector*</u> where in it. $\mathbb{v}_{S_{c_{II}}}$ is the second version of saline current vector. f is Coriolis parameter. z_1 is depth of lower level of the oceanic layer. z_2 is upper level of the oceanic layer. $\rho(s.T.0)$ is density of surface ocean defined in (8). p is pressure of seawater at any point considered. $K_T(s.T.p)$ is mean bulk modulus defined in (9). $\mathbb{k}$ is vertical unit vector in Cartesian coordinates system. ∇ is gradient operator in Cartesian coordinates system. Φ is geopotential and subscript " s " refers to this fact that variation of seawater geopotential is affiliated to seawater saline solely.

Eastward component of the second version of saline current vector is introduced in equation (5-Sc-II-a) and northward component of it. is presented in equation (5-Sc-II-b).

From the second version of saline current vector or its components. one can perceive:

2 – 2 – 2 – A: Whatever we go from pole to equator. the second version of saline current becomes stronger (with pay attention to footnote No. 2)

2 – 2 – 2 – B: If the oceanic layer has more geopotential thickness; then the second version of the saline current becomes more powerful;
2 – 2 – 2 – C: Whatever oceanic layer is near to ocean surface; density would be lower and the second version of the saline current becomes stronger as a result;
2 – 2 – 2 – D: if the salinity of the oceanic layer would be high. the second version of saline current is less powerful and
2 – 2 – 2 – E: If the horizontal gradient of seawater salinity would be greater. the second version of saline current becomes more powerful. because the second version of saline current is proportional to the horizontal gradient of seawater geopotential thickness.
In this manner. the second version of saline current vector. i.e.. equation (4-Sc-II) shows that: "*The second version of saline current flows parallel to Isopycnals and Isopleths of implicit seawater salinity so that. low values of density (low values of salinity and high values of geopotential) are located at the right side of downstream.*" (In the northern hemisphere) This fact is demonstrated in figures 11 and 12.

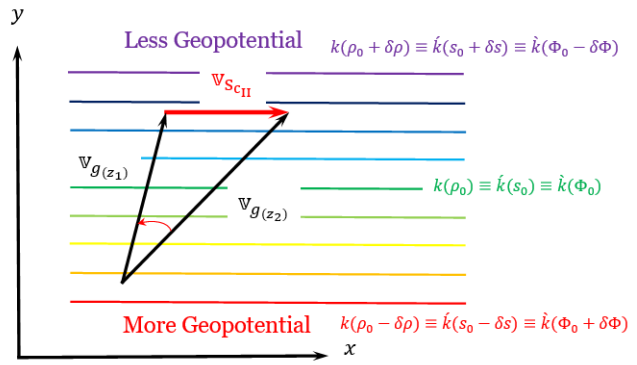

Figure 11. Counterclockwise rotation of geostrophic current with respect to depth (Backing) and more geopotential advection. Coefficient $k=-\frac{1}{f}\langle\frac{1}{\frac{\rho(s.T.0)}{1-{}^{p}/_{K_T(s.T.p)}}}\rangle(\Phi_2-\Phi_1)$. $\acute{k}$ is proportional to k in such a manner that – for instance – $k(\rho_0-\delta\rho)$ is identical to $\acute{k}(s_0-\delta s)$ and $\grave{k}$ is proportional to k in style that – for example – $k(\rho_0-\delta\rho)$ is similar in very detail to $\grave{k}(\Phi_0+\delta\Phi)$ [The second version of saline current]

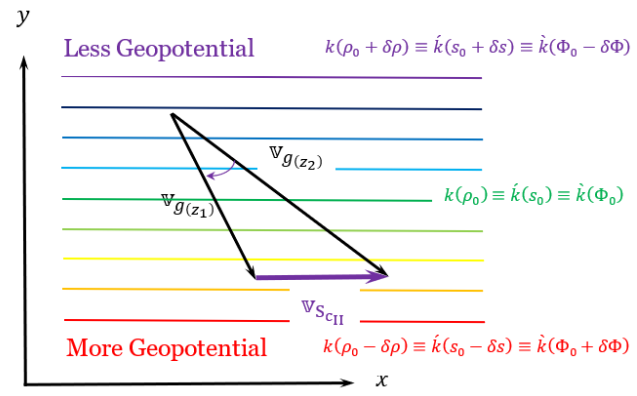

Figure 12. Clockwise rotation of geostrophic current with respect to depth (Veering) and less geopotential advection. Coefficient $k=-\frac{1}{f}\langle\frac{1}{\frac{\rho(s.T.0)}{1-{}^{p}/_{K_T(s.T.p)}}}\rangle(\Phi_2-\Phi_1)$. $\acute{k}$ is proportional to k in such a manner that – for instance – $k(\rho_0+\delta\rho)$ is identical to $\acute{k}(s_0+\delta s)$ and $\grave{k}$ is proportional to k in style that – for example – $k(\rho_0+\delta\rho)$ is similar in very detail to $\grave{k}(\Phi_0-\delta\Phi)$ [The second version of saline current]

In connection with figure 11 – considering conditions (53-2) and (53-3) – counterclockwise turning of geostrophic current with respect to depth (backing) is associated with more geopotential advection in the ocean by geostrophic current in the layer.
Conversely; as shown in figure 12 – considering conditions (53-2) and (53-3) – clockwise turning of geostrophic current with respect to depth (veering) implies less geopotential advection in the ocean by geostrophic current in the oceanic layer.

2.2.3 The third version of saline current

For deriving formulae for the third version of saline current by considering conditions (53-2). (53-3) and this fact that. variation of geopotential is related to variation of seawater salinity only; first we fix the mind on equation (5-Dc-III-a) that was eastward components of the third version of dense current i.e.:

$$u_{D_{c_{III}}}=-\frac{1}{f}\frac{\partial}{\partial y}(\Phi_2-\Phi_1) \qquad \text{(5-Dc-III-a)}$$

In equation (5-Dc-III-a). $u_{D_{c_{III}}}$ is eastward component of the third version of dense current and we used definition (2-Dc-a) for deriving this equation.
And northward component of the third version of dense current was:

$$v_{D_{c_{III}}}=\frac{1}{f}\frac{\partial}{\partial x}(\Phi_2-\Phi_1) \qquad \text{(5-Dc-III-b)}$$

In equation (5-Dc-III-b). $v_{D_{c_{III}}}$ is northward component of the third version of dense current and we used definition (2-Dc-b) for extracting this equation.
With due attention to: [3]

$$\Phi=\Phi(s.T.p) \qquad (35)$$

and emphasis on conditions (53-2) and (53-3) based upon that horizontal variation of seawater density is related to horizontal variation of seawater salinity solely. and implies variation of seawater geopotential height only by horizontal variation of seawater salinity. we get:

$$u_{S_{c_{III}}}=-\frac{1}{f}\frac{\partial}{\partial y}\left(\Phi_{s_2}-\Phi_{s_1}\right) \qquad \text{(5-Sc-III-a)}$$

where. in equation (5-Sc-III-a). $u_{S_{c_{III}}}$ is eastward component of the third version of saline current. f is Coriolis parameter. y is northward axis of Cartesian coordinates system. Φ_{s_2} is geopotential of higher level of the oceanic layer. Φ_{s_1} is geopotential of lower level of the oceanic layer and $\left(\Phi_{s_2}-\Phi_{s_1}\right)$ is geopotential thickness of the oceanic layer. Furthermore. subscript "s" refers to this fact that increasing or decreasing of

geopotential is related on seawater salinity only. with due attention to (35).
and:

$$v_{S_{c_{III}}} = \frac{1}{f}\frac{\partial}{\partial x}\left(\Phi_{s_2} - \Phi_{s_1}\right) \qquad \text{(5-Sc-III-b)}$$

where. in equation (5-Sc-III-b). $v_{S_{c_{III}}}$ is northward component of the third version of saline current. f is Coriolis parameter. x is eastward axis of Cartesian coordinates system. Φ_{s_2} is geopotential of higher level of the oceanic layer. Φ_{s_1} is geopotential of lower level of the oceanic layer and $\left(\Phi_{s_2} - \Phi_{s_1}\right)$ is geopotential thickness of the oceanic layer. Furthermore. subscript "s" refers to this fact that increasing or decreasing of geopotential thickness is related on seawater salinity only. with due attention to (35).
Now; by joining (5-Sc-III-a) and (5-Sc-III-b) as vector. we obtain:

$$\mathbb{v}_{S_{c_{III}}} = f^{-1}\mathbb{k} \times \nabla_p\left(\Phi_{s_2} - \Phi_{s_1}\right) \qquad \text{(4-Sc-III)}$$

where. in equation (4-Sc-III). $\mathbb{v}_{S_{c_{III}}}$ is: *The third version of saline current vector*. f is Coriolis parameter. $\mathbb{k}$ is vertical unit vector in pressure coordinates system. ∇_p is gradient operator in pressure coordinates system. Φ_{s_2} is geopotential of higher level of the oceanic layer. Φ_{s_1} is geopotential of lower level of the oceanic layer and $\left(\Phi_{s_2} - \Phi_{s_1}\right)$ is geopotential thickness of the oceanic layer. Furthermore. subscript "s" refers to this fact that increasing or decreasing of geopotential thickness is related on seawater salinity only. with due attention to (35).
From the third version of saline current vector or its components. one can perceive:
2 – 2 – 3 – A: Whatever we go from pole to equator. the third version of saline current becomes stronger (with pay attention to footnote No. 2)
2 – 2 – 3 – B: If the oceanic layer has more geopotential thickness; then the third version of the saline current becomes more powerful. and
2 – 2 – 3 – C: If the horizontal gradient of seawater geopotential thickness would be greater. the third version of saline current becomes more powerful. because the third version of the saline current is proportional to the horizontal gradient of seawater geopotential thickness.
In this manner. the third version of saline current vector. i.e.. equation (4-Sc-III) shows that: "*The third version of saline current flows parallel to Isopleths of geopotential thickness of the oceanic layer* i.e.. $(\Phi_{s_2} - \Phi_{s_1})$ *so that. high values of geopotential thickness are located at the right side of downstream.*" (In the northern hemisphere) This fact is illustrated in figures 13 and 14.

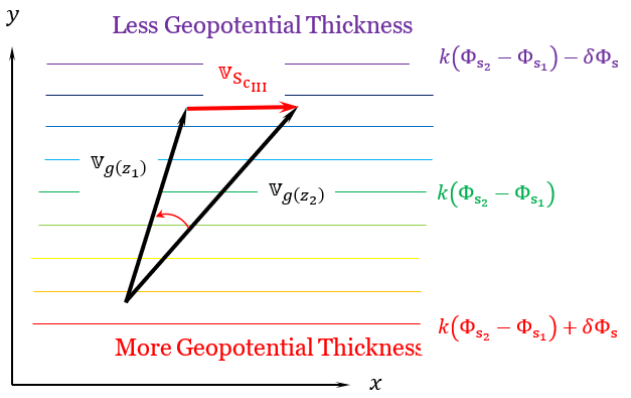

Figure 13. Counterclockwise rotation of geostrophic current with respect to depth (Backing) and more geopotential thickness advection. Coefficient $k = \frac{1}{f}$ [The third version of saline current]

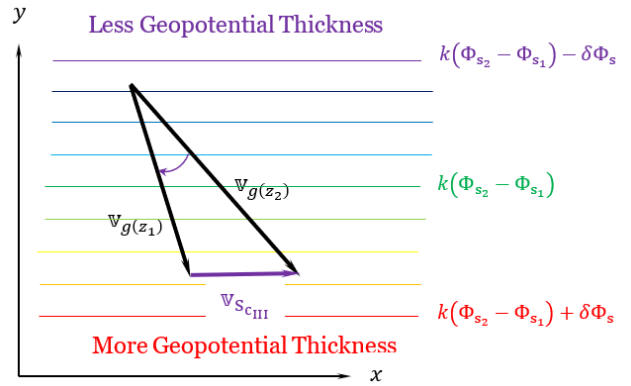

Figure 14. Clockwise rotation of geostrophic current with respect to depth (Veering) and less geopotential thickness advection. Coefficient $k = \frac{1}{f}$ [The third version of saline current]

In connection with figure 13 – considering conditions (53-2) and (53-3) – counterclockwise turning of geostrophic current with respect to depth (backing) is associated with more geopotential thickness advection of the oceanic layer by geostrophic current in the layer. Conversely; as shown in figure 14 – considering conditions (53-2) and (53-3) – clockwise turning of geostrophic current with respect to depth (veering) implies less geopotential thickness advection of oceanic layer by geostrophic current in the oceanic layer.

3. Results and Discussion

All versions of the dense current equations are extremely useful diagnostic tools. which is often used to check analyses of the observed current field for consistency.
It can also be used to estimate the mean horizontal oceanic seawater density. and thickness advections in an oceanic layer.
Dense current is struggle of the oceanic medium to return thermodynamic equilibrium and completing the dynamic cycle of ocean. This movement begins from the fact that solar radiation disturbs the thermodynamic

equilibrium of oceanic ambience. resulting production of horizontal gradient of density. Horizontal gradient of density produces horizontal gradient of potential energy and in turn. this condition forces ocean to generate horizontal gradient of pressure and finally. it causes to start current for returning thermodynamic equilibrium of the ocean.

Concerning various insolation and non-uniform transfer of diffusion of heat and salinity in the different layers of the ocean; horizontal gradients of density are not same in the oceanic layers and current velocities cannot be the same at oceanic layers. Therefore. this phenomenon produces dense current that is effort of ocean to reduce horizontal gradient of density and in turn. reducing dense current speed. By continuous reduction of dense current speed. thermodynamic disequilibrium of ocean weakens and weakens. until returning the thermodynamic equilibrium of the ocean. If we assume there will be no more solar radiation. finally the ocean current will be disappeared in presence of friction.

Some time. horizontal variation of seawater density is a result of horizontal variations of seawater temperature. This phenomenon produces a special case of dense current that we call it *Thermal current.*

Likewise. in some other case; the horizontal variation of seawater density is related to horizontal variation of seawater salinity only. This phenomenon produces another special case of dense current that we call it *Saline current.*

Thermal current and saline current can create under thermocline layer in some special conditions as well as dense current.

So. dense current and its special cases i.e.. thermal current and saline current those produced by baroclinic domain. are main response of the oceanic environment for returning thermodynamic equilibrium again. This means that. oceanic currents including geostrophic currents transfer high density seawater to location of low-density seawater. transfer high seawater temperature to low seawater temperature. likewise high seawater salinity toward seawater with low salinity region and analogically vice versa.

Therefore. transferring high density seawater to location of low-density seawater; moving high temperature seawater to region with low seawater temperature; shift seawater with high salinity to region with low salinity seawater. as well as advecting more thickness oceanic layer toward less thickness oceanic layer; have important roles for diffusing heat and salt in oceans for the purpose of balancing temperature and salinity in oceans. These conditions are important duties of oceans toward regulating of world climate balance.

Also. dense current vector equations. equations of eastward component of dense current and equations of northward component of dense current show:

3 – 1 – At any time density varies in horizontal direction. by horizontal variation of temperature. salinity or pressure. i.e.. all time we confront by baroclinic medium; therefore. always there are dense current. thermal current or saline current too;

3 – 2 – Whatever we approach to tropical latitudes. dense current. thermal current or saline current will be powered (with pay attention to footnote No. 2);

3 – 3 – Whatever we close to ocean surface – for reason of light density - dense current. thermal current or saline current has more force;

3 – 4 – If there is high horizontal gradient of density. high horizontal gradient of temperature or more horizontal gradient of salinity; dense current. thermal current or saline current has more strength respectively. and

3 – 5 – If there is more horizontal gradient of thickness of the oceanic layer; then dense current. thermal current or saline current has more power.

Likewise. the propositions of dense current. thermal current or saline current those are propounded with above-mentioned configurations; can help to better understanding of ocean dynamics. Furthermore. knowing the advections of the heavy seawater density. light seawater density. high temperature seawater. low temperature seawater. high salinity seawater. low salinity seawater or advection of the thickness of the oceanic layer with exclusive specifications; can help to improve oceanic forecasting. Although. we referred to the variation of the geostrophic current with respect to depth here; but this proposition is valid for the variation of real oceanic current in vertical direction with some modifications that needs separate discussion.

And study of dense current. thermal current or saline current can enlighten deep sea dynamics and helps to better understanding climate of deep oceans.

4. Conclusions

Ocean currents are powerful and dynamic systems that drive the Earth’s climate. affect marine life. and transfer vast amounts of energy around the globe. A better understanding of these currents can greatly improve our ability to predict and respond to extreme weather events while helping us make smarter decisions when planning for future growth and development. It is also important to remember that ocean currents play a key role in regulating global temperatures by moving heat from the equator to poleward regions as well as regulating global ocean’s salinity.

Many phenomena and mechanisms have essential roles for transfer and diffusion of arriving solar radiation from tropical regions to high latitudes in northern hemisphere and low latitudes in southern hemisphere.

The most important of these mechanisms are: winds. ocean currents. sensible heat. latent heat. monsoon phenomenon (as other type of latent heat transfer).

tropical cyclones. meridional overturning circulation. Rossby waves and Antarctic circumpolar current.

Oceanic currents are second mechanism for transferring sensible heat of solar radiation from tropical regions toward high or low latitudes of the earth in northern hemisphere and southern hemisphere. And; in comparison with the first mechanism for transferring sensible heat from tropical regions to high or low latitudes. i.e.. wind; the minimum transferring of heat by ocean current per unit volume is 3395 times and maximum transferring heat by ocean current per unit volume is 4688 times as long as transferring heat by wind.

Therefore. research about dense current. thermal current or saline current is vital for understanding heat and saltiness balance in oceans and study of world climate via deep oceans.

In classification; dense current. thermal current and saline current are classified in thermohaline circulation. This kind of ocean circulation is driven by differences in water density. The cold. dense water sinks to the ocean floor and is replaced by warm. less dense water from the surface. This movement of water can occur on a global scale. with water sinking in the polar regions and rising in the tropics. as well as on a more local scale.

Overall. these currents play a vital role in the ocean's ecosystem. climate and weather patterns. and human activities. They also have a major influence on the distribution of heat. carbon and other elements in the ocean. and they support marine life. Understanding these currents is important for managing resources and predicting future changes in the ocean's environment.

Atmospheric movements (winds) and oceanic movements (currents) are some parts of the mechanisms those try to adjust heat. humidity and salinity in Atmosphere-Ocean System. Even different shear of them (movements) including their vertical shear; have basic roles in the subject.

Our goals in this article were familiarizing with oceanic efforts for transfer of sensible heat via dense current. thermal current and saline current those are vertical shear of geostrophic current in baroclinic ocean with specific conditions. And this work helps us to better realize oceanic climate.

Separation of oceanic currents same as real oceanic current. geostrophic current. dense current. thermal current and saline current is not easy. To separate them for understanding their effects. we need to use oceanic model with high accuracy for knowing the type of ocean current. And preparing this kind oceanic model. is essential necessity and vital for our society.

It is necessary to note the basic point. Atmosphere and oceanic waters are baroclinic. And the theory of barotropic ambience – same as geostrophic balance – is acceptable for simplification of meteorological and oceanic analyses.

However. baroclinic environment. geostrophic current and variation of it with respect to depth. definition of thermal current and saline current. deriving of thermal current vector in Cartesian coordinates system as well as deriving saline current vector in this coordinates system. the other view to derive equation of thermal current and saline current. other view of relation between thermal current and geopotential thickness. also relation between saline current and geopotential thickness. have been discussed expanded upon the article.

5. References

[1] Zamanian. M. T.. 2023: A New Look at the Vertical Shear of the Geostrophic Current. Part I: Dense Current. *International Journal of Coastal. Offshore and Environmental Engineering*. Vol. **8**/No. 3/Summer 2023 (49-62)

[2] Zamanian. M. T.. 2022: A New Look at the Vertical Shear of the Geostrophic Wind. Part I: Dense Wind. *International Journal of Coastal & Offshore Engineering*. Vol. **7**(**3**). 10-19 pp.

[3] Zamanian. M. T.. 2023: A New Look at the Vertical Shear of the Geostrophic Wind. Part II: Thermal wind and Moist Wind. *International Journal of Coastal. Offshore & Environmental Engineering*. Vol. **8** (**2**). 21-39 pp.

[4] Pedlosky. J.. 1998: *Ocean circulation theory.* Berlin. Springer. xi + 453 pp.

[5] Holton. J. R. and. G. J. Hakim. (2013). *An Introduction to Dynamic Meteorology*. Amsterdam. 5th edition. Elsevier. xvi + 532 pp.

[6] Apel. J. R.. 1999: *Principles of Ocean Physics.* San Diego. Academic Press. xiii + 634 pp.

[7] Marshal. J. and R. A. Plumb. 2008. *Atmosphere. Ocean. and Climate Dynamics. An Introductory Text.* Amsterdam. Elsevier. xx + 319 pp.

[8] Gill. A. E.. 1982: *Atmosphere-Ocean Dynamics.* San Diego. Academic press. xv + 662 pp.

[9] Pedlosky. J.. 1987: *Geophysical Fluid Dynamics.* 2nd edition. New York. Springer. xiv + 710 pp.

[10] Ghil. M. and E. Simonnet. 2020: *Geophysical Fluid Dynamics. Dynamical Systems and the Climate Sciences.* Paris. European Union. 80 pp.

[11] Simmons. G. F.. 1985: *Calculus with Analytic Geometry.* New York. McCra-Hill. xxi + 950 pp.

[12] Curry J. A. and P. J. Webster. (1999). *Thermodynamics of Atmosphere and Oceans.* San Diego. Academic Press. xvii + 471pp.

[13] Pond. S. and G. L. Pickard. 1983: *Introductory Dynamical Oceanography.* Amsterdam. 2nd edition. Elsevier. xx + 329 pp.

[14] UNESCO. "The Practical Salinity Scale 1978 and the International Equation of State of Seawater 1980. Tenth Report of the Joint Panel on Oceanographic Tables and Standards." UNESCO Technical Papers in Marine Science No. 36. UNESCO. Paris. France (1981).

INTERNATIONAL JOURNAL OF
COASTAL, OFFSHORE & ENVIRONMENTAL ENGINEERING IJCOE Vol.9 /No.1 / winter 2024(25-30)

vailable online at: www. Ijcoe.org Manuscript Type: Original Research Article

Modern tectonic events in near-bottom sediments of the Middle Caspian Sea

Victoria A. Putans [1], Hadi Gerivani[2*]

[1] *Shirshov Institute of Oceanology, Russian Academy of Sciences, Moscow, Russia.*
[2*] *Iranian National Institute for Oceanography and Atmospheric Science, Tehran, Iran, gerivani@inio.ac.ir*

ARTICLE INFO

Article History:
Received: 08 Aug. 2023
Accepted: 12 Jan. 2024

Keywords:
Earthquakes
Seismoacoustic
Sediment structure
Degasation
Active tectonic

ABSTRACT

The Central Caspian western border is a seismically active region with contrasting combinations of mountain clinoforms and troughs. Intense troughing started here at the end of the Pliocene and remained uncompensated by sediments. Using high resolution seismoacoustic profiles associated with earthquake catalogs and also some additional data, this study investigated the correlation between modern seismic events and deformation structures in the seabed sediments of the Derbent Basin in the western part of the Middle Caspian Sea. The results showed that the seismic activity and the sediment disruption vary across the basin, and can be classified into four areas: single deformations, western slope, deep basin north-east area, and deep basin south area. The study revealed that the Caspian Sea is a tectonically active region, and that the seismic events can trigger high pressure and hot fluid to seep through the weak zones in the sediments. This paper also presents some interesting observation on seismoacoustic profiles including tens of disruptions in sediment structure and disjunctions in seafloor relief, fault groups, gas pipes, and horizontal zones of non-correlation.

1. Introduction

Caspian Sea is a hydrocarbon basin of great value. But there is a great variety of exploration problems as well. One of the problems is microseismicity and shallow tectonic movements. Every natural process is responsible for some geological forms, which could be seen on seismic sections. North and Central Caspian Sea shows distinct zones of different geological environments, which are connected with different geohazards [1, 2]. Assessment of the stability of the Quaternary sediments on continental slopes in the Central Caspian Basin has high practical value in light of intense hydrocarbon surveys and exploration. In the Central Caspian with medium water depths around 400 m, mainly the pipeline projects are facing with the problems caused by natural geohazards in compare to the construction projects. The fields are in the center of the Sea with a relatively calm environment but pipelines have to be stretched long routs along seabed with different sediments, geological features and various natural processes which usually associated with hazardous conditions. For a pipeline project, it is very important to investigate slopes stabilities and sediment transport pattern along pathways of the pipe [3].

Modern tectonic movements lead to deformation both in sediment cover as a whole and in local near-bottom layers. In addition to powerful earthquakes which is well known that can trigger submarine huge mass movements, mud volcanoes and etc., repeatedly occurring earthquakes with low magnitude (<6) may activate different types of landslides and mudflows in seabed [4]. The Central Caspian area is considered as seismically active area with powerful earthquakes reported in the western border in Caucasus mountains, but most of the earthquakes occurred in the Derbent basin have magnitude less than 6 on the Richter scale [5, 6] The aim of this paper is to establish connection between already-known sediment forms and geohazardous processes of microseismicity and modern active tectonics in the central Caspian Basin.

2. Physical Setting

The Caspian Sea has the Caucasus mountain system on the west, the vast steppe of Central Asia on the east, the Russian platform on the north and the Alborz Mountains on the south. The sea has no connection with World Ocean, but is too large (1200km x 300km) to be called a lake. The present water surface is 28 m

below the world ocean level. Geomorphologically, the Caspian Sea can be divided into three regions (fig. 1).

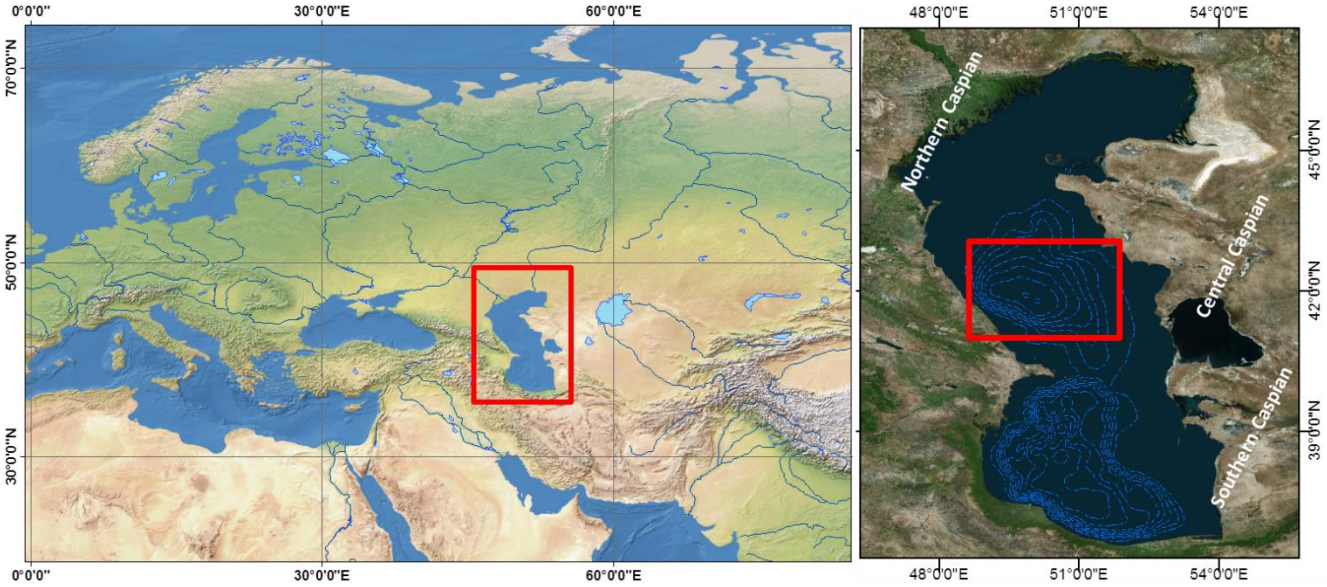

Figure 1. The position of the study area in the Caspian Sea.

The boundary between the northern and central parts is the Mangyshlak Threshold (a large sediment body) and between the central and southern parts is the Apsheron threshold (a tectonic sill).

The Middle Caspian Depression that has been considered in the present study is quasi-oval shape, extending in a NNW direction over a distance of 450 km with wide of 100-200 km. It is characterized by a slightly steeper near-Caucasian slope, with the deepest part also shifted towards the Caucuses Mountains. The depression is filled with Jurassic-Quaternary sediments up to 8–10 km thick with a maximum thickness registered in the band adjacent to the Dagestan coast. The sedimentary cover is underlain by a partly deformed Permo-Triassic rock complex and metamorphosed basement of Paleozoic and, probably, older age. The crust beneath the Middle Caspian Basin is approximately 40 km thick, whereas the thickness of the lithosphere is 150 km [7, 8].

The Caspian depression crosses structural elements of different origins. The seismogenic zone distribution correlates well with fields of modern tension in the Caucasus region and with the most likely directions of lithospheric mass movement (mostly northwest) [9]. The Central Caspian has relatively high seismicity because its western border is the seismically active Caucasus mountain system. The earthquake magnitude on the western slope can reach 6-7 on the Richter scale [5].

Based on the pattern of earthquakes below the borders of modern structures, Ivanova and Trifonov [10] distinguished several seismotectonic areas on the Caspian Sea (fig. 2). According to this classification, the area of the present research is situated in seismotectonic area I. This is an area with contrasting combinations of mountain clinoforms and troughs. Intense toughing was started here at the end of the Pliocene and remained uncompensated by sediments .

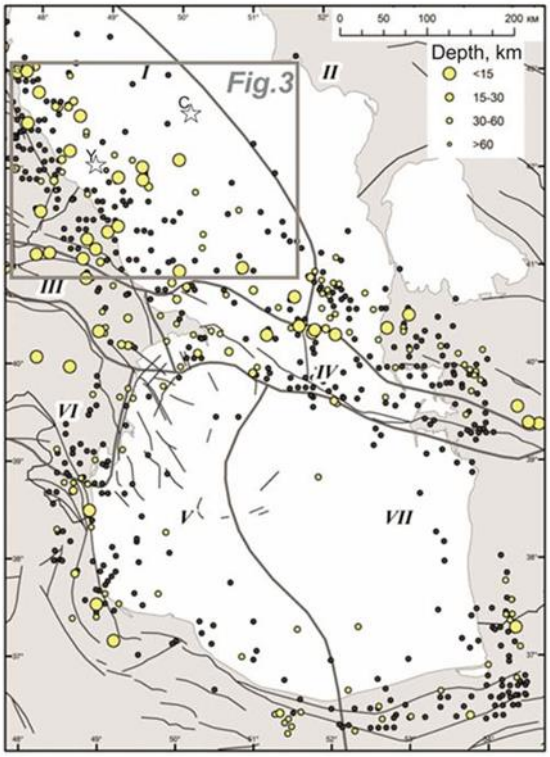

Figure 2. Seismotectonic provinces I-VII (by Ivanova and Trifonov [10]) and distribution of earthquake epicenters: black for earthquakes before 1998, yellow for 1998-2017. Thin black lines are for main tectonic faults.

3. Material and Methods

Seismoacoustic method used in this study to survey seabed sediments and features is a branch of "shallow" seismic applications which sometimes called sub-bottom profiler. It uses acoustic waves of much higher frequency (kHz) than "big" seismic waves, which are tens and hundreds of Hz [11]. "Shallow" means that the seismic profile provides information about the upper parts of the sediment cover, e.g. 150 m below sea bottom only, but the resolution can reach tens of centimeters (some SES data). The profiles used in this study were obtained by Shirshov Institute of Oceanology in 2004-2013, by single-channel seismic profiling system GEONT with multielectrode sparker and parametric echo-sounding SES-2000-standard (Tab. 1). The position of the profiles were used in this study are presented in figure 3. The collected seismic reflection data were processed using the RadExPro seismic processing program with standard algorithm (muting, filtration, sometimes deconvolution). Interpretation was performed using Kingdom software.

Deep drilling log data for two hydrocarbon sites including Centralnaya and Yalama were used here to confirm the observation where it is necessary but unfortunately we are not allowed to publish these log data (fig. 3).

The earthquake catalogues from the last 150 years [12,13,6] were used to evaluate the modern tectonic activity. All recorded and reported seismic events during the period of 1998-2017 including more than 500 earthquakes with magnitude more than 3 on the Richter scale were selected and analyzed to achieve the goal of this study.

Table 1. Specifications of the seismic instruments used for geophysical surveys

Instrument type	Function	Frequency range, kHz	Penetration (depend on sediments), m	Vertical resolution, m
Sparker	Seismic profiler	0.2-0.7	50 – 300	2-3
SES–2000 standard	Echo-sounder + Seismic profiler	100 4-12	10 – 50	0.05-0.15

4. Results

The study concerns western part of tectonic province I (fig. 2, 3), where the sediment cover has maximum thickness of 14 km with Pliocene-Quaternary part of 5 km. In general, most of the earthquake epicenters are concentrated in western side of the Middle Caspian Sea (fig, 3) and all have depth no more than 75 km. The most of the earthquakes in selected area have focus depth about 5-15 km and magnitude of 3.5-4 on the Richter scale which could be interpreted as signs of a technically active zone in the rigid basement. However, there are several events in the "calm" area of deep basin with focus depth of 0-5 km and magnitude about 3.5.

Using the seismoacoustic profiles from the selected area (fig.3), many disruptions were revealed in sediment structure and in seafloor relief. In general, it is possible to distinguish three disruption types: first, faults and fault groups (fig.5, 6, 7) that are mainly situated in near- bottom layers, second, horizontal zones of non-correlation (fig. 4, 7) that are disturbed acoustic horizons on the two-way time (TWT) depth from 0.8 to 1.3 ms, and third, "gas pipes" (fig.7) that are vertical structures with roots in disturbance layers. For all these objects, there is a clear geographical pattern of three areas: 1) the western slope of the Derbent basin, 2) deep part of the Basin near the southern slope, and 3) eastern part of the Basin. There are also single objects of interest (six). Some profiles represent one object from different sides, but mostly there are single crossings (see the position of profiles on fig.3).

Field measurement of water column properties in the Central Caspian basin showed anomalous values of temperature salinity and sound velocity close to seabed which can help our understanding of the characteristics of the fluids that come out of the seabed (fig. 4).

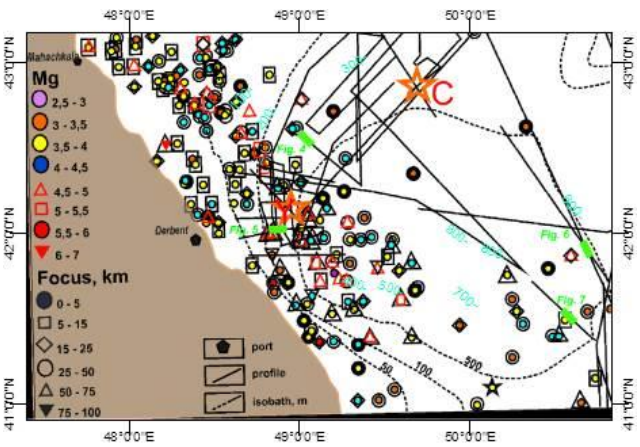

Figure 3. Position and characteristics of the earthquakes and location of seismoacoustic profiles in the area of interest. Stars show two hydrocarbon drilling sites with deep stratigraphic and geophysical data called: Centralnaya (C) and Yalama (Y).

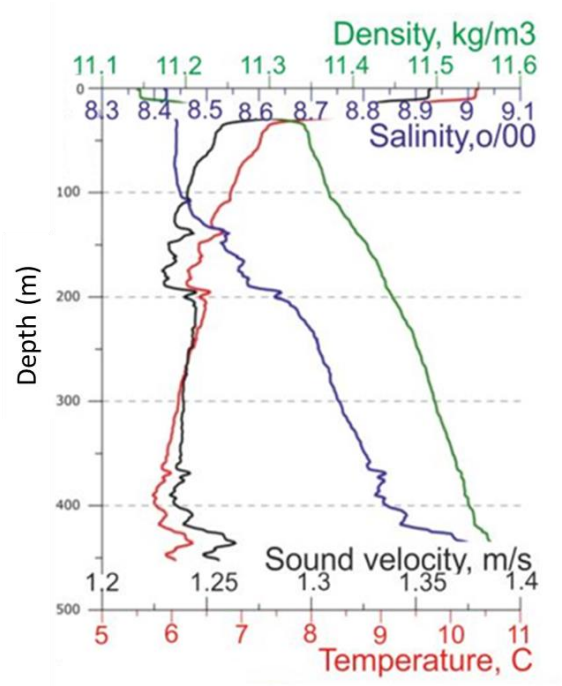

Figure 4. Physical properties of water column measured in the Central Caspian Basin (After [14]).

5. Discussion

Distribution maps of modern seismic events and disruptions in seabed sediment structure were evaluated and showed significant correlation between modern tectonically activities and prominent seismic events with deformation and features observed in seabed sediments. The characteristics of the observed phenomena are different around the basin and can be classified as discussed in the following.

5.1. Single deformations

Nearly all single deformations in sediments have nearby earthquake events with focus depths on 0-5 km (fig.3). The most spectacular deformation is located in northwest of the Mangyshlak Threshold and appears to indicate long lived fault (red lines in fig.5) with several stages. In addition to this fault, seismic data shows groups of minor sub vertical disruptions (however that could be slumping) and horizontal zones of non-correlation (disturbed layer on TWT 0.8 to 0.9 ms). The nearest earthquake is double (Mg 4-4.5 events) and situated several kilometers to the northwest (fig.3). We interpret the objects as evidences of modern on-going tectonic events, occurring due to repeatedly throwing and re-compensation processes in sediment cover.

5.2. Western Slope

Deformation structures in the sediments of the western slope of Derbent Basin correlate with earthquake events with magnitudes from 3.5 to 5. Alongside with sediment waves and reworking zones, seismoacoustic sections show mainly disjunctions of different amplitudes, several unclear “pipes” and some “non-correlated” zones (fig. 6). Object diversity is caused by peculiarities in the western slope relief and the proximity of Caucasus mountain system. In the north-western part of the Derbent slope most focuses have depth about 20 km, magnitudes of 3.5-4 (fig.3) and disjunctions are slight, but to the southeast, magnitudes reach to 4.5-5 with a single event of 6.1. On seismic profiles, there are some vertical zones that seem very similar to “pipes” and also faults that become more prominent and look more like grabens (fig. 6). Focus depths here are from 50 to 75 km. In spite of nearby presence of Caucasus Mountains, it seems that the tectono-stratigraphic processes in this area can be connected with observation on the deep well-log data of Yalama hydrocarbon site.

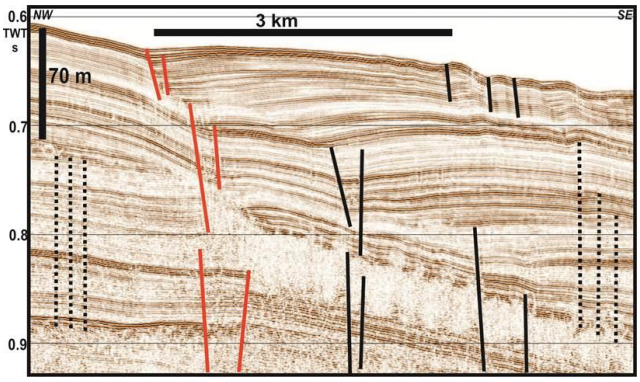

Figure 5. Seismoacoustic profile on Mangyshlak threshold. Red lines indicate long live fault zone.

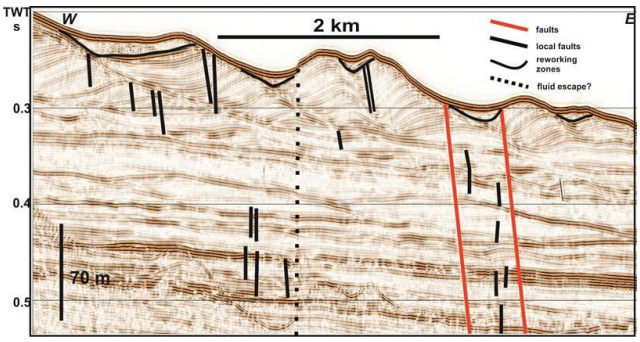

Figure 6. Seismoacoustic profile recorded on the Western Derbent slope

5.3. Deep basin: north-east area

In this area earthquake events are rare, with an average magnitude of 4 and a single event of 5.3 (fig.3). The depths of most focuses are approximately 5 km, but some are 50 km. Seismoacoustic sections show several vertical zones of disturbance with “transparent” wave field which could be interpreted as “gas pipes” and associated with slight vertical disruptions in some places which can be local faults. The sediment strata are undisturbed and well-stratified, with consistent horizontal reflectors (fig. 7). The Caspian Sea has high hydrocarbon potential, thus,

degasation processes are inevitable. it seems that earthquakes even of low magnitude can generate new faults and re-activate existing ones, and via these disruptions high pressure fluids resulted form, degasation processes can unloaded.

5.4. Deep basin: south area (Apsheron Threshold base)

In the southernmost area of Derbent Basin, earthquake events are rare with average magnitudes of approximately 4 which mostly have depths of 0-75 km (fig.3) and located mainly to the south-east nearby tectonic-originated Apsheron Sill. On seismoacoustic sections, there are plentiful "gas pipes", series or vertical disruptions, and acoustically heterogeneous layers with chaotic packages below (fig.8). Also seismoacoustic sections shows that stratified sediment cover underwent post-sediment deformations. Field measurements of physical properties of water column showed temperature and salinity anomaly close to seabed over the area of study (fig. 4). We interpret these post-sediment structures as paths for high pressure, hot and saline.

6. Conclusions

This paper examined the relationship between modern seismic events and deformation structures in the seabed sediments of the Derbent Basin in the western part of the Middle Caspian Sea, using high resolution seismoacoustic profiles, earthquake catalogs, and some other data. The findings indicated that the basin has different levels of seismic activity and sediment disruption, which can be divided into four areas: single deformations, western slope, deep basin north-east area, and deep basin south area. The paper showed that the seismic events can cause seepage of high pressure fluid through the weak zones in the sediments. The paper also reported some interesting features on seismoacoustic profiles, such as numerous disruptions in sediment structure and seafloor relief, fault groups, gas pipes, and horizontal zones of non-correlation.

The Caspian Sea has high hydrocarbon potential; thus, degasation processes are very possible. Strong earthquakes can generate new faults and re-activate existing ones, and via these disruptions fluids are luid seeps that had occurred during periods of high seismic activity. After that even slight seismic events (of magnitude <6) can provoke high pressure fluids to pass through the weak zones mainly including faults and "gas pipes" [14].

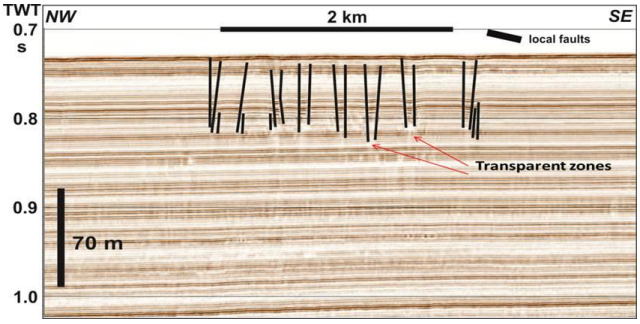

Figure 7. Observation on seismoacoustic profiles in the north-eastern area of Deep basin.

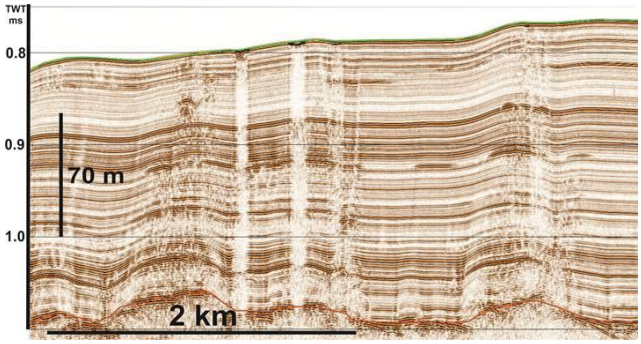

Figure 8. Seismoacoustic profiles in the southern slope of the Central basin (Apsheron Sill).

the deformation effects of modern seismic processes [15, 16]. In the case of Central Caspian, weak (average magnitude 4) and shallow (average depth 20 km, rare 75 km) earthquakes cause disruptions in the upper part of sediment strata.

In most cases, disruptions are coupled with signs of fluid activity such as non-correlation zones. These zones follow faults and/or "acoustically weak zones", and on acoustic sections these zones appear as disrupt areas. Most likely, earthquake displacements and shakings which caused by unloading of stress in deep horizons, generate series of local faults through all strata near to seabed where high pressure fluids can escape from sediments. If fluid migrates by lateral migration, non-correlation zones may occur hundreds kilometers from the seismic activity point.

At the end it should be noted that the results of such basic researches can be useful for many different field of studies [17, 18].

Acknowledgments

The Authors are thankful to Russian Shirshov Institute of Oceanology (project of Federal Program: FMWE-2024-0019) and Iranian National Institute for Oceanography and Atmospheric Science (INIOAS) (Project No. 396-012-01-029-01 and 396-012-01-08-03) for supporting this work.

References

[1] Putans V.A., Merklin L.R., Levchenko O.V. (2010) Sediment waves and other forms as evidence of geohazards (Caspian Sea). International Journal of Offshore and Polar Engineering. Vol.20, No.4, December 2010, pp1-4 ISSN 1053-5381

[2] Gerivani, H., Putans, V.A., Merklin, L.R. and Modarres, M.H., 2021. Characteristics of features formed by gas hydrate and free gas in the continental slope and abyssal plain of the Middle Caspian Sea. Marine Georesources & Geotechnology, 39(4), pp.419-430.

[3] Jeng, D.S., Zhang, J. and Kirca, Ö., 2020. Coastal Geohazard and Offshore Geotechnics. Journal of Marine Science and Engineering, 8(12), p.1011.

[4] Zitter, T.A.C., Grall, C., Henry, P., Özeren, M.S., Çağatay, M.N., Şengör, A.M.C., Gasperini, L., de Lépinay, B.M. and Géli, L., 2012. Distribution, morphology and triggers of submarine mass wasting in the Sea of Marmara. Marine Geology, 329, pp.58-74.p.1011.

[5] Lobkovskii L.I., Verzhbitskii V.E., Merklin L.R. et al. (2009) Slump structures in Quaternary deposits on northern slope of Derbent basin. Oceanology 49: №3: 430-439 DOI: 10.1134/S0001437009030126

[6] Ulomov V.I., Medvedeva N.S. (2014) Specialized catalogue of Northern Eurasia earthquakes http://seismos-u.ifz.ru/documents/Eartquake-Catalog-СК3.pdf

[7] Mir N. 2005. English Version of Explanatory Notes of International tectonic map of the Caspian Sea region (scale 1:2500000). Moscow: Russian Academy of Science.

[8] Gerivani H., Putans V., Ivanov A. Hydrocarbon fluid seepage controlled by active tectonic: Observations in the Derbent Basin of the Caspian Sea. XXIII International scientific conference “Marine geology school” Moscow, 8 - 22 November, 2019.

[9] Panina, L.V. and Zaitsev, V.A. Moscow Univ. Geol. Bull. (2014) 69: 11. https://doi.org/10.3103/S0145875214010074.

[10] Ivanova T.P., Trifonov V.G. (2002) Seismotectonics and modern sea level change of Caspian sea. Geotectonics, Vol. 36, No. 2, 2002, pp. 109–123. Translated from Geotektonika, No. 2, 2002, pp. 27–42

[11] Putans V.A., Levchenko O.V., Merklin L. R., Pleshkov A.Yu. (2013) Seismoacoustic anomalies in sediments of western Russia seas. Modern problems of science and education №6 /111-10597

[12] Catalogues of urgent report service of Geophysical Service RAS. http://www.ceme.gsras.ru/cgi-bin/new/catalog.pl?l=1

[13] Dagestan chapter of Federal geophysical service, General catalogue of seismic events http://dbgsras.ru/site/earthquake?nofilter=1

[14] Putans, V.A., Trimonova, M.A. and Merklin, L.R., 2023. Hidden hydrosphere under the Caspian Sea: Geophysical evidence and sea-level influence. Interpretation, 11(1), pp.T181-T188.

[15] Firoozfar A., Bromheaad E.N., Dykes A.P. (2012) Caspian sea level change impacts regional seismicity. Journal of Great Lakes Research, vol.38, issue 4: 667-672 https://doi.org/10.1016/j.jglr.2012.09.004

[16] Chen J.L., Pekker T., Wilson C.R. et al, (2017) Long-term Caspian Sea level change. Geophys. Res. Lett, 44. 6993-7001 DOI: 10.1002/2017GL073958.

[17] Rashidi Ebrahim Hesari, A., & Rahime, M. (2021). Evaluation and validation of wind energy extension (Bahooz) in Manjil region, Iran. International Journal Of Coastal, Offshore And Environmental Engineering (ijcoe), 6(5), 76-88. DOI: 10.22034/ijcoe.2021.153621

[18] Raoufi, M., Zanganeh Ranjbar, P., & Mehrdad, A. (2021). Evaluation of SSG breakwaters on the southern shores of the Caspian Sea to produce sustainable energy. International Journal Of Coastal, Offshore And Environmental Engineering (ijcoe), 6(5), 64-75. DOI: 10.22034/ijcoe.2021.152617

INTERNATIONAL JOURNAL OF
COASTAL, OFFSHORE & ENVIRONMENTAL ENGINEERING IJCOE Vol.9/No. 1/Winter 2024 (31-42)

Available online at: www. Ijcoe.org Manuscript Type: Original Research Article

Investigation the Surface Waves During the Indian Ocean Summer Monsoon in the Chabahar Offshore Area Using Numerical Modeling

Mohammad Pakhirehzan[1], Hossein Malakooti[1*]

[1] Faculty of Marine Sciences and Technology; University of Hormozgan, Bandar Abbas, Iran
Corresponding Author: malakooti@hormozgan.ac.ir

ARTICLE INFO

Article History:
Received: 19 Oct. 2023
Accepted: 15 Jan. 2024

Keywords:
COAWST
Indian Ocean Monsoon
MIKE SW
SWAN
WRF

ABSTRACT

Spectral and statistical analyses of wind-induced waves are very important in the design of coastal and offshore structures. In this study, the results of numerical simulations by two spectral wave models (MIKE SW and SWAN) were compared to investigate the effect of the Indian Ocean summer monsoon on wave patterns in the Chabahar offshore area in the northern Gulf of Oman. The wind field for the wave simulations was obtained by the WRF model. WRF and SWAN were implemented as wave-atmosphere subsystems of the COAWST (Coupled Ocean–Atmosphere–Wave–Sediment Transport model). For MIKE SW wind input, the output wind field of the WRF model was extracted and converted to the readable format. The results of the wave simulation are acceptable by both the COAWST and MIKE SW experiments in comparison with observational data, but the results of the COAWST model were more accurate than the results of MIKE SW in simulating wave height and period, while in simulating wave direction, MIKE SW was more accurately than COAWST. The wave spectrums were prepared for observational data and model results. All Spectrums had a single peak which means that one main frequency is responsible for the most wave energy. The best-fitted spectrum was JONSWAP for all occasions. This means that the sea state of the study area was not a fully developed sea during the simulation period. Directional wave spectrums of observational data and model results showed the south and southeast directions for the wave energy propagation.

1. Introduction

The winds over the northern Indian Ocean generally blow from the southwest during May-September (summer monsoon) and from the northeast during November–February (winter monsoon). The wind force is much stronger during the summer monsoon than during the winter monsoon [1]. Monsoons denote significant seasonal variations in winds and precipitation [2].

The ocean response to the surface severe winds is always associated with extreme wave heights, large current velocities, and substantial water level variations [3]. A fast-varying wind forms complex ocean wave fields which can propagate thousands of kilometers away from the storm center, resulting in dramatic variations of the wave field in space and time [4]. Determination of wind-induced wave conditions is a very important factor because of its impacts on economic, societal, and other human activities in coastal areas [5].

Due to the increased performance of computational resources, the use of numerical models to predict natural events is becoming more prevalent [6]. Nowadays, wave characteristics are estimated using numerical models, because of the lack of measurements in many regions [7]. Numerical simulation is among the major methods employed to study the surface wave field under the action of a tropical cyclone. The study of the surface wave field during tropical cyclones relies on the development of the wind-wave model [8]. There are many spectral wave models for wave forecast studies in the open ocean as well as in the coastal area [9]. The accuracy of the results of wave models is strongly dependent on the wind fields [10-11].

Many studies have been done to develop numerical models to study and predict environmental phenomena from a variety of temporal and spatial scales (e.g. [12-20]). In general, researchers in these studies have used three methods to implement modeling. Some have used one model (such as

WWIII, SWAN, MIKE SW, WAM, ROMS, STWAVE, etc.), some have compared the results of two models, and some have used the results of coupled models (including atmosphere, ocean, and waves models) simultaneously. The results obtained from all three methods were mostly acceptable. Of course, regarding the use of the third method (coupled models), the results are at a more favorable level than the other two methods. A set of models that can develop the interaction between the atmosphere, the ocean, and the waves will give better results. Coupled systems allow the effects of larger-scale processes to directly influence the smaller-scale response and allow sensitivity experiments to exchange prognostic variable fields between model components. Coupling of models is a sure and simple way to increase a model's complexity [6]. However, some models of the first method also give good results if correct physical components, calibration, and accurate wind field are used.

In this study, a combination of the above three methods is used. For this purpose, the simulation results in the Chabahar offshore area in the northern Gulf of Oman during the Indian Ocean summer monsoon by a coupled atmosphere-wave (SWAN [21] and WRF [22]) model as a subset of COAWST [6] have been compared with the results by the MIKE SW model [23]. The waves obtained by the COAWST are a result of the simulated wind (U_{10}, V_{10}) by the WRF applied to the simulation area by SWAN, and this wind, in turn, is affected by the roughness coefficient, which determines by the wave height and wavelength sent from the SWAN to the WRF. The SWAN model can be run individually, but researchers who have used coupled model have claimed that coupling is more accurate than individual execution in addition to saving time ([6, 24-28]). Also, the waves obtained by MIKE SW are the result of simulated wind (U_{10}, V_{10}) which are extracted from the results of the WRF model and converted into a format that can be read by the MIKE SW model.

The WRF model is designed and presented for numerical simulation of the atmosphere. The WRF supports several dynamical and physical parameterizations that allow for the various configurations, tailored to atmospheric studies [22]. The SWAN and the MIKE SW are known as two widely used, well-tested spectral wave models for near-shore simulations. Both models represent the generation, propagation, and dissipation of waves and include the effects of refraction and shoaling on wave propagation, accounting for wave dissipation by white-capping, wave-wave interactions, bottom friction, and depth-induced wave breaking [29]. The SWAN model is presented for use in an enclosed sea, although it was initially designed primarily for use in coastal environments [30]. The MIKE SW model is based on a flexible mesh, which allows for coarse spatial resolution in the offshore area and high resolution in the shallow coastal waters [31].

SWAN can be run on both structured and unstructured grids, its spatial discretization is based on a vertex-centered method, and the control volume in SWAN is a polygon, while MIKE SW only uses unstructured grids, its spatial discretization is a cell-centered method, and the control volume in MIKE SW is triangular. The major difference between the numerical methods is that the SWAN uses fully implicit method time integration whereas MIKE SW is an explicit approach [23, 32, 33].

Comparison of wave simulation results by different models has been studied by various authors. Strauss et al. [34] presented comparative simulations by SWAN and MIKE SW in the Gold Coast of Australia. They claimed that model simulations are compared with observed data from existing wave recording buoys. Their results showed that the inclusion of wind in the modeling undertaken did not improve the model's accuracy and winds over 10 m/s led to an overestimation of significant wave height while increasing the processing time. Moeini and Etemad-Shahidi [7] compared the results of wave parameters simulation by SWAN and MIKE SW for Lake Erie in the United States. They used a field data set of Lake Erie for testing the performance of the simulations. They claimed that the average scatter index of SWAN was about 16% for significant wave height and 19% for peak wave period; while the average scatter index of MIKE SW was calculated about 20% and 13% for significant wave height and peak wave period, respectively. Both models were also evaluated for the prediction of wave direction and it was found that MIKE SW results are slightly more accurate than those of SWAN. Montoya et al. [35] performed a comparison between WAVEWATCH III and SWAN, using data from Hurricane Katrina in the Gulf of Mexico. They simulated sea surface directional wave spectrum and other wave parameters and their relation with the drag coefficient. They compared simulated data with in-situ buoy data. Their results showed that the WAVEWATCH III presented the best statistical comparisons for the main wave parameters, such as significant wave height and peak wave period, and the SWAN model tends to overestimate the maximum values for significant wave height for some buoys and the peak wave period for almost all the buoys. Fonseca et al. [36] presented results of wave characteristics simulation in shallow waters by MIKE SW, SWAN, and STWAVE models in the Portuguese coasts. In situ measurements from buoys and Acoustic Doppler Current Profilers (ADCP) were used to validate the model simulations. The researchers claimed that, both MIKE SW and SWAN are complex models and have a large set of formulations and parameter choices, and STWAVE produced good

results and is considerably faster than the other models.

This study is structured as follows. The study area is presented in the next section. Numerical model definitions including estimation and the governing equations of them, a brief outline of the SWAN, MIKE SW, and WRF models, Setup, calibration, and Validation of models, and a definition of wave spectrum and its application are introduced in the section 3. The main wind and wave simulated parameters by models, the directional and frequency wave spectrum, and their comprehensive comparison are presented in section 4. Finally, the conclusions and recommendations are presented in section 5.

2. Study Area

The study area is located in the northern Gulf of Oman and southeast of Iran in the offshore area of Chabahar port (Figure 1). The Chabahar port is the only ocean port in Iran. This port is a gateway for Central Asian countries to expand their trade first with the Indian Ocean countries and then with the rest of the world. The Chabahar port lies at the mouth of the Chabahar Bay and is always exposed to high waves, resulting from cyclones and monsoons coming from the Indian Ocean. The area under investigation for wave characteristics analysis is located between latitudes 24°40' to 25°40' N, and longitudes 60° to 61° E.

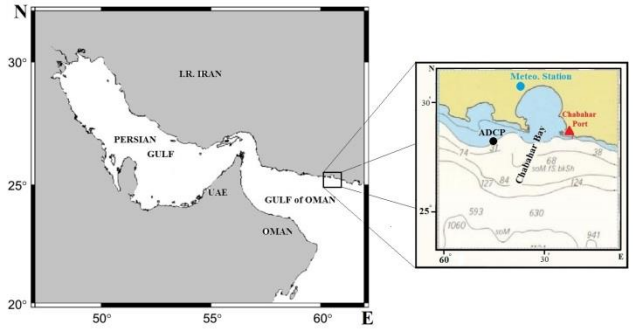

Figure 1. Area under investigation

3. Material and Methods

3.1 Numerical Models Definitions

The coupled atmosphere–wave modeling system includes WRF, SWAN, and the Model Coupling Toolkit [37] to exchange data fields between the wave and the atmosphere model. The Model Coupling Toolkit (MCT) allows the transformation of various distributed data between component models using a parallel coupled approach. MCT is a program written in Fortran90 and works with the MPI communication protocol. It is compiled as a set of libraries, which are linked during the compilation [6]. Fields exchanged in the coupled system are shown in Figure 2. The WRF model transfers wind speeds at 10 meters above the sea surface (U_{10}, V_{10}) to SWAN, and SWAN passes back significant wave height, wavelength, and wave period [26].

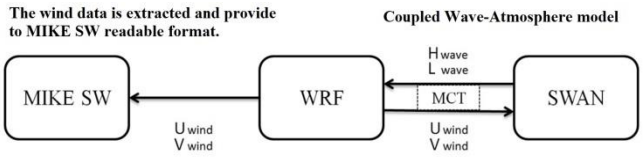

Figure 2. Data fields exchanged between models

3.2 WRF Model

The WRF is a non-hydrostatic, quasi-compressible atmospheric model with several boundary layer schemes, as well as both explicit and parameterized physics [13]. WRF is an advanced mesoscale numerical weather prediction system designed to serve both operational forecasting and atmospheric research needs [38]. The time integration scheme in the model uses the third-order Runge-Kutta scheme, and the spatial discretization employs second to sixth-order schemes [39]. The WRF model has two large classes of simulations that can produce both ideal and real data simulations. In the simulation with real data, a pre-processing system named WPS is required to generate all atmospheric fields and static geographical data for initial boundaries. The work of vertically interpolating meteorological fields to WRF eta levels is performed within the real program [22].

The WRF should be provided by physical schemes which are to be fitted with the season and the geographical area. Based on recent sensitive studies in low-level wind simulation, three important physical schemas of Land Surface Model (LSM), Surface Layer (SL), and planetary boundary Layer (PBL) have been introduced [40-43]. To modify the WRF code to provide an enhanced bottom roughness when computing the bottom stress over the ocean, Warner et al. [12] have recommended the use of Mellor-Yamada Nakanishi Niino (MYNN) scheme for PBL. This scheme solves higher-order Turbulent Kinetic Energy equations than the other schemes (e.g. MYJ scheme by Janjic [44], and YSU scheme by Hong et al. [45]). The equation of the MYNN PBL scheme is affected by the surface stress directly. In the MYNN scheme, the default surface roughness (z_0) method is as follows by Fairall et al. [46], in which the Charnock parameter (c_a) is a function of 10 m wind speed (U_{10}):

$$z_0 = \frac{c_a U_*^2}{g} + \frac{v}{U_*} \quad (1)$$

$$c_a = \begin{cases} 0.011, U_{10} \le 10 ms^{-1} \\ \frac{1}{8}(7U_{10} + 18) \times 10^{-3}, 10 ms^{-1} < U_{10} < 18 ms^{-1} \\ 0.018, U_{10} \ge 18 ms^{-1} \end{cases} \quad (2)$$

Here, u_* is the surface stress (friction velocity), g is gravity, and v is the viscosity. After the WRF code has been modified to allow the MYNN scheme to incorporate the effect of the waves according to the formula of Taylor and Yelland [47], the roughness length equation is as follows:

$$z_0 = 1200\, H_s \left(\frac{H_s}{L_p}\right)^{4.5} + 0.11 \frac{v}{U_*} \quad (3)$$

Here, H_s is the significant wave height, and L_p is the mean wavelength. This option is activated when coupling to the wave model and was chosen as a representative method [6, 48].

3.3 SWAN Model

The SWAN resolves the spectral balance equation in the Cartesian system or spherical coordinates as a function of action density spectrum N(x,t,σ,θ). SWAN can simulate shoaling due to spatial variations at the bottom. It can also simulate refraction, bottom friction, depth-induced wave breaking, and the three-wave interactions, which are very important factors for shallow waters [35]. SWAN solves the action balance equation as follows:

$$\frac{\partial \mathrm{N}}{\partial \mathrm{t}}+\frac{\partial \mathrm{c_x N}}{\partial \mathrm{x}}+\frac{\partial \mathrm{c_y N}}{\partial \mathrm{y}}+\frac{\partial \mathrm{c_\theta N}}{\partial \theta}+\frac{\partial \mathrm{c_\sigma N}}{\partial \sigma}=\frac{\mathrm{S}_{(\sigma,\theta)}}{\sigma} \quad (4)$$

Where N is the action density spectrum. The first term on the left-hand side represents the local rate of change of action density in time, the second and third terms represent the propagation of action density in geographic space, and the fourth term represents depth-induced and current-induced refraction. The fifth term represents the shifting of the relative frequency due to variations in depth and currents. The term $S(\sigma,\theta)$ is the source term in terms of energy density [49].

SWAN contains several physical processes that add or withdraw wave energy to or from the wave field. The processes included are wind input, white-capping, bottom friction, depth-induced wave breaking, obstacle transmission, nonlinear wave-wave interactions (quadruplets and triads), and wave-induced set-up [32].

One of the most important calibration factors in SWAN is the changing rate of energy dissipation by the white-capping. For this purpose, the quasi-linear model by Hasselmann [50], and Janssen [51] are considered. The white-capping formulation implemented in SWAN is:

$$\mathrm{S_{dis}}=-\mathrm{C_{ds}}\left[(1-\delta)+\delta\left(\frac{\mathrm{k}}{\bar{\mathrm{k}}}\right)\right]\frac{\mathrm{k}}{\bar{\mathrm{k}}}\left(\frac{\tilde{\mathrm{S}}}{\tilde{\mathrm{S}}_{\mathrm{PM}}}\right)^{\mathrm{q}}\tilde{\sigma}\,\mathrm{E}(\sigma,\theta \quad (5)$$

$$\begin{cases}\mathrm{C_{ds}}=2.36\times10^{-5},\delta=0.8 & \text{for Komen et al. [52]}\\ \mathrm{C_{ds}}=4.10\times10^{-5},\delta=0.5 & \text{for Janssen [51]}\end{cases} \quad (6)$$

Here, k is the wave number, $\tilde{k}$ mean spectral wave number and $\tilde{\sigma}$ are the mean spectral wave frequency. The quantity $\tilde{S}$ is the mean spectral steepness, and $\tilde{S}_{PM}=\sqrt{3.02\times10^{-3}}$ is the mean steepness of the Pierson-Moskowitz spectrum. Coefficient for determining the rate of white-capping dissipation (C_{ds}), and coefficient which determines the dependency of the white-capping on wave number (δ) are the tuning parameters in the equation [11].

The bottom friction in SWAN is a combination of the empirical model of JONSWAP [53], the drag law model of Collins [54], and the eddy-viscosity model of Madsen et al. [55]:

$$\mathrm{S_{ds,b}}=-\mathrm{C_b}\frac{\sigma^2}{\mathrm{g^2\sinh^2\kappa d}}\mathrm{E}(\sigma,\theta) \quad (7)$$

Here, C_b is a bottom friction coefficient [32].

3.4 MIKE SW Model

The MIKE SW simulates the growth, decay, and transformation of wind-generated waves and swells in offshore and coastal areas. The waves in this module are represented by the density spectrum $N(\sigma, \theta)$. The independent parameters are the relative angular frequency ($\sigma=2\pi f$), and the direction of wave propagation (θ). The governing equation is the wave action balance equation formulated in either Cartesian or spherical coordinates [56]:

$$\frac{\partial \mathrm{N}}{\partial \mathrm{t}}+\nabla.(\vec{\mathrm{v}}\,\mathrm{N})=\frac{\mathrm{s}}{\sigma}\rightarrow\frac{\partial}{\partial \mathrm{t}}\mathrm{N}+\frac{\partial}{\partial \mathrm{x}}\mathrm{C_x N}+\frac{\partial}{\partial \mathrm{y}}\mathrm{C_y N}+\frac{\partial}{\partial \sigma}\mathrm{C_\sigma N}+\frac{\partial}{\partial \theta}\mathrm{C_\theta N}=\frac{\mathrm{s}}{\sigma} \quad (8)$$

where N is wave action density, σ is the relative angular frequency, θ is the wave direction, C_x, C_y, C_σ, C_θ are celerity characteristics in a geographical and spectral coordinate system, and S is the energy source term, which represents the superposition of source function describing various physical phenomenon .

$$\mathrm{S}=\mathrm{S_{in}}+\mathrm{S_{nl}}+\mathrm{S_{ds}}+\mathrm{S_{bot}}+\mathrm{S_{surf}} \quad (9)$$

Where S_{in} represents the generated energy by the wind, S_{nl} is the wave energy transfer due to non-linear wave-wave interaction, S_{ds} is the dissipation of wave energy due to white capping, S_{bot} is the dissipation due to bottom friction and S_{surf} is the dissipation of wave energy due to depth-induced breaking [57-58].

The two main factors for model calibration in MIKE SW are white-capping and bottom friction. The white-capping is provided by Janssen [51] in terms of wave number:

$$\mathrm{S_{ds}}(\mathrm{f},\theta)=-\mathrm{C_{ds}^*}\left[\frac{\bar{\alpha}}{\bar{\alpha}_{\mathrm{PM}}}\right]^{\mathrm{m}}\left\{(1-\delta)\frac{\mathrm{k}}{\bar{\mathrm{k}}}+\delta\left(\frac{\mathrm{k}}{\bar{\mathrm{k}}}\right)^2\right\}\bar{\sigma}\mathrm{E}(\mathrm{f},\theta) \quad (10)$$

Here, $\bar{\alpha}$ is the overall steepness of the wave field, $\bar{\alpha}_{PM}$ is the value of $\bar{\alpha}$ for the Pierson-Moskowitz spectrum, $\bar{\mathrm{k}}$ is the mean wave number, and $\bar{\sigma}$ is the mean relative angular frequency. C_{ds}, δ, and m are constant and the default values for them are 4.5, 0.5 and 4 respectively [23]. The rate of dissipation due to bottom friction by Komen et al. [52] is:

$$\mathrm{S_{bot}}(\mathrm{f},\theta)=-\left(\mathrm{C_f}+\frac{\mathrm{f_c}(\bar{\mathrm{u}},\bar{\mathrm{k}})}{\mathrm{k}}\right)\frac{\mathrm{k}}{\sinh 2\mathrm{kd}}\mathrm{E}(\mathrm{f},\theta) \quad (11)$$

Here, C_f is a friction coefficient with a typical value between 0.001 to 0.01 m/s depending on the bed and flow conditions. The default value for C_f is 0.0077 m/s. the k is the wave number, d is water depth, f_c is the friction coefficient for current with zero as the default value corresponding to excluding the effect of the current on the bottom friction, and u is the current velocity [23].

3.5 Models Setup and Validation

Initially, to make the results of the simulations closer to the real data, the models must be validated. The validation period is considered from July 3 to 6, 2016.

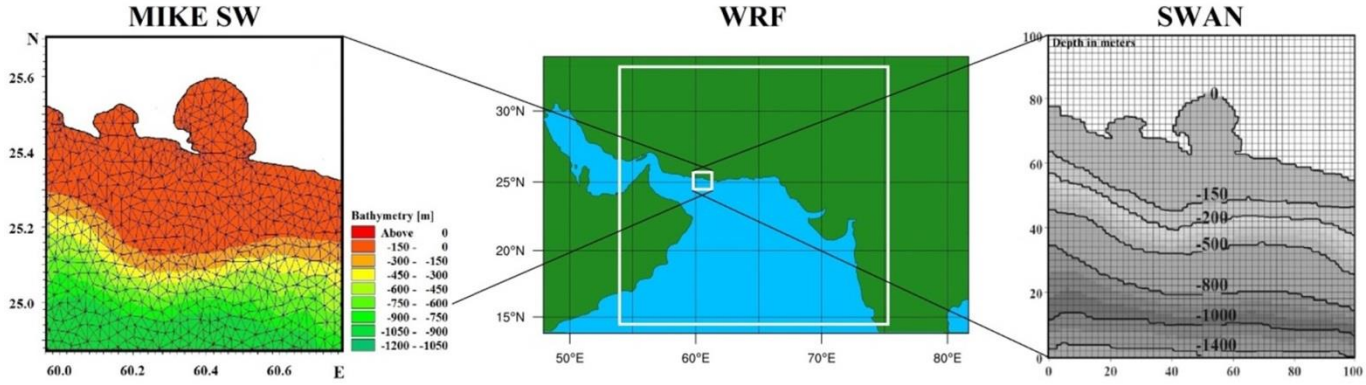

Figure 3. Telescopic domains configuration of WRF and wave models (MIKE SW & SWAN) domains.

The recorded wind data at Chabahar meteorological station with 3 hours time interval at 25°26' N and 60°22' E, prepared by Iran Meteorological Organization, and the recorded wave data by ADCP (Acoustic Doppler Current Profilers) with one hours time interval at 25°13' N and 60°16' E, prepared by Iranian Port and Maritime Organization, which located in 24 km southeast of the mouth of Chabahar Bay, were used to calibrate and validate the models.

The best configuration for the atmospheric model (WRF) was selected based on previous studies [40-42, 59-60]. Two telescopic domains were designated. The external domain (Nx × Ny: 80×80) with 27 km resolution, and the internal domain (Nx × Ny: 13×13) with 9 km resolution covers the Chabahar Bay and offshore area, which exactly matches the domain of wave models (Figure 3).

The microphysics options applied in this study include the WRF Single-Moment 6-class scheme by Hong et al. [61], long wave radiation (RRTM) by Mlawer [62], and short wave radiation by Dudhia [63], the MYNN planetary boundary layer (PBL) scheme by Nakanishi and Niino [64], and the Noah Land Surface Model (LSM) by Chen and Dudhia [65]. Initial and boundary conditions for WRF are prepared by FNL data type. The NCEP FNL (Final) Operational Global Analysis data are on a 1° by 1° grid prepared operationally every six hours. This product is received from the Global Data Assimilation System (GDAS), which continuously collects observational data from the Global Telecommunications System (GTS), and other sources, for many analyses. The analyses are available on the surface, at 26 levels from 1000 to 10 mb, in the surface boundary layer and at some sigma layers, the tropopause, and a few others.

The computational grid for SWAN was prepared as a regular mesh with several 100×100 grids was considered. The length and width of each cell are about 1.8 km. The SWAN model origin of the grid is at 24° 50' N and 60° 0.0' E, and the resolution in the geographical space is 0.016 × 0.016 degrees (Figure 3). The mode of implementation is two-dimensional and non-stationary, the spectral resolution varying from 0.042 Hz to 0.65 Hz with a $\sigma m+1=1.1\sigma m$ distribution, the number of frequencies in the spectral space is 24, and the number of directions in the spectral space is 36, and the coordinates is spherical.

For calibration of the SWAN model, the white-capping was considered. For the rate of energy dissipation by white-capping (C_{ds}), at first, the model default value (2.36×10^{-5}) was considered. The calculation was done in a non-stationary method with a time step of 30 minutes. The results show that the observational wave height data were above the simulated wave height. By decreasing the value of the white-capping, finally, the best agreement was obtained with the value of 1.00×10^{-6}. For energy dissipation due to depth breaking, the value of the energy dissipation coefficient and the ratio of maximum wave height on depth were considered 0.8 and 0.01, respectively.

The coupled wave-atmosphere model was executed with SWAN and WRF. The time step of WRF and SWAN is adjusted equal to 180 seconds and 30 minutes increment, respectively. The two models were synchronized 1800 seconds to exchange data fields through the MCT coupler during the simulation. Figure 4 represents the synoptic pattern of the area with maximum wind speed and wind field at 10 m level, and the pattern of sea level pressure distribution over the area. Figure 5 shows the time series of wind and wave parameters simulated by COAWST in comparison with observational data.

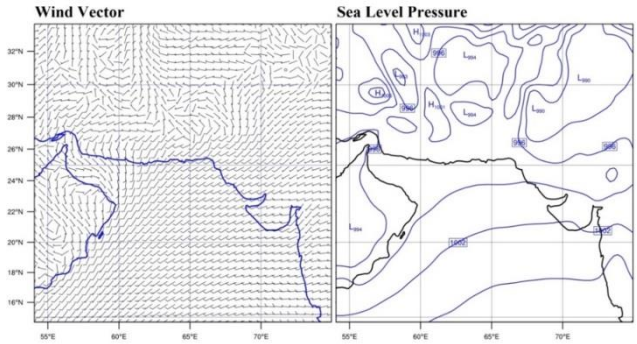

Figure 4. Synoptic pattern of 10 m wind field (left) and sea level pressure distribution (right) at annual maximum wind speed (2016 July 05, 12:00).

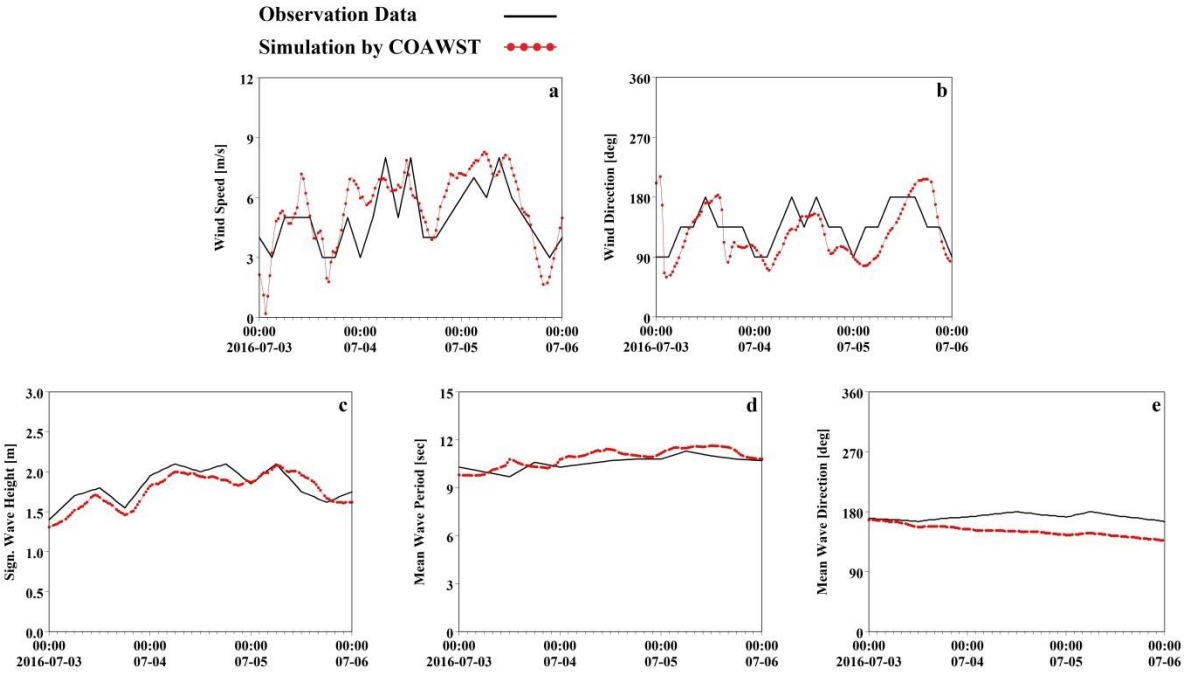

Figure 5. Time series of (a) wind speed, (b) wind direction, (c) Sign. Wave Height, (d) Mean wave Period and (e) Mean Wave Direction derived from COAWST in comparison with observational data during the validation period.

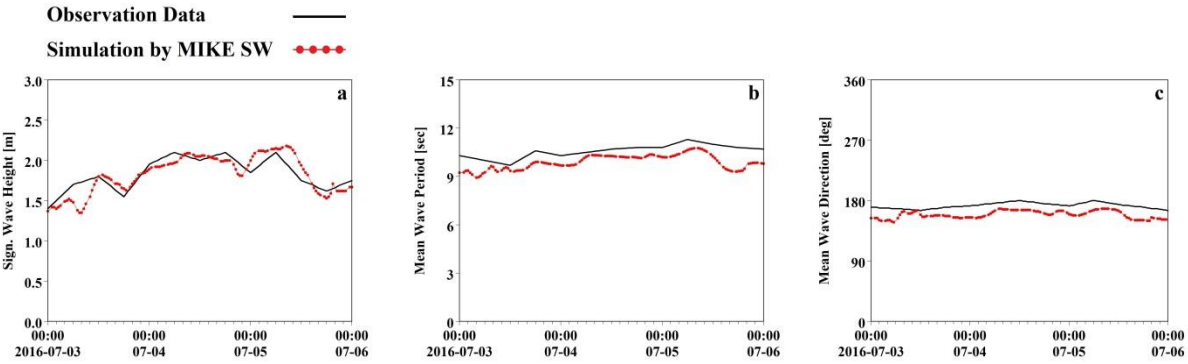

Figure 6. Time series of (a) Sign. Wave Height, (b) Mean wave Period, and (c) Mean Wave Direction derived from MIKE-SW in comparison with observational data during the validation period

The MIKE SW has been adapted to simulate the wave parameters in the validation period (July 3 to 6, 2016). The flexible mesh has been adapted for the domain of simulation. This mesh has been generated with the 3663 cells (Figure 3). The hourly wind speed and direction adapted to the MIKE SW model were derived from the WRF simulations. After the WRF is implemented in the coupled system, the wind data is extracted and provided to MIKE SW in a readable format. The modeled area is bordered by three open boundaries at the west, east, and south, and one land boundary at the north. For the open boundary conditions, the water level elevation was considered at all three open boundaries. Considering the geographical location of the area, and taking into account the selected period for simulation, the water temperature was set to 25°, and the water salinity was set to 35 ppt. Figure 6 shows time series of wave parameters simulated by MIKE SW in comparison with observational data.

For accuracy evaluation of the simulation results, the Bias parameter, Correlation Coefficient (CC), Root Mean Square Error (RMSE), and Scattering Index (SI) were considered [66] and represents in Table 1.

$$\text{Bias} = \sum_{i=1}^{N} \frac{1}{N} (y_i - x_i) \quad (12)$$

$$\text{CC} = \sum(x_i - \bar{x})(y_i - \bar{y}) / \sqrt{\sum(x_i - \bar{x})^2 \sum(y_i - \bar{y})^2} \quad (13)$$

$$\text{RMSE} = \sqrt{1/N \sum_{i=1}^{N} (y_i - x_i)^2} \quad (14)$$

$$\text{SI} = \sqrt{\frac{1}{N}\sum_{i=1}^{N} (y_i - x_i)^2} \Big/ \frac{1}{N}\sum_{i=1}^{N} x_i \quad (15)$$

Table 1. Performance evaluation of wave parameters base on computational errors during validation period.

MODEL	Parameters	Bias	CC	RMSE	SI
COAWST	Wind Sp.	0.47	0.78	1.24	0.24
	Wind Dir.	-1.28	0.52	6.50	0.26
	Wave Height	0.13	0.74	0.19	0.10
	Wave Period	-1.01	0.90	1.08	0.10
	Wave Dir.	-4.87	0.91	8.25	0.16
MIKE SW	Wave Height	0.19	0.73	0.32	0.17
	Wave Period	-1.98	0.45	3.20	0.30
	Wave Dir.	-7.60	0.41	8.69	0.16

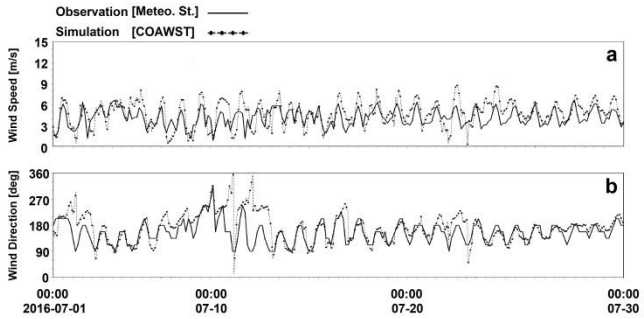

Figure 7. (a) Wind speed, and (b) wind direction simulated by COAWST (by WRF) in comparison with observational data

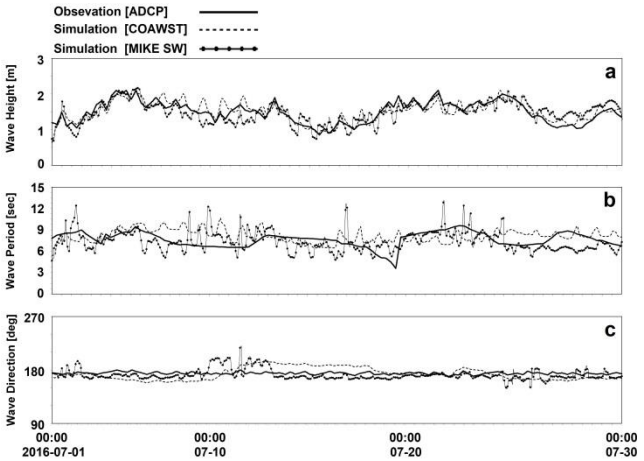

Figure 8. Time series of (a) Sign. Wave Height, (b) Mean wave Period, and (c) Mean Wave Direction derived from COAWST and MIKE SW in comparison with observational data

Table 2. Computational errors for simulated parameters in comparison with observational data in July, 2016.

MODEL	Parameters	Bias	CC	RMSE	SI
COAWST	Wave Height	0.22	0.90	0.15	0.10
	Wave Period	0.46	0.61	0.98	0.10
	Wave Dir.	7.50	0.66	2.97	0.12
MIKE SW	Wave Height	0.24	0.83	0.20	0.13
	Wave Period	0.66	0.78	3.11	0.31
	Wave Dir.	12.76	0.49	9.68	0.12

4. Results and Discussions

Figures 7 and 8 represent the time series data derived from the model results at the monitoring point. Figure 7 contains wind speed and direction for the July of 2016, during the summer monsoon of the Indian Ocean. Since Chabahar offshore is further away from the monsoon area, the intensity of the wind seems justified. The maximum wind speed reached up 10 m/s at its maximum and the wind direction was mainly from the south.

Figure 8a shows the significant wave height and contain two points. First, there is high coordination between the model's results and the observational data. Second, based on past experiences and due to the intensity of the wind, the significant wave height is higher than expected, and as a result, indicating the effect of swell waves. According to the diagrams, the height of the wave in July is between 0.85 m to 2 m and the average is 1.5 m.

Figure 8b shows the mean wave period, which shows that the results of the models are not desirable, compared to the observed data but are acceptable. Figure 8c shows the mean wave direction results by models compared with the real data that are in good agreement with the wind direction. The wave direction is mainly from the south. Table 2 represents the computational errors for simulated parameters by models compared with real data in July, 2016.

The scatter plots are presented in Figure 9. By analyzing Figures 8 and 9 and Table 2, it can be concluded that the results of the simulations by both models are accurate and acceptable, but the results of the COAWST model are in better agreement with the real data than the results of MIKE SW model.

To calculate and plot the wave spectrum, a time interval on July 3 to 7, 2016 was considered. This time interval included maximum wind speed during July 2016. For this purpose, significant wave height, frequency, peak angular frequency, peak wave period, and maximum wave height are needed (Table 3). The Wave spectrums were prepared for COAWST, MIKE SW, and ADCP data. The smoothing Spline technique from MatLab software was used. To distinguish which of the presumed wave spectrums could better represent the pattern of waves in the Chabahar offshore area, the JONSWAP spectrum, Bretschneider spectrum, and Ochi spectrum were considered.

According to Figure 10, the best-fitted pattern for the concerning point is represented by the JONSWAP spectrum. The frequency spectrum of waves shows a single peak type spectrum, which suggests that just one main frequency (period) is responsible for the generated waves. The peak value of observational (ADCP) data is located at 4.56 m^2s in frequency of 0.09 Hz, while by MIKE SW this value is 4.65 m^2s in frequency of 0.12 Hz, and by COAWST is 4.55 m^2s in frequency of 0.08 Hz. According to the results, the peaks of the wave spectrums diagrams are almost on the same level. Also, the smoothed and unsmoothed spectrum of the COAWST model has a better agreement with the spectrum of observational data.

Figure 11 shows the directional wave spectrum by ADCP, MIKE SW, and COAWST. According to diagrams, the direction of wave propagation has oriented from south and southeast and is affected by wind direction. The MIKE SW wave propagation was located closer to ADCP wave propagation than COAWST.

Table 3. Wave parameters at maximum wind speed during July, 2016.

Date & Time	Observation or Model	Tp (sec)	Fp (Hz)	WD (deg)	Hmax (m)	Hs (m)	Max. of Spectrums (m^2.s)			
							S(f)	JONSWAP	Ochi	Bretschneider
2016-07-05 06:00	ADCP	11.1	0.09	180	2.10	1.55	4.56	4.89	2.38	2.01
	MIKE SW	8.33	0.12	165	2.18	1.75	4.65	4.66	2.79	2.09
	COAWST	12.5	0.08	149	2.08	1.50	4.55	4.70	2.33	1.69

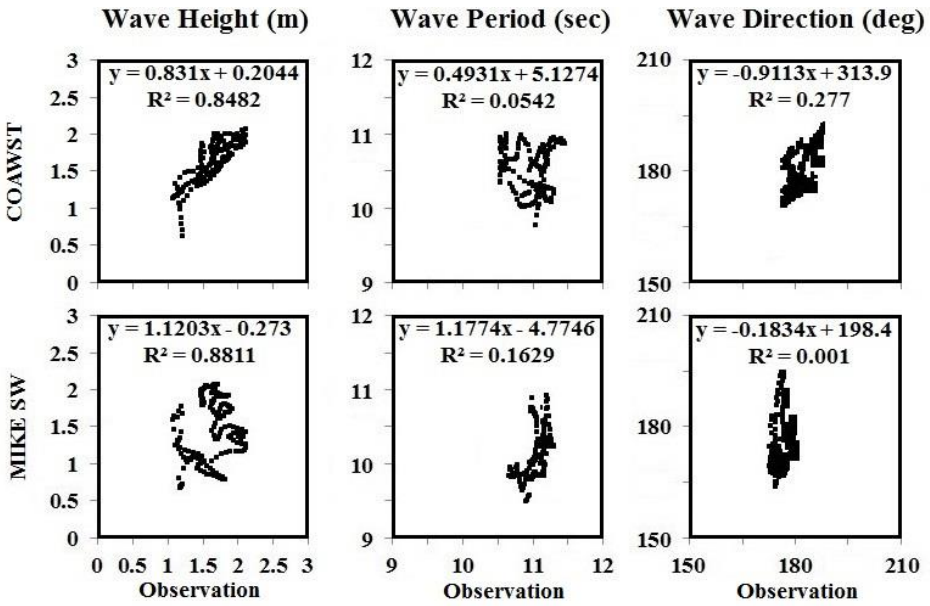

Figure 9. Scatter plot diagram for wave height, wave period, and wave direction.

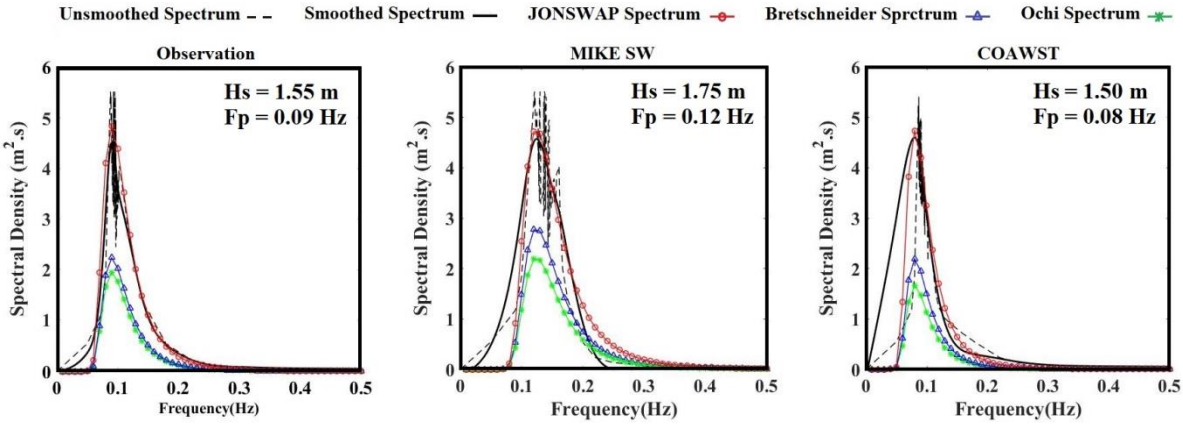

Figure 10. Frequency wave spectrums for Observation (left), MIKE SW (mid), and COAWST (right) simulations results for period of maximum wind speed in July, 2016.

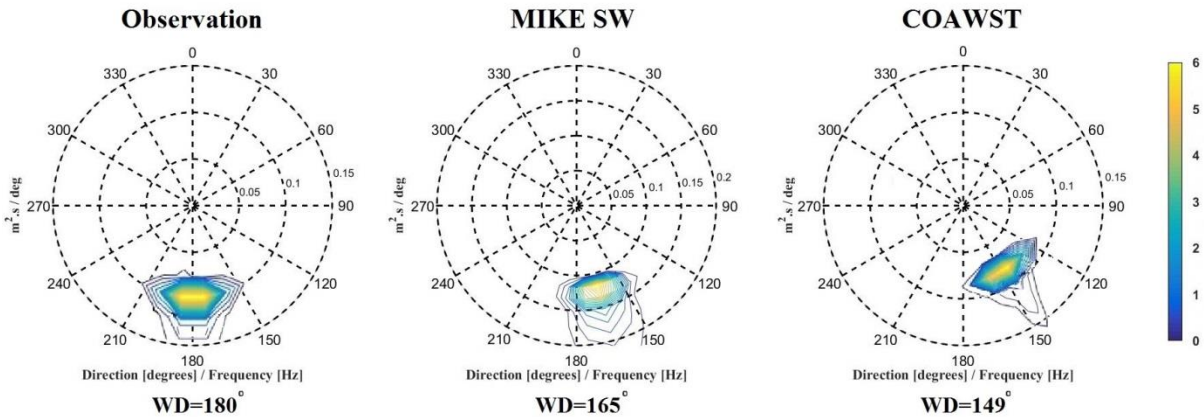

Figure 11. Directional wave spectrums for ADCP (left), MIKE SW (mid), and COAWST (right) simulations results for the period of maximum wind speed in July 2016.

5. Conclusion

In this study, a comparison between SWAN and MIKE SW wave models for the wave field in the Chabahar offshore area in the northern Gulf of Oman was implemented during the peak activity of the Indian Ocean Summer Monsoon occurs in July 2016. Wind conditions for the wave models were obtained by the WRF model in two ways. First, WRF and SWAN were implemented as wave-atmosphere subsystems of the COAWST (Coupled Ocean–Atmosphere–Wave–Sediment Transport) model. Second, the wind field of the WRF model output was extracted and converted to the MIKE SW readable format.

Simulated wind parameters including speed and direction are compared with observational data from the Chabahar meteorology station. The result of the wind simulation was acceptable by COAWST and was found closer to the observational data according to the computational errors. The results of the wave simulation are acceptable by both the COAWST and MIKE SW experiments in comparison with observational data of ADCP (Acoustic Doppler Current Profilers), but the results of the COAWST were found closer to the observational data. The results of the COAWST model were more accurate than the results of MIKE SW in simulating wave height and period, while in simulating wave direction, MIKE SW was more accurate than COAWST.

The wave spectrums were prepared for observational data and models results during the interval of maximum wind speed in July 2016. All Spectrums had a single peak which means that one main frequency is responsible for the most wave energy. Provided spectrums were compared with standard spectrums of JONSWAP, Bretschneider, and Ochi. The best-fitted spectrum was JONSWAP for all occasions. This means that the sea state of the Chabahar offshore area was not a fully developed sea during the simulation period. The peak of the frequency spectrum diagram for the COAWST model is closer to the frequency spectrum of observational data than to the MIKE SW.

Directional wave spectrums of observational data and models results showed the south and southeast directions for the wave energy propagation. The direction of wave propagation is affected by wind direction. The MIKE SW wave propagation was found closer to observational wave data propagation than COAWST.

As a general conclusion, it can be stated that both models have provided acceptable results. It might be expected that the results of the COAWST model match the observational data to a higher degree than the results of the MIKE SW model, but in practice, this is not the case. The complexity of a set is not always the reason for its better results. Although MIKE SW model is a complete but simple set, it provides acceptable results compared to the complex COAWST set, which is the result of the efforts of J.C. Warner and his colleagues. Perhaps the difference in the views of physical oceanographers in the Netherlands and Denmark in the DELFT and DHI collections for the production of SWAN and MIKE models, respectively, according to the results of this research, will finally end in the same conclusion.

Of course, the extent of the simulation area and wind field condition induced by monsoons or cyclones can also be decisive in the obtained results. One should wait for another research with the same conditions but with a larger simulation scope in other ocean locations, and with different wind fields !

Acknowledgment

The authors are thankful to Iranian Meteorological Organization and Iranian Port and Maritime Organization for providing observational data.

6. References

[1] Shankar, D., Vinayachandran, P.N. and Unnikrishnan, A.S, (2002). *The monsoon currents in the north Indian Ocean. Progress in oceanography,* 52(1), p.63-120.

[2] Zheng, C., Pan, J., Tan, Y., Gao, Z., Rui, Z. and Chen, C., (2015). *The seasonal variations in the significant wave height and sea surface wind speed of the China's seas. Acta Oceanologica Sinica,* 34, p.58-64.

[3] Allahdadi, M.N., Chaichitehrani, N., Allahyar, M. and McGee, L., (2017). *Wave spectral patterns during a historical cyclone: a numerical model for cyclone Gonu in the northern Oman Sea. Open Journal of Fluid Dynamics,* 7(2). P.131-151.

[4] Zhou, L.M., Wang, A.F. and Guo, P.F., (2008). *Numerical simulation of sea surface directional wave spectra under typhoon wind forcing. Journal of Hydrodynamics, Ser. B,* 20(6), p.776-783.

[5] Kutupoğlu, V., Çakmak, R.E., Akpınar, A. and van Vledder, G.P., (2018). *Setup and evaluation of a SWAN wind wave model for the Sea of Marmara. Ocean Engineering,* 165, p.450-464.

[6] Warner, J.C., Armstrong, B., He, R. and Zambon, J.B., (2010). *Development of a coupled ocean–atmosphere wave sediment transport (COAWST) modeling system. Ocean modeling,* 35(3), p.230-244.

[7] Moeini, M.H. and Etemad-Shahidi, A., (2007). *Application of two numerical models for wave hindcasting in Lake Erie. Applied Ocean Research,* 29(3), p.137-145.

[8] Xu, F., Cheng, Z. and Xia, M., (2020). *Surface wave field under binary typhoons Sarika and Haima (2016) in South China Sea. Estuarine, Coastal and Shelf Science,* 241, p.106802.

[9] Abdollahzadehmoradi, Y., Erdik, T., Özger, M. and Altunkaynak, A., (2014). *October. Application of MIKE 21 SW for wave hindcasting in Marmara Sea Basin for the year 2012. In 11th international congress on advances in civil engineering (ACE)*, p.21-25.

[10] Ardhuin, F., Bertotti, L., Bidlot, J.R., Cavaleri, L., Filipetto, V., Lefevre, J.M. and Wittmann, P., (2007). *Comparison of wind and wave measurements and models in the Western Mediterranean Sea. Ocean Engineering*, 34(3-4), p.526-541.

[11] Rusu, L., Bernardino, M. and Guedes Soares, C., (2014). *Wind and wave modelling in the Black Sea. Journal of Operational Oceanography*, 7(1), p.5-20.

[12] Warner, J.C., Sherwood, C.R., Signell, R.P., Harris, C.K. and Arango, H.G., (2008). *Development of a three-dimensional, regional, coupled wave, current, and sediment-transport model. Computers & geosciences*, 34(10), p.1284-1306.

[13] Zambon, J.B., He, R. and Warner, J.C., (2014). *Investigation of hurricane Ivan using the coupled ocean atmosphere wave sediment transport (COAWST) model. Ocean Dynamics*, 64, p.535-1554.

[14] Anton, I.A., Rusu, L. and Anton, C., (2019). *Nearshore wave dynamics at Mangalia beach simulated by spectral models. Journal of Marine Science and Engineering*, 7(7), p.206.

[15] Liang, B., Gao, H. and Shao, Z., (2019). *Characteristics of global waves based on the third-generation wave model SWAN. Marine Structures*, 64, p.35-53.

[16] Pradhan, U.K., Mishra, P., Mohanty, P.K., Panda, U.S. and Ramanamurthy, M.V., (202). *Modeling of tidal circulation and sediment transport near tropical estuary, east coast of India. Regional Studies in Marine Science*, 37, p.101351.

[17] Son, B. and Do, K., (2021). *Optimization of SWAN wave model to improve the accuracy of winter storm wave prediction in the East Sea. Journal of Ocean Engineering and Technology*, 35(4), p.273-286.

[18] Islek, F. and Yuksel, Y., (2021). *Inter-comparison of long-term wave power potential in the Black Sea based on the SWAN wave model forced with two different wind fields. Dynamics of Atmospheres and Oceans*, 93, p.101192.

[19] Li, Z., Tam, C.Y., Li, Y., Lau, N.C., Chen, J., Chan, S.T., Dickson Lau, D.S. and Huang, Y., (2022). *How Does Air-Sea Wave Interaction Affect Tropical Cyclone Intensity? An Atmosphere-Wave-Ocean Coupled Model Study Based on Super Typhoon Mangkhut (2018). Earth and Space Science*, 9(3), p.e2021EA002136.

[20] Zed, A.A.A., Kansoh, R.M., Iskander, M.M. and Elkholy, M., (2022). *Wind and wave climate southeastern of the Mediterranean Sea based on a high-resolution SWAN model. Dynamics of Atmospheres and Oceans*, 99, p.101311.

[21] Booij, N.R.R.C., Ris, R.C. and Holthuijsen, L.H., (1999). *A third-generation wave model for coastal regions: 1. Model description and validation. Journal of geophysical research: Oceans*, 104(C4), p.7649-7666.

[22] Skamarock, W.C., Klemp, J.B. and Dudhia, J., (2005). *Coauthors, 2008: A description of the Advanced Research WRF version 3. NCAR Tech*, Note TN-4751STR.

[23] DHI (Danish Hydraulic Institute)., (2012). *MIKE 21 Spectral Wave Module. Scientific Documentation. Danish Hydraulic Institute*, p.66.

[24] Warner, J.C., Perlin, N. and Skyllingstad, E.D., (2008). *Using the Model Coupling Toolkit to couple earth system models. Environmental modelling & software*, 23(10-11), p.1240-1249.

[25] Ninomiya, J., Mori, N., Yasuda, T., Mase, H. and Kihara, N., (2012). *Improvement of Storm Surge Simulation Upon Parameterizations Of Coupled Air-Sea Interactions. Coastal Engineering Proceedings*, (33), p.51-51.

[26] Du, J., Larsén, X.G. and Bolaños, R., (2015). *A coupled atmospheric and wave modeling system for storm simulations. In Proceedings of EWEA Offshore 2015 conference European Wind Energy Association (EWEA).*

[27] Grifoll, M., Navarro, J., Pallares, E., Ràfols, L., Espino, M. and Palomares, A., (2016). *Ocean–atmosphere–wave characterisation of a wind jet (Ebro shelf, NW Mediterranean Sea). Nonlinear Processes in Geophysics*, 23(3), p.143-158.

[28] Ricchi, A., Miglietta, M.M., Falco, P.P., Benetazzo, A., Bonaldo, D., Bergamasco, A., Sclavo, M. and Carniel, S., (2016). *On the use of a coupled ocean–atmosphere–wave model during an extreme cold air outbreak over the Adriatic Sea. Atmospheric Research*, 172, p.48-65.

[29] Hoque, M.A., Perrie, W. and Solomon, S.M., (2020). *Application of SWAN model for storm generated wave simulation in the Canadian Beaufort Sea. Journal of Ocean Engineering and Science*, 5(1), p.19-34.

[30] Rusu, E. and Raileanu, A., (2016). *A multi-parameter data-assimilation approach for wave prediction in coastal areas. Journal of Operational Oceanography*, 9(1), p.13-25.

[31] Remya, P.G., Kumar, R. and Basu, S., (2014). *An assessment of wind forcing impact on a spectral wave model for the Indian Ocean. Journal of Earth System Science*, 123, p.1075-1087.

[32] SWAN team., (2018). *SWAN Scientific and Technical Documentation; Delft University of Technology: Delft, The Netherlands*, p.147.

[33] Ilia, A. and O'Donnell, J., (2018). *An assessment of two models of wave propagation in an estuary protected by breakwaters. Journal of Marine Science and Engineering*, 6(4), p.145.

[34] Strauss, D., Mirferendesk, H. and Tomlinson, R., (2007). *Comparison of two wave models for Gold Coast, Australia. Journal of Coastal Research*, p.312-316.

[35] Montoya, R.D., Arias, A.O., Royero, J.O. and Ocampo-Torres, F.J., (2013). *A wave parameters and directional spectrum analysis for extreme winds. Ocean Engineering*, 67, p.100-118.

[36] Fonseca, R.B., Gonçalves, M. and Guedes Soares, C., (2017). *Comparing the performance of spectral wave models for coastal areas. Journal of Coastal Research*, 33(2), p.331-346.

[37] Jacob, R., Larson, J. and Ong, E., (2005). *M× N communication and parallel interpolation in Community Climate System Model Version 3 using the model coupling toolkit. The International Journal of High Performance Computing Applications*, 19(3), p.293-307.

[38] Chotamonsak, C., Salathé Jr, E.P., Kreasuwan, J., Chantara, S. and Siriwitayakorn, K., (2011). *Projected climate change over Southeast Asia simulated using a WRF regional climate model. Atmospheric Science Letters*, 12(2), p.213-219.

[39] Soda, T., Shiotani, S., Makino, H. and Shimada, Y., (2017). *19. Research on Ship Navigation in Numerical Simulation of Weather and Ocean in a Bay. Navigational Systems and Simulators: Marine Navigation and Safety of Sea Transportation*, p.141.

[40] Osuri, K.K., Mohanty, U.C., Routray, A., Kulkarni, M.A. and Mohapatra, M., (2012). *Customization of WRF-ARW model with physical parameterization schemes for the simulation of tropical cyclones over North Indian Ocean. Natural Hazards*, 63, p.1337-1359.

[41] Srinivas, C.V., Hariprasad, D., Bhaskar Rao, D.V., Anjaneyulu, Y., Baskaran, R. and Venkatraman, B., (2013). *Simulation of the Indian summer monsoon regional climate using advanced research WRF model. International Journal of Climatology*, 33(5), p.1195-1210.

[42] Samala, B.K., Baerjee, S., Kaginalkar, A. and Dalvi, M., (2013). *Study of the Indian summer monsoon using WRF–ROMS regional coupled model simulations. Atmospheric Science Letters*, 14(1), p.20-27.

[43] Andraju, P., Kanth, A.L., Kumari, K.V. and Vijaya Bhaskara Rao, S., (2019). *Performance optimization of operational WRF model configured for Indian Monsoon Region. Earth Systems and Environment*, 3, p.231-239.

[44] Janjić, Z.I., (1994). *The step-mountain eta coordinate model: Further developments of the convection, viscous sublayer, and turbulence closure schemes. Monthly weather review*, 122(5), p.927-945.

[45] Hong, S.Y., Noh, Y. and Dudhia, J., (2006). *A new vertical diffusion package with an explicit treatment of entrainment processes. Monthly weather review*, 134(9), p.2318-2341.

[46] Fairall, C.W., Bradley, E.F., Hare, J.E., Grachev, A.A. and Edson, J.B., (2003). *Bulk parameterization of air–sea fluxes: Updates and verification for the COARE algorithm. Journal of climate*, 16(4), p.571-591.

[47] Taylor, P.K. and Yelland, M.J., (2001). *The dependence of sea surface roughness on the height and steepness of the waves. Journal of physical oceanography*, 31(2), p.572-590.

[48] Du, J., (2017). *Coupling atmospheric and ocean wave models for storm simulation.*

[49] Holthuijsen, L.H., (2010). *Waves in oceanic and coastal waters. Cambridge university press.*

[50] Hasselmann, K., (1974). *On the spectral dissipation of ocean waves due to white capping. Boundary-Layer Meteorology*, 6, p.107-127.

[51] Janssen, P.A., (1991). *Quasi-linear theory of wind-wave generation applied to wave forecasting. Journal of physical oceanography*, 21(11), p.1631-1642.

[52] Komen, G.J., Hasselmann, S. and Hasselmann, K., (1984). *On the existence of a fully developed wind-sea spectrum. Journal of physical oceanography*, 14(8), p.1271-1285.

[53] Hasselmann, K., Barnett, T.P., Bouws, E., Carlson, H., Cartwright, D.E., Enke, K., Ewing, J.A., Gienapp, A., Hasselmann, D.E., Kruseman, P. and Meerburg, A., (1973). *Measurements of wind-wave growth and swell decay during the Joint North Sea Wave Project (JONSWAP). Ergaenzungsheft zur Deutschen Hydrographischen Zeitschrift, Reihe A*.

[54] Collins, J.I., (1972). *Prediction of shallow-water spectra. Journal of Geophysical Research*, 77(15), p.2693-2707.

[55] Madsen, O.S., Poon, Y.K. and Graber, H.C., (1988). *Spectral wave attenuation by bottom friction: Theory. In Coastal engineering*, 1988, p.492-504.

[56] Komen, G.J., Cavaleri, L., Donelan, M., Hasselmann, K., Hasselmann, S. and Janssen, P.A.E.M. (1996). *Dynamics and modelling of ocean waves*, p. 554.

[57] Remya, P.G., Kumar, R., Basu, S. and Sarkar, A., (2012). *Wave hindcast experiments in the Indian Ocean using MIKE 21 SW model. Journal of earth system science*, 121, p.385-392.

[58] Sørensen, O.R., Kofoed-Hansen, H., Rugbjerg, M. and Sørensen, L.S., (2005). *A third-generation spectral wave model using an unstructured finite volume technique. In Coastal Engineering 2004: (In 4 Volumes)*, p.894-906.

[59] Soltanpour, M., Ranji, Z., Shibayama, T., Ghader, S. and Nishizaki, S., (2018). *Numerical simulation of tropical cyclones and storm surges in the Arabian Sea. Coastal Engineering Proceedings, (36),* p.1-11.

[60] Pakhirehzan, M., (2021). *Analysis of Ashobaa tropical cyclone-induced waves in the Northern Indian Ocean using coupled atmosphere–wave modeling. Marine Systems & Ocean Technology,* 16, p.124-141.

[61] Hong, S.Y., Dudhia, J. and Chen, S.H., (2004). *A revised approach to ice microphysical processes for the bulk parameterization of clouds and precipitation. Monthly weather review,* 132(1), p.103-120.

[62] Mlawer, E.J., Taubman, S.J., Brown, P.D., Iacono, M.J. and Clough, S.A., (1997). *Radiative transfer for inhomogeneous atmospheres: RRTM, a validated correlated-k model for the longwave. Journal of Geophysical Research: Atmospheres,* 102(D14), p.16663-16682.

[63] Dudhia, J., (1989). *Numerical study of convection observed during the winter monsoon experiment using a mesoscale two-dimensional model. Journal of Atmospheric Sciences,* 46(20), p.3077-3107.

[64] Nakanishi, M. and Niino, H., (2006). *An improved Mellor–Yamada level-3 model: Its numerical stability and application to a regional prediction of advection fog. Boundary-Layer Meteorology,* 119, p.397-407.

[65] Chen, F. and Dudhia, J., (2001). *Coupling an advanced land surface–hydrology model with the Penn State–NCAR MM5 modeling system. Part I: Model implementation and sensitivity. Monthly weather review,* 129(4), p.569-585.

[66] Pakhirehzan, M., Rahbani, M. and Malakooti, H., (2018). *Numerical Study of Winter Shamal Wind Forcing on the Surface Current and Wave Field in Bushehr's Offshore Using MIKE21. International Journal Of Coastal, Offshore And Environmental Engineering (ijcoe),* 3(2), p.57-65.

INTERNATIONAL JOURNAL OF
COASTAL, OFFSHORE & ENVIRONMENTAL ENGINEERING IJCOE Vol.9 /No.1 / winter 2024(43-54)

Available online at: www. Ijcoe.org Manuscript Type: Original Research Article

An Approximate Simple Computational Method to Determine Hydrodynamic Forces on Drag Dominated Offshore Structures

Mohammad Reza Tabeshpour[1*], Hasan Imani[2]

[1*]*Associate Professor, Department of Mechanical Engineering, Sharif University of Technology, Tehran, Iran; tabeshpour@sharif.edu*
[2]*Ph.D., Department of Mechanical Engineering, Sharif University of Technology, Tehran, Iran.*

ARTICLE INFO

Article History:
Received: 04 Oct. 2023
Accepted: 05 Jan. 2024

Keywords:
Offshore structures
Initial design
Wave-induced drag loads
Wave penetration depth
Linearization of Morison's equation

ABSTRACT

Offshore structures are subjected to highly dynamic, irregular external loads from the air, water and soil. One of the most important forces affecting design, construction, installation, and maintenance of such structures considerably is wave force. Accordingly, accurate calculation of the wave force acting on offshore structures is one of the first steps of design process to ensure structural safety of all components under different environmental conditions. Nevertheless, such calculations are not only difficult but also computationally expensive. The main reasons for such complexities are the probabilistic and randomness of sea waves as well as the dynamics of Fluid Structure Interaction (FSI) which make the assessment of wave loading on offshore structures a challenging procedure in offshore engineering practice. It is therefore the main objective of this research to present effective alternative approximation methods based on the Morison's equation for determining wave loads acting on the structural components of the offshore supporting structures that are slender compared to the wave length (e.g. legs, braces, spokes and mooring lines). The comparison results show that the proposed method can be more efficient with time and also a reliable method in initial design of offshore platforms with acceptable results compared to the conventional approach.

1. Introduction

Offshore structures are subjected to different environmental conditions with complex loading combinations such as waves, currents, wind, and sometimes earthquakes or ice [1-3]. Among these forces, the wave-induced loadings are often the most important dynamic excitations for most offshore structures. Therefore, accurate calculation of wave forces acting on offshore structures is essential for safe and reliable design in marine engineering. However, the nonlinearity of the wave loadings would be the main difficulty in such computations, even if the irregularity of wave and nonlinearities of the structure are ignored. Accordingly, a time domain analysis is required in order to determine the most accurate response especially for dynamically sensitive structures, e.g., drag dominated structures. Nevertheless, such calculations are conceptually complicated and computationally expensive. Similarly, experimental methods and local measurements as the other techniques for structure response calculations and behaviour evaluation are not only costly but also very difficult to perform. It is therefore practically necessary to develop worthwhile simplified models with shorter analysis time duration than usual models for engineering analysis applications at an early stage of the design process. The importance of establishing such models is that it does not only allow the engineers to have a better interpretation of the dynamic behaviour of the structure by driving analytical solution but also provides a good basis for validation of numerical method's results [4].

Numerous studies have been carried out using Morison's equation [5] for wave loading estimation on the cylindrical slender structural members of offshore structures. However, despite the good estimation of wave loads provided by this model, the nonlinearity existing in its drag force component makes the dynamic analysis of the drag dominated structures prohibitively time consuming and therefore it has limited applications in usual design and assessment practice of offshore platforms. Consequently, developing more economic and reliable analytical solution techniques are desirable.

Over the last few decades, many research studies have been dedicated to modify and linearize Morison's

model in order to simplify the load and response estimation procedure of offshore structures comprised of cylindrical slender elements. The most extensively used linearized form of Morison's equation was proposed by [6-8] using equivalent linearization technique developed by [9]. The main advantage of this linearization besides drastically reduction of the computational time is that the excitation force and corresponding response become stochastically stationary and Gaussian [10, 11], so many efficient numerical methods can be used to assess the structural behaviour in frequency domain [12, 13]. Nevertheless, since this approximation significantly underestimates the distribution of wave force [14, 15]; [16] modified the original linear form of Morison's equation and obtained a new coefficient for the linearized drag force component, in which it gives a better estimation of the nonlinear wave-induced forces. Also, [4] derived a new linearized form of drag component utilizing a same technique with considering the probability density instead of spectrum of the wave force used to drive the original model which provides a more accurate approximation of wave force than the Borgman's model. Moreover, [17] discussed the major limitation with the classical Gaussian equivalent linearization method using the well-known mean square error criterion and proposed an approximate series including the conventional one as the first approximation for the coefficients of the equivalent linearized drag force in the Morison's equation through a new mean square criterion based on Hermite polynomial error sample functions. The Borgman's linearized model was developed for unidirectional wave forces; therefore, due to limitations of the model with vector operation rules, [18] added some modification and presented a new linearized model applicable for multi-directional wave flow. [19] extended the conventional linearized model using statistical linearization technique for nonzero-mean stochastic in case of waves and currents co-occurrence. [20] discussed the great limitations of Borgman's linearization technique in extreme wave loading and wave-induced fatigue loading calculations illustrated well by [21] and used an alternative linearization to make this equation applicable for such cases. Apart from the aforementioned studies on linear predictions, other higher-order solutions have also been proposed in order to reduce the errors originated by the linearization approaches as much as possible [21].

The main objective of this study is to introduce new simplified approximation models for hydro dynamical wave loads calculation applied on cylindrical members of offshore platforms based on linear wave theory and the Morison's equation. For this purpose, first, the non-linearized and linearized model of Morison's equation for regular wave cases with and without considering the effects of the instantaneous free water-wave surface are discussed. Then, the alternative simplified methods based on two ideas: linear and uniform distributions of wave force in depth, are developed. Afterwards, in order to verify the applicability and accuracy of the proposed calculation methods, the important parameters governing the behavior of the offshore structures (i.e., wave-induced base shear and overturning moment) for a single cantilever representative cylinder in a unidirectional flow are compared with the nonlinear and linearized Morison's wave-induced forces.

2. Wave Loading

The evaluation of structural and motion responses are essential in the assessment of operability of offshore structures. The design loads especially hydrodynamic forces have crucial roles in the design of offshore structures. Therefore, many research efforts have been dedicated on the development of an appropriate hydrodynamic load calculation modeling procedure especially the computation of wave induced loads for either the fatigue or extreme cases. In the recent years, there has been a significant improvement in the prediction of wave loads imposed on offshore structures. In this regard, linear and nonlinear methods including time domain numerical approaches and frequency domain techniques using different wave theories (linear and non-linear) and wave loading calculation methods (i.e., Morison's method, Diffraction theory, Froude-Krylov method, and Computational Fluid Dynamic (CFD)) as well as probability analysis have been utilized [22].

3. Morison Equation Considering Deep Water-Wave Conditions

The correct calculation of the wave load on the support structures depends on selecting an appropriate load-calculation model in the simulation (see Figures 1 and 2). The suitable approach to calculate the total time-varying wave loading per unit length acting normal to the slender members (i.e., the ratio of member diameter to the wavelength is less than 0.2) is Morison's equation. According to this theory, such structures do not significantly affect the wave particle motions and the wave induced forces originate from inertia and viscous effects. The horizontal wave loads (i.e., Morison's forces) per unit length for certain depth of motionless member below the mean water surface can then be expressed as the sum of inertia force (i.e., added mass), f_I, and drag force, f_D, as follows [23-25].

$$f(z,t) = f_I + f_D = \rho C_I V_b a_x + \frac{1}{2}\rho C_D A_p u_x |u_x| \qquad (1)$$

In which, ρ is the water density, C_I is the hydrodynamic inertia coefficient, C_D is the hydrodynamic drag coefficient. Inertia and drag coefficients are functions of the Reynolds number (R_e), Keulegan-Carpenter number (K_c) and relative surface

roughness of structural member [26, 27]. Values of these coefficients can be obtained from lab or field model tests; however, for conventional engineering works, the values of these coefficients are assumed to be practically constant. According to the [28], the hydrodynamic drag and inertia coefficients are in the range of 0.6 to 1 and 1.5 to 2, respectively. Also, V_b is the volume of the element, A_p is the projected area of the member normal to the direction of the wave motion field, and a_x and u_x are the horizontal wave-induced acceleration and velocity components of the water particle normal to the axis of the member, respectively. The wave particle velocity and acceleration can be computed using different wave theories developed for different specific range of depths; however, the linear small-amplitude wave theory (i.e., Airy) normally provide promising and reliable estimations of this parameter with a shorter computational time, which is a very important factor in real structural design practices. According to the small-amplitude theory as a derivation of first-order velocity potential theory, the horizontal component of water particle kinematics can be determined as follows:

$$u_x = \frac{\omega H}{2}\left(\frac{\cosh\left[k\left(z+d\right)\right]}{\sinh kd}\right)\cos\left(kx-\omega t\right) \tag{2}$$

$$a_x = \frac{\omega^2 H}{2}\left(\frac{\cosh\left[k\left(z+d\right)\right]}{\sinh kd}\right)\sin\left(kx-\omega t\right) \tag{3}$$

where, H is the wave height, T is the wave period, d is the water depth, z is the depth of member below the mean water surface, and $k = 2\pi/\lambda (wave\ length)$ and $\omega = 2\pi/T$ are the wave number and wave angular frequency, respectively. Hence, by substituting the horizontal component of water particle kinematics given by Eq. (3) into Eq. (2) and integrating the force per unit length acting on the structure from the mud line up to the mean water surface level (see Figure 3), the total wave force can be calculated as follows:

$$F = \int_{-d}^{0} f\ (z,t)dz \tag{4}$$

$$F_I = -\frac{\rho C_I}{2k}\frac{\pi D^2}{4}\omega^2 H sin(\omega t) \tag{5}$$

$$F_D = \frac{\rho C_D D}{32k}\left(\omega H\right)^2 \times \left(\frac{2kd + sinh(2kd)}{sinh^2(kd)}\right)cos\,\omega t\,|cos\,\omega t| \tag{6}$$

This equation (i.e., Eq. (4)) would be limited only to drag force component in cases where the structures are drag dominated, $D/H < 0.16$ (see Figure 2). This can be shown as:

$$\frac{F_{D_{max}}}{F_{I_{max}}} = \frac{1}{4\pi}\frac{C_D}{C_I}\left(\frac{2kd + sinh(2kd)}{sinh^2(kd)}\right)\left(\frac{H}{D}\right) \tag{7}$$

$$Deep\ water \rightarrow sinh(kd) \approx \frac{e^{kd}}{2}$$

$$\left(\frac{2kd + \frac{e^{2kd}}{2}}{\frac{e^{2kd}}{4}}\right)_{d\rightarrow\infty} \approx \left(2 + \frac{8kd}{e^{2kd}}\right)_{d\rightarrow\infty} \approx 2 \tag{8}$$

$$C_I = 1,\ C_D = 1$$

$$\frac{F_{D_{max}}}{F_{I_{max}}} = \frac{1}{2\pi}\left(\frac{H}{D}\right) \tag{9}$$

$$\frac{D}{H} << \frac{1}{2\pi} \rightarrow \frac{F_{D_{max}}}{F_{I_{max}}} >> 1$$

Therefore, the total wave loads in such cases, which encompasses the kind of structures are considered in this study, can be rewritten as follows:

$$f\ (z,t) = f_D = \frac{1}{2}\rho C_D A_p u_x\,|u_x| \tag{10}$$

The desribe kinematics of the wave in the Airy linear wave theory is only valid up to the mean sea level; Accordingly, to provide a more realistic representation of wave loads near the mean sea level, it is neccessary to apply some modifications to the water particle velocity definition obtained from the linear wave theory in order to take into account the effects of free surface fluctuations. For this purpose, various extrapolation teqniquies such as Wheeler, vertical, and linear stretching methods, which have been widely utlized in practice, can be used. İn the vertical and linear stretching methods, the water particle velocity at the mean sea level is assumed to be extrapolated to above MSL with zero and constant partial derivation, respectively. In the Wheeler stretching method, which is used in this study as the most commonly utilized method, the extrapolation is applied through coordinate mapping as follows, so that the profile is stretched and redistributed to instantaneous free surface elevation of wave [29]:

$$z = \frac{z_s - \eta}{1 + \frac{\eta}{d}} \tag{11}$$

In this case, the wave kinematics and total wave force can be calculated as follows:

$$u_x = \frac{\omega H}{2} \times \frac{cosh\left[k\left(z+d\right)\left(\frac{d}{d+\eta}\right)\right]}{sinhkd} cos\left(kx-\omega t\right) \tag{12}$$

$$a_x = \frac{\omega^2 H}{2} \times \frac{\cosh\left[k\left(z+d\right)\left(\frac{d}{d+\eta}\right)\right]}{\sinh kd} \sin(kx - \omega t) \quad (13)$$

which yields to:

$$F^{Stretched} = \int_{-d}^{\eta} f\,(z,t)dz \quad (14)$$

$$F_I^{Stretched} = \left(\frac{d+\eta}{d}\right) F_I \quad (15)$$

$$F_D^{Stretched} = \left(\frac{d+\eta}{d}\right) F_D \quad (16)$$

It should be noted that in cases where the structural movement is considerable, the relative velocity and acceleration contributed from the fluid-structure interaction must be accounted in the calculation of hydrodynamic forces.

For the ultimate/collapse capacity design purposes, the global analysis of structures through parameters giving the dominant responses is required [30]. Such evaluation is usually performed by calculating the maximum global loads (i.e., base shear and overturning moment) which may govern the design of braces and leg members. To obtain the maximum base shear and overturning moment, since each member will not be attaining the maximum loads due to its location relative to wave; hypothetically, it should be assumed that the wave crest is positioned relatively at the origin of each member even though the obtained responses and hence the design would be highly conservation [31, 32]. These parameters can be calculated for as follows:

$$M_T = \sum_{i=1}^{N}\left[F_i * \Delta z_i * (d - |z_i|)\right] \quad (17)$$

$$F_T = \sum_{i=1}^{N}\left[F_i * \Delta z_i)\right] \quad (18)$$

where N is the number of segments along the length of element, F_i is the lateral wave forces per unit length at the centroid of segment i, Δz_i is the subdivision steps size of the member length associated with node i, d the depth of water, and z_i is the depth of node i below the mean water surface.

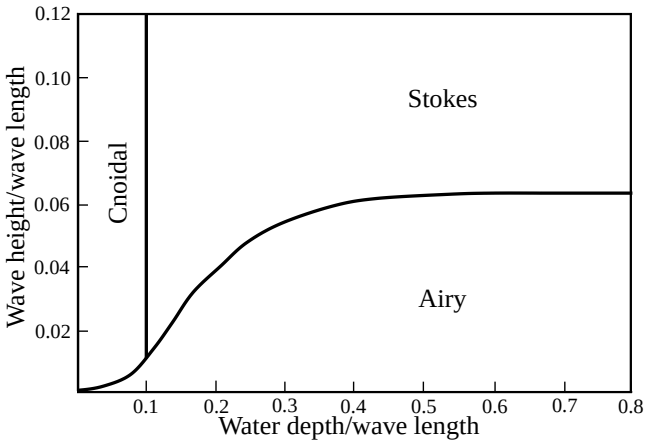

Figure 1. The validity ranges of different water wave theories [33].

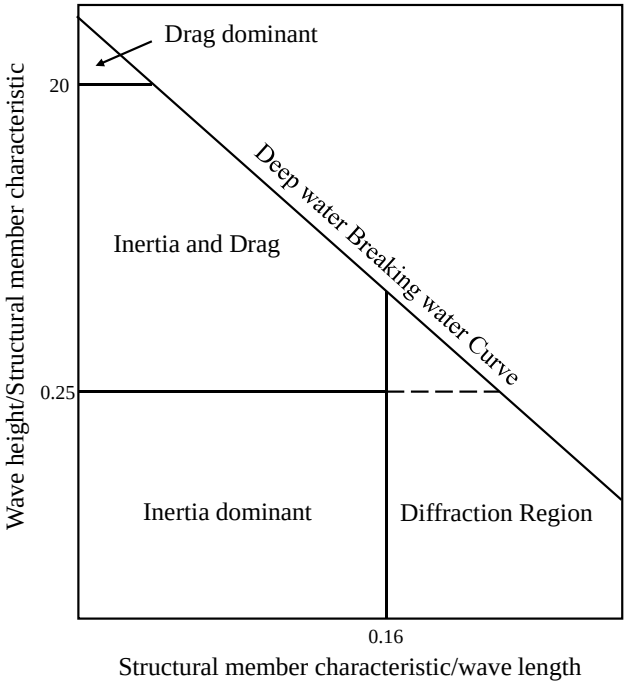

Figure 2. The dominating wave force regimes [23].

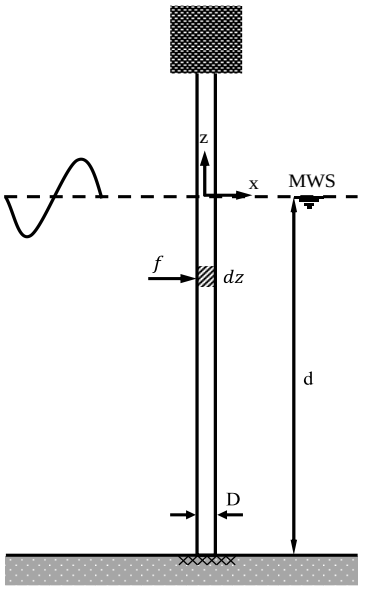

Figure 3. The schematic of the partial force of the wave acting on a representative contilevered vertical cylinder

4. Linearization of Morison's Equation

In the Morison's equation, the inertia force term is a linear function of particle acceleration components while the drag force term is a nonlinear function of particle velocity components which makes the implementation of wave loading calculation algorithm conceptually and practically very difficult. As a result, linearization of this term is very important in cases like that is intended to use a mixed approach and combining the Morison's equation with the diffraction potential theory in order to solve the governing equation of motion in the frequency domain. Consequently, in regular waves where a cosine variation in velocity, $u = u_0 \cos \omega t$ is assumed, the nonlinear drag term of Morison's equation can be linearized using the Fourier series expansion as follows:

$$F_D = A_D \cos \omega t . |\cos \omega t| = A_D \left(a_0 + \sum_{n=1}^{\infty} \left(a_n \cos n\omega t + b_n \sin n\omega t \right) \right) \quad (19)$$

In which,

$$a_0 = \frac{\omega}{2\pi} \times \int_0^{2\pi/\omega} A_D \cos \omega t \, |\cos \omega t| dt = 0$$

$$a_n = \frac{\omega}{\pi} \times \int_0^{2\pi/\omega} A_D \cos \omega t \, |\cos \omega t| \cos \omega t dt = A_D \times \left(\frac{8}{3\pi} \cos \omega t - \sum_{n=1}^{\infty} \frac{8 \sin\left((2n+1)\omega t \right)}{\pi (2n-1)(2n+1)(2n+3)} \right) \quad (20)$$

$$b_n = \frac{\omega}{2\pi} \times \int_0^{2\pi/\omega} A_D \cos \omega t \, |\cos \omega t| \sin \omega t dt = 0$$

The higher-order harmonics have less effects on the response due to less amplitude and energy than the fundamental harmonic and structural dynamics [34]. Therefore, the fundamental harmonic seems to be sufficient order of expansion and the linearized drag force can be given by:

$$F_D = A_D \left(\frac{8}{3\pi} \cos \omega t + higher \ \ harmonics \right) \approx A_D \frac{8}{3\pi} \cos \omega t \quad (21)$$

5. Equivalent Simplified Approximation Expressions of Morison's Equation

Another approach to reduce the complexity and computational cost of using drag term directly into the numerical wave loading calculation algorithm in situations mentioned before especially cases involved with high nonlinearities is to develop much simpler yet precise mathematical formulas to estimate the wave-induced forces. Accordingly, in this study, to overcome this problem, first, the usefulness of deep water limitation which is a reasonable assumption in the procedure of driving the simplified model for calculating the wave forces acting on Morison's type framed structures is considered. Based on this limitation, the terms in bracket in Eqs. (2) and (12), which show the variations of components over the vertical water column, can be rewritten as follows:

$$Deep\ water: \left\{ \begin{array}{l} \left(\dfrac{cosh\left[k\left(z+d \right) \right]}{sinhkd} \right) \\ \left(\dfrac{cosh\left[k\left(z+d \right)\left(\dfrac{d}{d+\eta} \right) \right]}{sinhkd} \right) \end{array} \right\}_{d \to \infty} = e^{kz} \quad (22)$$

In which, substitution of this simplification into the horizontal component of water particle velocity given by Eq. (2) yields to the following equation for wave force per unit length on drag dominated structures:

$$f(z,t) = \frac{1}{2} \rho C_D D \left(\frac{\omega H}{2} \right)^2 \times e^{2kz} cos\left(kx - \omega t \right) \left| cos\left(kx - \omega t \right) \right| \quad (23)$$

By taking into account the unit values with appropriate order of magnitude for parameters including the water density, $\rho = 1000 kg/m^3$, diameter of the member, $D = 1\, m$, and hydrodynamic drag coefficient, $C_D = 1$, the magnitude of maximum total unit wave load at the mean water surface level, f_0, in a sea state can be obtained as follows:

$$f(z,t) = f_0 e^{2kz} cos\left(\omega t \right) \left| cos\left(\omega t \right) \right| \quad (24)$$

where,

$$f_0^{[kg]} = 50 v_0^2 \ , \ v_0^2 = \left(\frac{\omega H}{2} \right)^2 \quad (25)$$

The reason for deriving this equation is to show that the magnitude of maximum total unit wave force at the mean water surface level in drag dominated structure can be simply carried out by knowing only the value of horizontal component of water particle velocity. This outcome is very important because it can be very usful in practical cases. Accordingly, for further simplification,

simplified expressions for term, v_0, the amplitudes of horizontal water particles velocity at the mean sea level are elaborately extracted using the curve fitting teqnique through least-squares regressive minimization function. This approach then leads to concise expressions of wave kinematics within a good range of accuracy which at last results in very practical, reliable, and straightforward wave calculation models for engineering applications in deep water wave conditions. For this porpuse, the relationship between wave height and wave period, $T = 2.94\sqrt{H}$ [29] and dispersion equation definition for deep water conditions, $\omega^2 = gk$ [35] are first considered. Then, using linear regression on these terms yield to the following expressions: (1) $H \approx 1.8T - 6.2$ and (2) $H/\lambda = 0.07$. Figure 4a and b shows the derived linearized relationship between wave height, wave period, and wavelength for deep water conditions. Subsituation of achieved extracion into Eq. (10), the horizontal component of the water particle velocity can then be calculated in a simpler way for waves in deep water conditions, in which the wave height/period is the only parameter needed. Figure 5 shows the water particle velocity as a function of wave height and period using the aforementioned linearized relationships.

$$v_0 = 0.25H + 1 \quad (26)$$

$$v_0 = 0.5T - 1 \quad (27)$$

İt can now be cleary seen that by knowing only one of the main parameters of the wave (i.e., height/period) in a sea state, the magnitude of maximum total unit wave force at the mean water surface level can easily be obtained and to calculate the actual magnitude it just needed to multiply the output by the real values for the water density, diameter of the member, and hydrodynamic drag coefficient.

At last, to calculate the total unit wave-induced base shear force and overturning moment, the distribution of wave forces along each member at any moment is also required. Considering the location of platform members at different depths relative to the wave, each member attains a portion of induced loads. Accordingly, in the present study, the definition of wave penetration depth (Eq. (28)), which seems to play an important role in the amount of forces exerted to the structure, is used to develop two simple approximate methods, in which only one of the main characteristics of the wave in a sea state (i.e., significant wave height/spectral peak frequency) is needed to calculate the base shear and overturning moment of the maximum wave force on the structure.

$$PD(z) = e^{2kz} \quad (28)$$

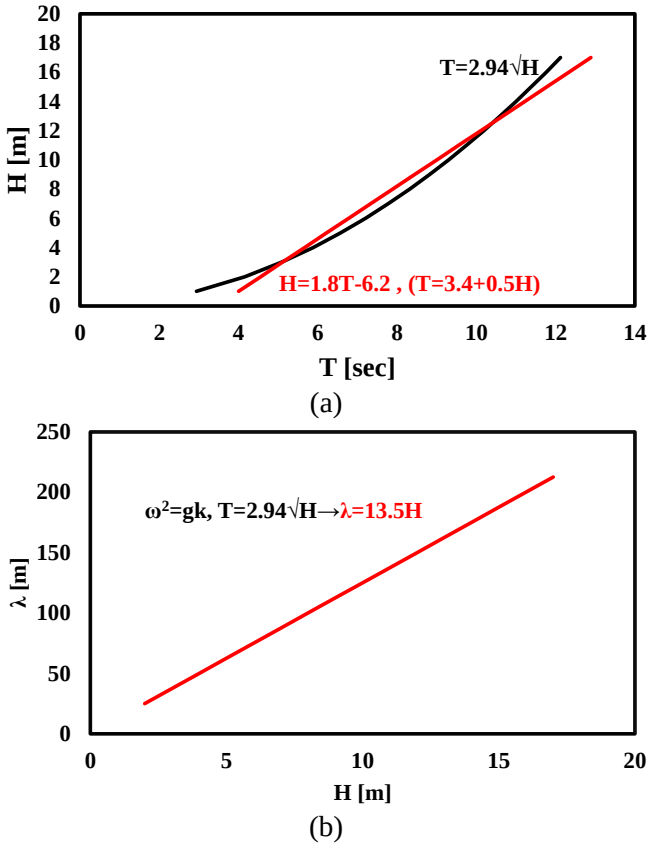

Figure 4. The linearization diagrams of the relationships between (a) the wave height and period (b) the wave height and length.

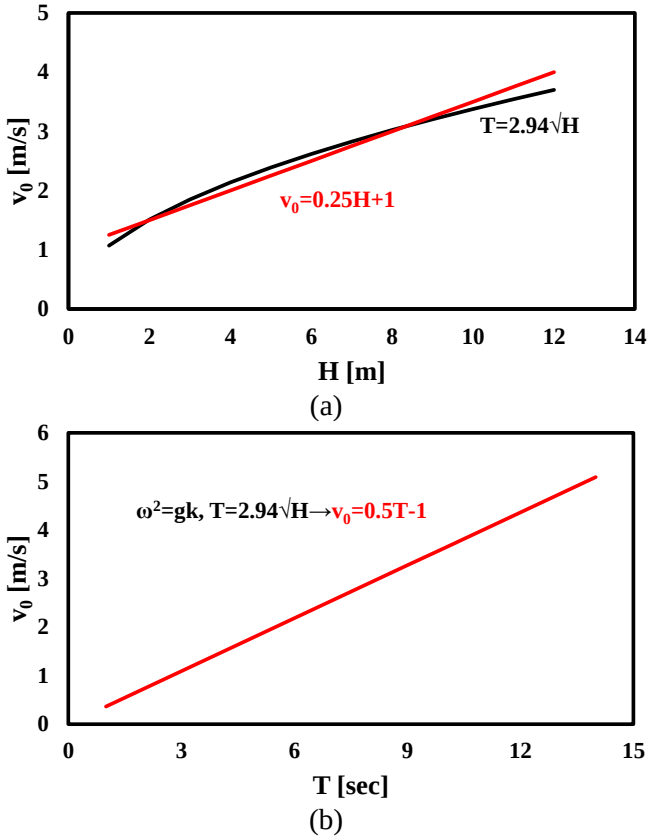

Figure 5. The linearization diagrams of the relationships between (a) the wave height (b) the wave period and horizontal component of the water particle velocity.

In the first method, the exponential distribution of the wave force in depth is replaced by a linear varying distributed (LVD) load segment along the projected length of the members normal to the direction of wave propagation at the instant of maximum wave force. This method is developed based on being able to calculate the total wave force on each member with 90% accuracy with respect to the Morrison's equation. Accordingly, using the Morrison's force amplitude at the mean sea level along with 90% of the total wave force obtained from the Morison's equation at the time when it is maximum yields the penetration depth; and hence, the dimensions of this linear distribution as follows (Figure 7).

$$0.9F_D^0 = \frac{f_0 z_0}{2} \tag{29}$$

$$0.9\left(\frac{\rho C_D D}{16k}(\omega H)^2\right) = 50\left(\frac{\omega H}{2}\right)^2 \frac{z_0}{2} \tag{30}$$

$$\frac{90}{16k}(\omega H)^2 = \frac{50}{8}(\omega H)^2 z_0 \tag{31}$$

$$\frac{0.9}{2\pi}\lambda = z_0 \tag{32}$$

$$z_0 = 0.15\lambda \tag{33}$$

$$\left.\begin{array}{l}\omega^2 = gk \rightarrow T^2 = 0.64\lambda \\ T^2 = 8.6H\end{array}\right\} \rightarrow \lambda = 13.5H \tag{34}$$

$$z_0 = 2H \tag{35}$$

As a result, the maximum estimated magnitude of the base shear force resulted from the net force acting at the one-third of the segment length from above and the total overturning moment of the wave corresponding to this linear distribution approximation about the base can be obtained as follows:

$$\begin{aligned} F^{Tri.} &\approx 50v_0^2 H \\ F_{Streched}^{Tri.} &\approx 62.5v_0^2 H \end{aligned} \tag{36}$$

$$\begin{aligned} M^{Tri.} &\approx 50v_0^2 H\left(d - \frac{2H}{3}\right) \\ M_{Stretched}^{Tri.} &\approx 62.5v_0^2 H\left(d - \frac{H}{3}\right) \end{aligned} \tag{37}$$

where v_0 is determined based on Eqs. (26) and (27).

In the second method, the exponential distribution of the wave force in depth is replaced by uniformly varying distributed (UVD) load segments along the projected length of the members normal to the direction of wave propagation. Two scenarios are considered in this approach: (1) one (UVD1) and (2) two (UVD2) uniform distributed load segments with 90% and 99% accuracy in comparison with the Morrison's equation, respectively. In these scenarios, it is assumed that the penetration depth for both upper and lower segments are the same as the one obtained from the previous method (i.e., $z_0 = 2H$). Accordingly, the magnitude of the upper force distribution at the mean sea level for both first and second scenario is determined based on 90% and the lower force distribution magnitude is carried out based on 9% of the total wave force obtained from the Morison's equation in order to give 99% accuracy from the resultant net forces for the second scenario (Figures 8 and 9).

$$0.9F_D^0 = 2f_0^{\text{Upper Seg.}} H = 20f_0^{\text{Lower Seg.}} H \tag{38}$$

$$\begin{aligned} &0.9\left(\frac{\rho C_D D}{16k}(\omega H)^2\right) \\ &= 2f_0^{\text{Upper Seg.}} H = 20f_0^{\text{Lower Seg.}} H \end{aligned} \tag{39}$$

$$\left.\begin{array}{l}T^2 = 8.6H \\ Deep\ water \rightarrow \omega^2 = gk\end{array}\right\} \rightarrow \begin{cases} f_0^{\text{Upper Seg.}} = 25v_0^2 \\ f_0^{\text{Lower Seg.}} = 1.5v_0^2 \end{cases} \tag{40}$$

Therefore, the maximum estimated magnitude of the base shear force resulted from the net forces acting at the mid-length of the segments and the total overturning moment of the wave corresponding to these uniform distribution approximations about the base can be expressed as follows:

$$\begin{aligned} F^{\text{Upper Seg.}} &\approx 50v_0^2 H \\ F_{Stretched}^{\text{Upper Seg.}} &\approx 62.5v_0^2 H \end{aligned} \tag{41}$$

$$F^{\text{Lower Seg.}} \approx F_{Stretched}^{\text{Lower Seg.}} \approx 3v_0^2 H \tag{42}$$

$$\begin{aligned} M^{\text{Upper Seg.}} &\approx 50v_0^2 H\left(d - H\right) \\ M_{Stretched}^{\text{Upper Seg.}} &\approx 62.5v_0^2 H\left(d - {}^{3H}\!/_{4}\right) \end{aligned} \tag{43}$$

$$M^{\text{Lower Seg.}} \approx M_{Stretched}^{\text{Lower Seg.}} \approx 3v_0^2 H\left(d - 3H\right) \tag{44}$$

where v_0 is determined based on Eqs. (26) and (27).

It should be stated that the penetration depths in both models considering the effects of free surface fluctuations are the same. The numerical procedure of developed simple methods are presented in Figure 6.

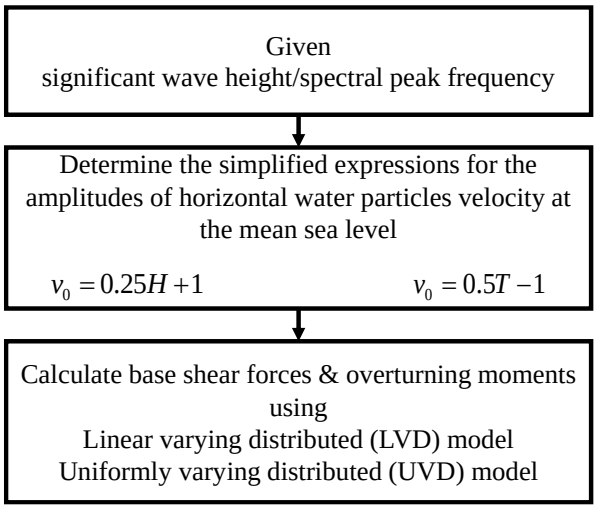

Figure 6. Schematic of developed simple models numerical procedure.

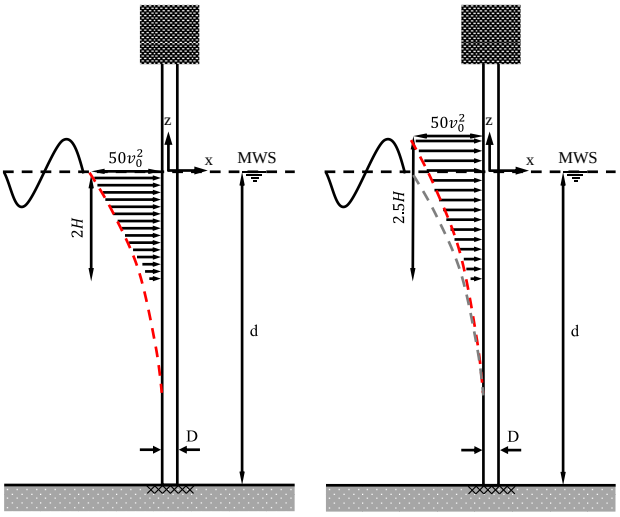

Figure 7. The linear varying distributed (LVD) model (a) with and (b) without considering the effects of the instantaneous free water-wave surface.

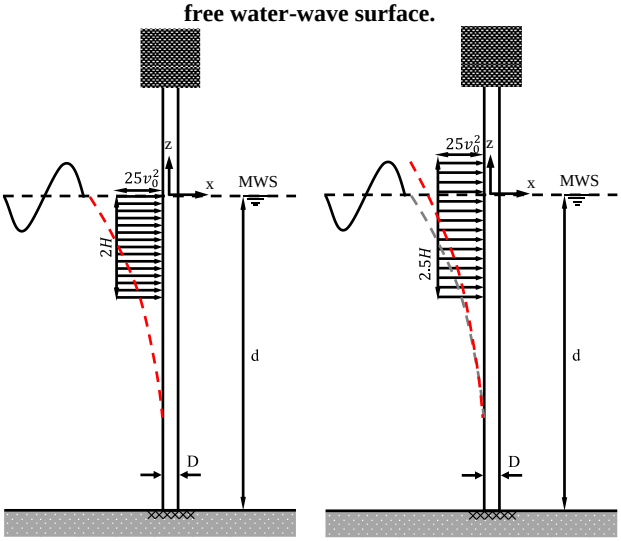

Figure 8. The single segment uniform varying distribution (UVD1) model (a) with and (b) without considering the effects of the instantaneous free water-wave surface.

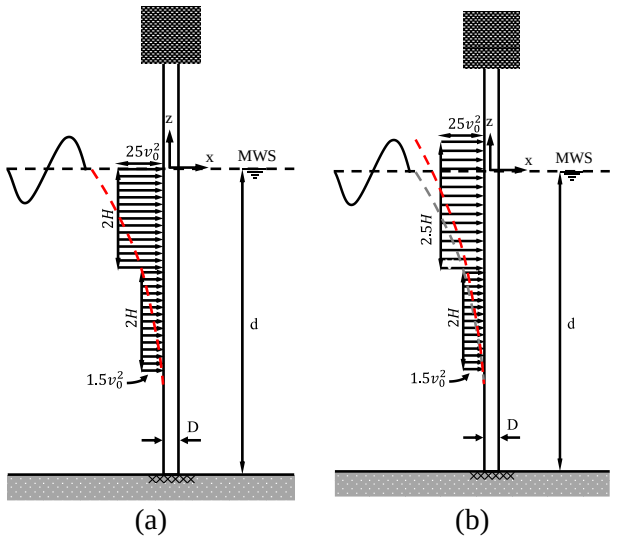

Figure 9. The double segments uniform varying distribution (UVD2) model (a) with and (b) without considering the effects of the instantaneous free water-wave surface.

6. Results and Discussion

6.1. Verification

In order to evaluate the accuracy of the proposed methods, the Demanding Parameters (DPs) (i.e., base shear and overturning moment) of a surface piercing vertical cantilever tabular pile foundation as a representative of the cylindrical shape structural components of the offshore platforms (e.g. monopile foundation, legs, braces, spokes and mooring lines) at 50 m depth are compared with the analytical nonlinear wave-induced forces and existing linearized models. For this purpose, a series of different sea states are considered to assess and verify the performance of these methods. The relevant parameters of the applied load cases are summarized in Table 1.

Table 1. Selected load cases.

Load case	H_s [m]	T_p [sec]
1	1	2.1
2	2	4.16
3	4	5.88
4	6	7.2
5	8	8.3
6	10	9.3
7	12	10.2
8	14	11
9	16	11.8

Figures 10 and 11 compare the computed base shear forces and the corresponding values of overturning moments using different methods without considering the effects of instantaneous free surface fluctuations. It is seen that the wave force distributions along the length of the member calculated based on the linear varying distributed (LVD) distribution approach and single segment uniformly varying distributed (UVD1) approach are in reasonable agreement with the values from conventional approach with little underestimation in all sea states. The comparison results from the double segments uniformly varying distributed (UVD2) approach and the analytical method also show that even though UVD2 method provides a good estimation of base shear forces in low and moderate sea states, the results of this method tend to deviate and overestimate the induced wave forces in the severe sea states mostly because of the overestimation in simplified water particle velocity expressions (see Figures 4 and 5). Regarding the overturning moment, UVD1 method result in a good estimation in all sea states, while the LVD and UVD2 methods yield nearly equal but overestimated especially in severe environmental conditions.

The computed Demanding Parameters using different methods considering the effects of instantaneous free surface fluctuations are also shown in Figures 12 and 13. The comparison results show that the overestimations in both approaches are in a good range of accuracy, while the calculation of overturning moments in LVD method seems to yield in higher but

acceptable overestimation when the effects of free surface is considered. Moreover, it can be observed that both LVD and UVD approach give a better estimation than the linearized model using the Fourier series expansion. Therefore, it can be concluded that the proposed methods yield in reliable, but mostly conservative results which is acceptable in initial calculation design process.

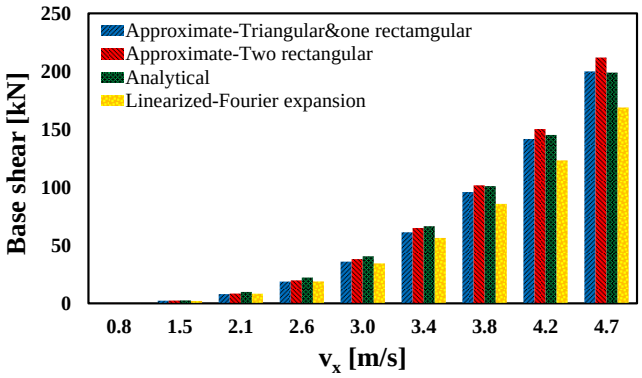

Figure 10. Computed base shear forces without considering the instantaneous free surface fluctuations for different load cases.

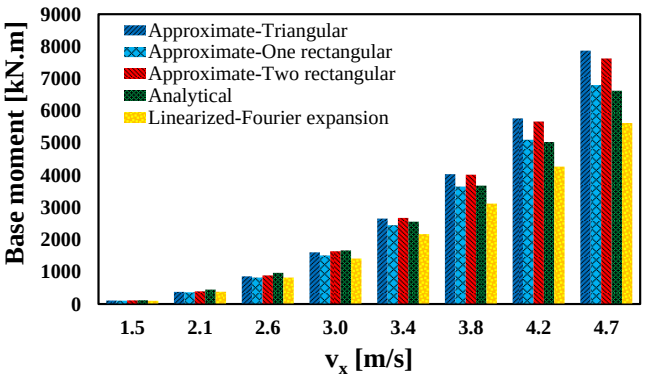

Figure 11. Computed overturning moments without considering the instantaneous free surface fluctuations for different load cases.

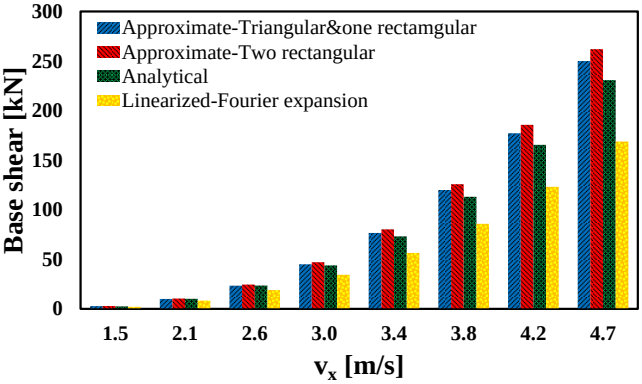

Figure 12. Computed base shear forces considering the instantaneous free surface fluctuations for different load cases.

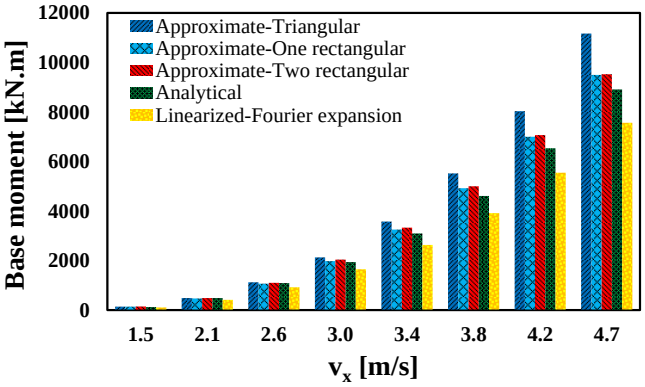

Figure 13. Computed overturning moments considering the instantaneous free surface fluctuations for different load cases.

6.2. Numerical case study

In addition to the previous section, a real scaled tested offshore jacket platform [36] is selected to evaluate the application of the simplified proposed methods in comparison with typical approach. The platform has four battered legs with diagonal brace members in vertical plans and is located in 4.88 m water depth. Structural elements perspective and properties of the platform is shown in Figure 14. The Airy wave theory with the wave height assumed to be equal to one-twentieth of the wave length was considered in all the perform tests presented in [36]. The experimental results were also carried out assuming inertia and drag coefficients to be equal to 2.0 and 1.0, respectively.

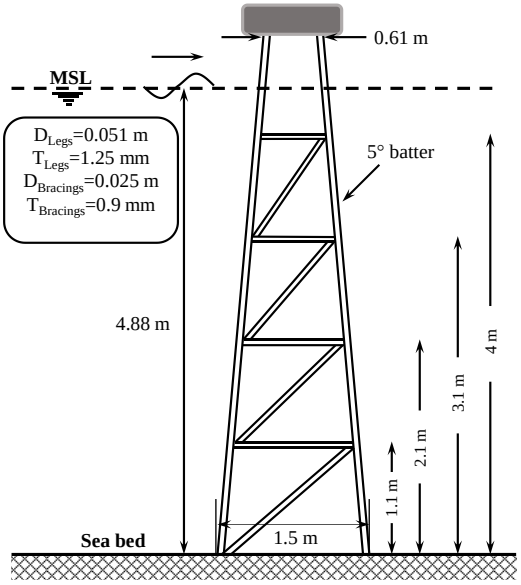

Figure 14. Schematic of the selected jacket platform and its structural properties.

To compute the total wave force (i.e., base shear) on the structure for both nonlinear and simplified proposed wave-induced forces, a three-dimensional (3D) numerical finite element model is developed using MatLab®. In this model, a linear interpolation between four calculation points along each element is considered to calculate the wave load on each member. Nevertheless, before comparing the results for the real

platform, the accuracy of developed FEM model is investigated for the surface piercing vertical cantilever beam studied in the previous subsection. From Figure 15, it is can be observed that the developed FEM model results in reasonable values in both high and low frequencies compared to conventional and simplified approaches, which validate the developed numerical model.

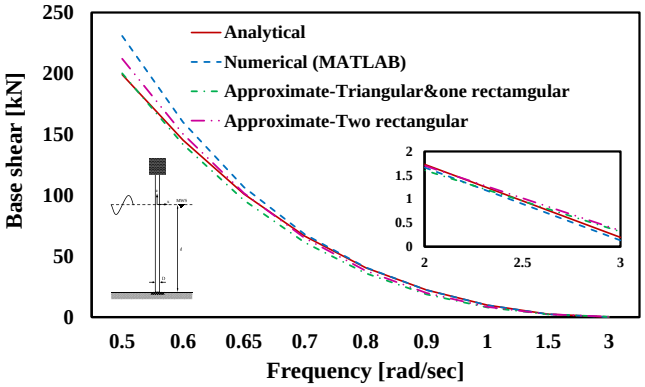

Figure 15. Verification of developed FEM model for base shear forces without considering the instantaneous free surface fluctuations for different excitation frequencies.

The developed finite element model is then used for the jacket platform (see Figure 16). The comparison with experimental data presented in Figure 17 shows a good match between the analytical, numerical, and simplified methods, which proves the accuracy of proposed methods in this study for a real platform. It should be stated that although the comparison result for the jacket platform does not validate the simplified methods developed in this study for lower frequency than 2 rad/sec due to unavailable experimental data, since the validation is examined for such low frequency range of a surface piercing vertical cantilever beam, it is assumed that these methods are applicable for low, moderate, and high excitation frequencies.

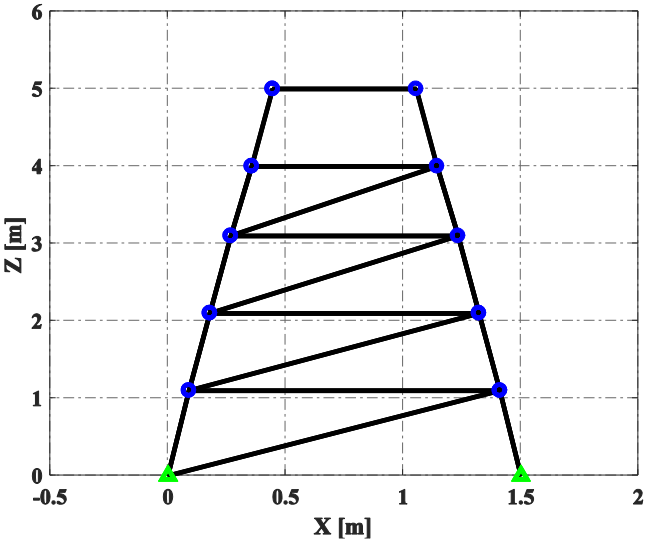

Figure 16. Two-dimensional view of the developed finite element model of the jacket platform.

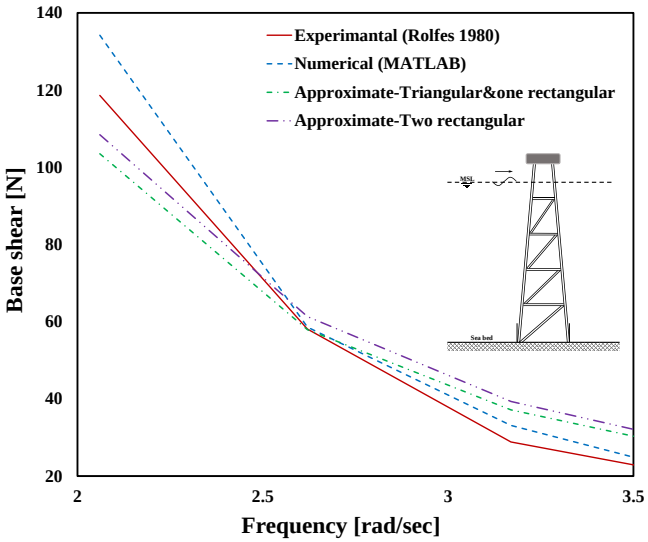

Figure 17. Comparison of computed base shear forces and experimental results of the small offshore test structure without considering the instantaneous free surface fluctuations.

7. Conclusions

This study presented details on driving new simplified approximation models incorporating the hydro dynamical wave forces calculation applied on framed members of offshore structures based on linear wave theory and the Morison's equation. In order to verify the accuracy of the proposed calculation methods, the static base shear force and overturning moment by the base line of a representative pile foundation/slender member are computed by the developed simplified expressions in different sea states and compared with the existing linearized model as well as the nonlinear Morison's equation. Moreover, the applicability of the proposed simplified methods is evaluated in comparison with experimental results of a real scaled tested offshore jacket platform. The results show that the achieved simplified models give good and realistic estimations of the maximum wave loads; and hence, corresponding maximum static base shear forces and overturning moments. Accordingly, utilizing such approximations not only make the hydro dynamical modeling and behaviour assessment of offshore support structures such as TLPs and semi-submersible platforms consist of large and small bodies more feasible and more implementable through mixed approaches (e.g., potential theory and Morison's equation) but also very viable for using in the first steps of design because of its smaller required computational time.

8. References

[1] Babaei, S., Amirabadi, R., & Sharifi, M. (2022). *Probabilistic Seismic Assessment and Fragility Curves for Fixed Pile-Founded Offshore Platforms*, International Journal Of Coastal, Offshore And Environmental Engineering (ijcoe), Vol. 7(1), p. 50-62. DOI: https://doi.org/10.22034/ijcoe.2022.151074.

[2] Erfani, M.H., Tabeshpour, M.R., & Sayyaadi, H. (2019). *Capacity Evaluation of Ressalat Jacket of Persian Gulf Considering Proper Finite Element Modeling of Tubular Members*, International Journal Of Coastal, Offshore And Environmental Engineering (ijcoe), Vol. 4(2), p. 55-63. DOI: https://doi.org/10.29252/ijcoe.3.2.55.

[3] Ghasemi, M.R., Shabakhty, N., & Enferadi, M.H. (2019). *Optimized SMA Dampers in Vibration Control of Jacket-type Offshore Structures (Regular Waves)*, International Journal Of Coastal, Offshore And Environmental Engineering (ijcoe), Vol. 4(4), p. 25-35. DOI: https://doi.org/10.29252/ijcoe.2.4.25.

[4] Song, J.B., Wu, Y.H., & Collinson, R. (1987). *A new linearized equation of random wave forces*, School of Mathematics and Statistics, Curtin University of Technology, GPO BOX U, Perth, Western Australia 6001, Vol.

[5] Morison, J., Johnson, J., & Schaaf, S. (1950). *The force exerted by surface waves on piles*, Journal of Petroleum Technology, Vol. 2(05), p. 149-154. DOI: https://doi.org/10.2118/950149-G.

[6] Borgman, L.E. (1965). *The spectral density for ocean wave forces*, in Proceedings Santa Barbara specialty conference, ASCE.

[7] Borgman, L.E. (1967). *Random hydrodynamic forces on objects*, The Annals of Mathematical Statistics. DOI: http://www.jstor.org/stable/2238868.

[8] Borgman, L.E. (1972). *Statistical models for ocean waves and wave forces*, Advances in Hydroscience, Vol. 8, p. 139-181. DOI: https://doi.org/10.1016/B978-0-12-021808-0.50008-5.

[9] Bogoliubov, N.N., & Lefschetz, S. (1947). *Introduction to non-linear mechanics*. Vol. 11. Princeton University Press.

[10] Borgman, L.E. (1965). *A statistical theory for hydrodynamic forces on objects, wave research project report HEL 9-6*. Hydraulic Engineering Laboratory, University of California, Berkeley, California.

[11] Borgman, L.E. (1967). *Spectral analysis of ocean wave forces on piling (coastal engineering conference in santa barbara, california, october 1965)*, Journal of the waterways and harbors division, Vol. 93(2), p. 129-156.

[12] Chandrasekaran, S., Jain, A., & Chandak, N. (2004). *Influence of hydrodynamic coefficients in the response behavior of triangular TLPs in regular waves*, Ocean Engineering, Vol. 31(17), p. 2319-2342. DOI: https://doi.org/10.1016/j.oceaneng.2004.06.005.

[13] Haritos, N. (1995). *Modelling the inertia force dominant response of compliant offshore structures in 3-dimensional wave environments*, Environment international, Vol. 21(5), p. 637-645. DOI: https://doi.org/10.1016/0160-4120(95)00079-Z.

[14] Rolfes, M., & Dawson, T. (1981). *Forces on a Large Scale Offshore Test Structure in Random Waves*, in International symposium on hydrodynamics in ocean engineering. Preprints, 1981.

[15] Tickell, R. (1977). *Continuous random wave loading on structural members*, Structural Engineer, Vol. 55(Analytic).

[16] Terro, M.J., & Abdel-Rohman, M. (2007). *Wave induced forces in offshore structures using linear and nonlinear forms of Morison's equation*, Journal of Vibration and Control, Vol. 13(2), p. 139-157. DOI: https://doi.org/10.1177/1077546307067085.

[17] Thinh, N., Anh, N., & Cuong, D. (1998). *An equivalent linearization for the drag force in the morison's equation using hermite polynomial error sample function*, Vietnam Journal of Mechanics, Vol. 20(2), p. 55-64. DOI: https://doi.org/10.15625/0866-7136/10021.

[18] Housseine, C.O., et al. (2015). *A new linearization method for vectorial Morison equation*, in Proceedings of the 30th International Workshop on Water Waves and Floating Bodies, Bristol (UK).

[19] Spanos, P.D., & Chen, T.W. (1981). *Random response to flow-induced forces*, Journal of the Engineering Mechanics Division, Vol. 107(6), p. 1173-1190. DOI: https://doi.org/10.1061/JMCEA3.0002774.

[20] Wolfram, J. (1999). *On alternative approaches to linearization and Morison's equation for wave forces*, Proceedings of the Royal Society of London A: Mathematical, Physical and Engineering Sciences. The Royal Society. DOI: http://www.jstor.org/stable/53464.

[21] Brouwers, J., & Verbeek, P. (1983). *Expected fatigue damage and expected extreme response for Morison-type wave loading*, Applied Ocean Research, Vol. 5(3), p. 129-133. DOI: https://doi.org/10.1016/0141-1187(83)90066-4.

[22] Hirdaris, S.E., et al. (2014). *Loads for use in the design of ships and offshore structures*, Ocean engineering, Vol. 78, p. 131-174. DOI: https://doi.org/10.1016/j.oceaneng.2013.09.012.

[23] Chakrabarti, S.K. (1987). *Hydrodynamics of offshore structures*. WIT press.

[24] Faltinsen, O. (1993). *Sea loads on ships and offshore structures*. Vol. 1. Cambridge university press.

[25] Patel, M.H. (1989). *Dynamics of offshore structures*. Springer-Verlag, Berlin. DOI: https://doi.org/10.1016/C2013-0-04045-5.

[26] Sarpkaya, T. (1986). *In-line and transverse forces on smooth and rough cylinders in oscillatory flow at high Reynolds numbers*, Journal of ship Research, Vol. 21(04), p. 200-216. DOI: https://doi.org/10.4043/2533-MS.

[27] Sarpkaya, T. (2010). *Wave forces on offshore structures*. Cambridge university press.

[28] API-RP2A-WSD (2007). *Recommended practice for planning, designing and constructing fixed offshore platforms–working stress design*. American Petroleum Institute, Washington, DC, USA.

[29] DNV-RP-C205 (2017). *Environmental Conditions and Environmental Loads*. Det Norske Veritas group, Norway.

[30] DNV-Report-No.95-3203 (1996). *Guidelines for Offshore Structural Reliability Analysis–Application to Jacket Platforms*. Det Norske Veritas group, Norway.

[31] Chandrasekaran, S. (2014). *Ocean Structures and Materials*. National Programme on Technology Enhanced Learning (NPTEL).

[32] Nallayarasu, S. (2009). *Offshore Structures Analysis and Design*. Madras: Department of Ocean Engineering, Indian Institue of Technology Madras.

[33] Dawson, T.H. (1983). *Offshore structural engineering*. United States.

[34] Templeton, J.S. (2007). *Offshore Technology in Civil Engineering, Volume Two: Hall of Fame Papers from the Early Years*. Vol. 2. ASCE Publications.

[35] Dean, R.G., & Dalrymple, R.A. (1991). *Water wave mechanics for engineers and scientists*. Vol. 2. World scientific publishing company. DOI: https://doi.org/10.1142/1232.

[36] Rolfes, M.H. (1980). *Wave force and structure response: a comparison of theoretical and experimental results using regular and irregular waves: a Trident Scholar Project Report*. (No. 108). US Naval Academy.

INTERNATIONAL JOURNAL OF
COASTAL, OFFSHORE & ENVIRONMENTAL ENGINEERING IJCOE Vol.9/No. 1/winter 2024 (55-63)

Available online at: www. Ijcoe.org *Manuscript Type: Original Research Article*

Comparison of different support vector machine kernels for monitoring of the last decade of the Iranian part of eastern Caspian Lake

Sina Gholizadeh[1], Reza Dezvareh[2*], Abbas Kiani[3]

[1] *MSc Student, Faculty of Civil Engineering, Babol Noshirvani University of Technology, Babol, Iran.*
[2*] *Associate Professor, Faculty of Civil Engineering, Babol Noshirvani University of Technology, Babol; rdezvareh@nit.ac.ir*
[3] *Assistant Professor, Faculty of Civil Engineering, Babol Noshirvani University of Technology, Babol*

ARTICLE INFO

Article History:
Received: 24 Mar. 2024
Accepted: 10 Jun. 2024

Keywords:
Caspian Sea
Svm
kernel
classification
wet land

ABSTRACT

With the drop in the water level of the Caspian lake in recent years, some part of this water body have become dry lands. The purpose of this research is to provide a method with a low error rate and a reasonable computational cost in order to prepare a map of changes by remote sensing techniques. In this research landsat-8 satellite data were used to extract water areas, under the effect of water indices and with the help of support vector machine. First, the images of the eastern region of the Caspian Sea, which is located in Iran, were prepared, then classified images of two classes of water and land were prepared with the help of the desired bands and water indices with support vector machine processing. Various kernels and indices were used to achieve the most accurate classification method. The classified images were compared with ground truth data to evaluate the classification accuracy. The overall accuracy of the classification in the basic mode with the WRI index and linear kernel was 95.88% and in the best method with the help of the AWEI index and the radial basis function kernel was 97.61%. In the results of the evaluation of the accuracy of change monitoring, the optimal performance of this method was 96.21%. Finally, the optimum classification approach was selected. For future researches, it is better to use this method to examine smaller scale areas.

1. Introduction

Extraction of water zones is an important matter in various fields, management of lake coastal areas, monitoring of coastal changes and monitoring of erosion, flood forecasting and evaluation of water resources are among its applications. Online and timely monitoring of surface water is essential for decision-making processes [1, 2]. Monitoring of land surface changes has been widely used in various remote sensing applications [3, 4]. One of the important advantages of remote sensing methods compared to field methods is that these methods are more economical in terms of time and cost. Spectral remote sensing is used to extract and identify water zones and ice masses on the surface [5].

By combining the use of vector machine-supported processing systems and spectral indices, researchers created a tremendous ability to separate image information. The support vector machine has a suitable capability for extracting image information. One of the important areas for extracting information and separating them from each other are coastal areas and areas covered by water zones. In 2016, Sarp and Ozcelik presented an article titled Extraction of water area and detection of changes using time series to the case study of Lake Burdur from 1986 to 2011. Using Landsat data and SVM-supported vector machine classification and water spectral indices such as NDWI, they separated water zones from image information. In general, the performance of SVM classifier was more accurate than other methods. The level of this accuracy was determined with the help of root mean square error and structural simulation index criterion [1]. In 2022, Munizaga et al. published an article entitled mapping coastal basins using satellite images and machine learning in a highly developed urban landscape to study the coastal region in Chile. They used two approaches of random forest and support vector machine in these classifications. In general, the accuracy of the random forest was higher and the accuracy of the vector machine method supported by SVM was also acceptable, which was generally 88% accurate. They classified the studied areas in four different scenarios related to the

manipulation of input data, such as using the main spectral bands, adding spectral indices, etc. [6, 7]. Also, in 2020, El-Nabwi et al., in an article entitled, an approach based on Landsat images to monitor the coastline in order to cover the integrated coastal management, conducted a case study of the coastal area of the Nile River in Egypt. They carefully monitored the changes in the coastlines and its effect on coastal walls and presented an approach that was a combination of Landsat images and GIS methods. They also classified Landsat data from 1985 to 2018 with the help of vector machine support. SVM classification in this research had an accuracy of 92.6%. They found that 1.2 square kilometers had been eroded in the studied area and they observed 4.4 square kilometers and 10.5 square kilometers of sedimentation in two time periods from 1985 to 2000 and from 2000 to 2018 respectively [7].

Considering the importance of determining land use and land cover, Avci et al. compared random forest and support vector machine algorithms in 2023. They investigated Marmara Lake, which is actually part of a wetland. Examining these areas is very important, especially since these areas have various functions. 3 different training datasets with 10, 15, and 20 areas of interest (AOI) per class, respectively, were used to classify satellite images acquired in 2015 and 2020 [8].

In 2024, Zhao et al presented a research with the aim of investigating the performance of different support vector machine algorithms such as CART, random forest and support vector machine in Google Earth Engine using Sentinel-2 data as a data source. They also used several satellite indicators such as mndwi to monitor their study area. Finally, they concluded that despite the good accuracy of svm, the RF algorithm provided better performance than the other two algorithms [9].

In 2020, genbatu et al investigated oasis areas in dry deserts. They identified these areas using machine learning algorithms. Then they compared the performance of each of these algorithms in terms of accuracy. k-nearest neighbor (KNN), random forest (RF), support vector machine (SVM) and artificial neural network (ANN) were used in this research. Landsat-8 Operational Land Imager (OLI) image data with spectral indices and covariates derived from a digital land model were used to classify 7 different land cover categories. In their research, the highest overall accuracy was produced by ANN (97.16%), after which svm and then rf provided the highest accuracy with a close and less difference [10].

The most accurate results were obtained from classification with RF algorithm and 20 AOIs.

In order to extract the features of the image more accurately, the researchers introduced new indicators. They optimized the indicators with various tests. Various researches have been done with the help of these indicators for the purpose of classifying the areas covered by water and soil zones. Lee et al designed a research to identify the most optimal bands for NDWI index. They tested eleven models. Among them, water index using short infrared and green showed the best results [11]. In 2006, Zhang improved the NDWI index in a research to automatically identify water areas, which have noise in some areas, such as built-up areas and vegetation. This research was done using near infrared and mid infrared bands. And to a large extent, it solved the challenges related to NDWI. The developed index is called MNDWI [12]. Munizaga et al also introduced the automatic water extraction index AWEI to increase the accuracy of water extraction in areas that include shadows and dark surface [6]. Feyisa et al. also developed the AWEI index, which led to an increase in the accuracy of identifying water areas in the presence of shade. They prepared flood maps in several different areas using Landsat 5 data. They compared their proposed method with other methods such as MNDWI and the most similar classifier. The results of their research led to the improvement of this index in accuracy and reduction of error in identification compared to analogical approaches [13]. Also, Akbari et al. used the AWEI index in a certain period of time in order to evaluate the changes in the water extent of Maharloo lagoon. They determined four five-year periods and in each period, with the help of this precise index, they investigated the average water area resulting from this index [14].

In 2022, Dodangeh et al. monitored the changes caused by floods in Golestan province with the help of several different approaches including features that were designed from the combination of different indicators and various limits of thresholding and data processing for the purpose of classification. They concluded that combined approaches have the highest accuracy [15]. In 2019, Karimi and colleagues evaluated the hydrodynamics and morphology of the Sefidroud river delta using 2D simulation and remote sensing data. They investigated the sedimentation status of the Sefidroud river delta with the help of MIKE21 software modeling. They concluded that the eastern and western shores of the SefidRoud river delta are being deposited, and the northern coast of the Sefidroud river delta is being eroded [16]. In 2016, Chegoonian et al evaluated the accuracy of classification of coral reef cover using Landsat8 satellite images by using data collection from coral reefs of Qeshm and Lark islands and simultaneous use of remote sensing. They used maximum likelihood classifier. They found that the highest classification accuracy is when they use 2 to 4 classes for classification [17]. Also, Fallah et al evaluated the effects of land use change on the water quality of Anzali International Wetland using Landsat-8 remote sensing data. With the help of statistical analysis and

measurement of parameters such as nitrate, they found out that a large part of the forest area has been converted to other uses such as agricultural land, waterside and city [18].

In 2021, Dodange and colleagues considered the monitoring of Khuzestan and Golestan region in the 2019 flood, which was very extensive. First, an algorithm was prepared to prepare permanent maps of water resources, which included optical satellite images of the last 5 years. Then, flood maps were prepared by using statistical calculations on the time-series bands of radar images, using the normalized indices of the images. The overall accuracy of monitoring the changes in Golestan and Khuzestan provinces was equal to 91.84 and 97.36 percent, respectively [15].

In 2024, researchers studied the Karun River in Iran as a water source in terms of thermal pollution. They found that the construction of dams, the creation of drainage of urban runoff into the Karun River and many other cases have increased the water temperature of the Karun River as a water source. They found out that after the construction of the dam on the Karun river, the average water temperature in the lake behind the dam was 3 degrees cooler than the outgoing water, even in some cases a temperature difference of 13 degrees was observed. They found that remote sensing data can be a good complement to existing ground data so that researchers have more reliable data [19].

Farhadi et al used FWEI in 2024 to monitor flooded areas. The task of this index is to determine the areas covered by water and flooded areas. FWEI uses the average ratio of visible and near-infrared bands obtained from Sentinel-2 images. This person has a very good ability to detect muddy and clear water in small streams of water. The researchers obtained the overall accuracy of this index at about 94.26% and compared to other indices, it offers higher accuracy [20].

In 2022, researchers began to integrate remote sensing and meteorological data with the aim of predicting flood time. Using deep learning algorithm and LSTM network, they tried to predict the 3-day discharge of Aqqala river. Because this network has a good capability for time series predictions. The discharge data of Aqqala station alone and together with its upstream stations, the elevation model of Aqqala city and Golestan province, are used as input network. the findings of the present study were compared with simple regression networks, support vector machine regression and simple neural network. The results indicate the superiority of the long-short-term memory network, despite the high Nash-Sutcliffe correlation of 91% compared to other networks [21].

In 2022, with the aim of automatic identification of flooded areas, researchers collected data for supervised classification of images and identification of flooded areas with the help of integrated indicators. They used Kmeans clustering algorithm, Otsu, Multi and Adaptive thresholds to generate automatic training data. These data were selected based on different water indices (NDWI, AWEI and MNDWI). Then they classified different image classes using different classifiers such as ANN, SVM and MD. In comparison with manual classification, this method provided good accuracy and quality [22].

The important point in this research is the special importance of the study area from an environmental point of view. So that various articles have been presented with remote sensing technique from the studied area which is presented below.

In 2019, Tatian et al. studied the changes in the vegetation cover of Gomishan wetland from 1994 to 2016. By preparing land use maps, they revealed that 87% of the underwater area has dried up and changed its use. They also discovered 5 dominant plant species that have grown significantly in recent years [23].

In another study in the same study area, in 2020, Alavi Panah et al. investigated surface ecological changes of Gomishan Wetland over a 30-year period. They used distance measurement indicators specific to the type of study such as RSEI [24].

In 2022, Hedayati et al investigated the lands covered by Gomishan wetland, they studied the area using Landsat data from 1978 to 2018 in a 40-year period. They revealed that the surface covered by water in 1997 showed the highest amount. Also, in 1978, the lowest level of water coverage was recorded [25] .

Also, in 2023, Khoshravan et al., by examining Gomishan Wetland in terms of shoreline changes from 1995 to 2019, found that most of the changes in the coastline of Gomishan Wetland were in the northern area, and the shoreline changes in the middle and southern areas of the Wetland were smaller, respectively.

They also found that the changes in the shoreline of the wetland received a significant effect from the changes in the water level of the Caspian Sea during the study period [26].

2. Research Significance

Although the use of a processing method such as support vector machine alone after training the user to the system is capable of classifying images, but the combination of various bands and indices has a significant effect on increasing the quality of classification accuracy. One of the great advantages of this method is reducing the error of artificial intelligence systems in classification such as vector machine support. It is worth mentioning that the high rate of automation of this method is a great advantage compared to other traditional methods that are expensive in terms of time or processing. The main advantage of choosing and proposing this method is monitoring with more accuracy and speed and lower

economic cost compared to other existing traditional methods. Monitoring the previous and current status of water areas such as bays, seas and lakes is very important in terms of economy, environment and strategic management in the country.

3. Study Area

A shallow part of the eastern part of Caspian Lake is located in its Iranian part. This area is located in Golestan province. This area is protected from strong waves due to the presence of a sand bar in the western part. For this reason, this area is a safe habitat for wildlife. The very small slope of the studied area is another reason that makes this area safe from the waves. Also, the drop in the water level of the Caspian Lake in recent years has caused the drying of this wetland. The approximate size of the studied area is 180 square kilometers. Figure1 is the used Landsat 8 image as a color image of the study area.

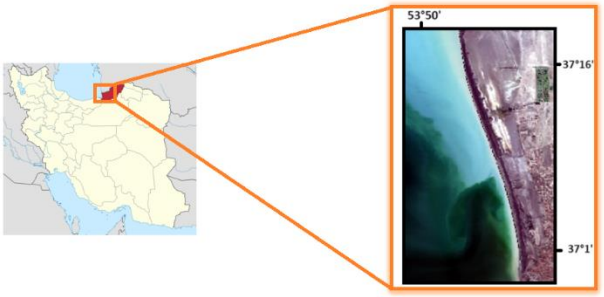

Figure 1. Geographical location of the study area

During the investigations, the water level of the Caspian Lake has been decreasing every year and this trend is still continuing. Only in 2018, after the flood that engulfed Golestan province in Iran, the studied area went under water. The retreat of Caspian lake water has directly affected the study area.

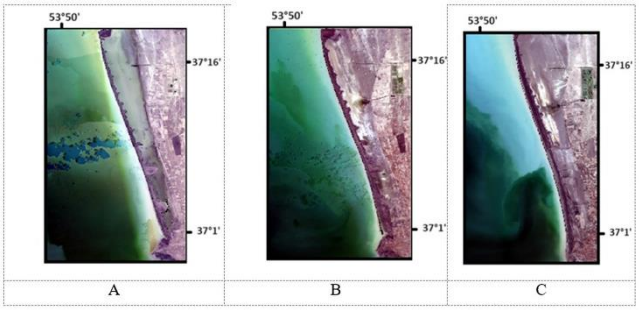

Figure 2. Geographical location of the study area: (A: 2014, B:2017 C: 2023)

The studied area is a coastal area and has a coastal wetland. During the years of study, along with the decrease of the water level of the Caspian Lake in recent years, the coastal wetland has dried up and disappeared. In the western area of this wetland, there is a sand tongue, which makes the coastal wetland to remain enclosed in several directions.

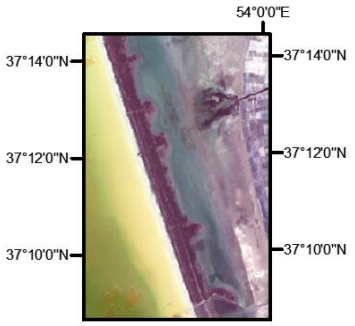

Figure 3. Geographical location of the study area in 2018 after flood

It can be seen that in the first year of the research, a large area of this wetland was under water. But in 2018, after a large flood that engulfed Golestan province in Iran, water was drained to this area. Considering that all the images of this research were selected between the fifth and sixth months of the year in different years, even though 3 months had passed since the flood, the flood water remained in the coastal wetland area.

The continuous decrease in the water level of Caspian Lake is one of the factors affecting the reduction of the surface area of the water zone in the research area. As can be seen in the figure, since 2014, the water level of Caspian Lake has decreased significantly. In the picture above, it can be seen that the water level of Caspian Lake has reached its lowest level in recent years from -25.5 meters compared to the level of open water to -28 meters lower than the level of open water. The Volga River, which is one of the wateriest rivers leading to this lake, has had a decreasing trend in supplying water to this lake in recent years. The share of Volga water supply from this river in 1979 has reached from 74.02% per year to 62.21% in recent years [17].

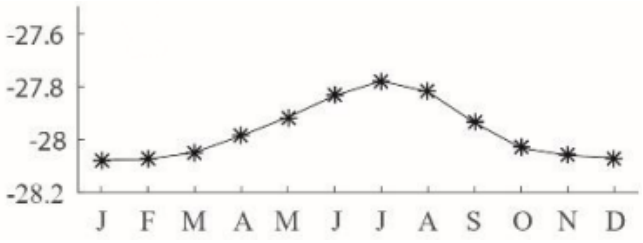

Figure 4. Monthly water level of Caspian Lake [18]

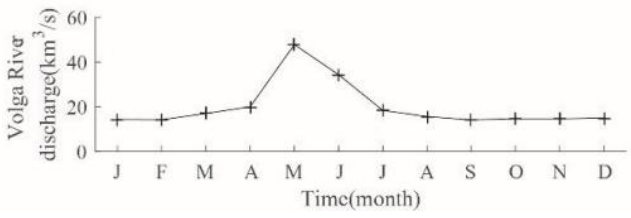

Figure 5. Average discharge of Volga River every month (by 67 years data) [18]

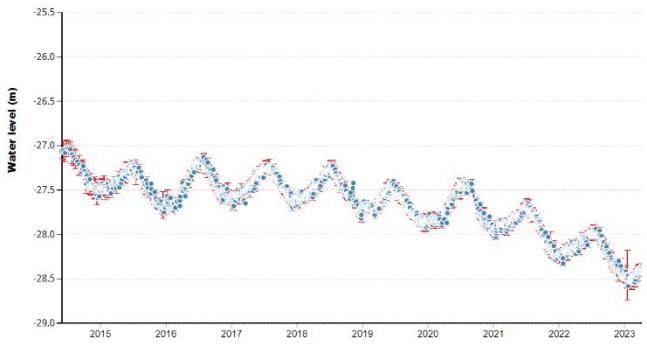

Figure 6. Caspian lake water level changes [19]

As can be seen in Figure 5, the water level of the Caspian Lake in this research was chosen from the fifth and sixth months of the year because the highest water level of the Caspian Lake was recorded in the mentioned months. In the fifth and sixth months of the year, the precipitation and discharge of the Volga River to the Caspian Lake reaches the maximum amount. Therefore, the water level of the Caspian Lake is at its highest level in these two months.

4. Purpose Method

In this article, Landsat images from 2014 to 2023 were used. The cloud filter set for the images was 5%. The data used in this research are Landsat images with a spatial resolution of 30 meters and a temporal resolution of 16 days. Which is obtained from earthexplorer.usgs.gov database. It is very important that the images used and recalled were only from the fifth and sixth months of every year, from 2014 to 2023, because the water level of Caspian Lake is at its highest annual level in this month. Also, due to the small tides of this lake, the need to apply a more accurate time filter is not felt, within a few hours. It is worth mentioning that the studied area, due to its direct connection to the water level of the Caspian Lake, has a similar behavior in terms of water level with the rest of this vast water area. During this research, 3 water indices NDWI, AWEI and WRI were classified by combining 6 bands of Landsat sensors and three processing kernels of vector machine support linear, sigmoid and radial basis function. Finally, the most accurate method was selected.

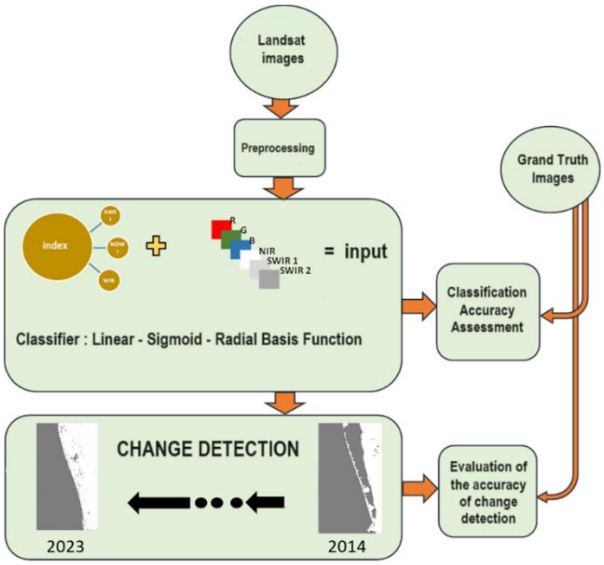

Figure 7. Research steps

Table 1. Specifications of the indices used

indices	equation
AWEI	$BLUE+2.5*GREEN-1.5*(NIR+SWIR1)-0.25*SWIR2$
NDWI	$\frac{green-nir}{green+nir}$
WRI	$\frac{green+red}{nir+swir}$

In the first part of the research, Landsat data was called. Regarding Landsat images, since these images have a suitable repetition period and are recorded every 16 days of the region, they provide a good opportunity to monitor changes in the regions. Then preprocessing was done. Image preprocessing included image normalization, radiometric correction, and calibration. Also, images with less than 5% cloud cover were called. Depending on the type of research, the necessary corrections were made on the images in the environment of Google's inheritance engine. These corrections were performed on 6 bands of the image (2 to 7).

In the second phase, the water indicators along with the desired bands were processed with the help of different computing kernels of vector supported machines. These indices included AWEI, NDWI and WRI. Support vector machine kernels were used in this research, radial, linear and sigmoid basis function kernels. Indicators use several bands to achieve certain goals and finally reach one band [27, 28]. The mentioned indices helped to improve the classification accuracy of Landsat images. During the research, it was revealed that the more the input bands that

classify the images with the index, the higher the accuracy in the output.

Four water indices were applied to each image. Its final output is prepared as a water mask under the effect of support vector machine in three different kernels, RBF, SIGMOID and LINEAR. On the processed images, supervised classification was done in two classes, land and water. Therefore, the land and water map of the studied area was prepared. Some points were made manually in order to train the machine learning system. The combination of water indices with the used bands made the classification of two classes more accurate.

Table 2. Parameter selection of kernels

Kernel	*Gamma parameter*	*C parameter*
Sigmoid	0.05	100
RBF	0.01	100
Linear	-	5

Table 2 shows the selected parameters of c and gamma that were determined in this research. These parameters are embedded to fine-tune the support vector machine classifier.

In order to monitor the changes of each class, change maps were drawn. The method that was optimal in terms of classification accuracy was selected and then the classified maps for the years 2014 to 2023 were prepared. Then these maps were subtracted in the ENVI software environment to obtain class change maps. The changes were divided into three groups: changed to land class, changed to water class and not changed. To evaluate the accuracy of the classification, the maps produced with the ground truth data were prepared, compared and evaluated by an expert user in the ENVI software environment. Kappa coefficient variables, participation and non-participation error and overall accuracy of all kernels and different indices were also calculated. Also, the accuracy of monitoring the changes was obtained from the difference between the images of the beginning and end of the research and the ground reality image of the beginning and end of the research.

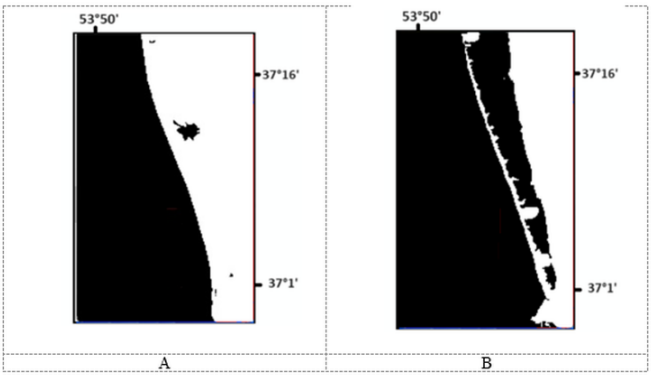

Figure 8. Grand Truth images of the study area: (A: 2023, B:2014)

5. Results and Discussions

In the classification of images, all the combinations of indices and different kernels of the support vector machine worked close to each other in terms of classification accuracy, but visually, especially in sensitive points such as water channels and points where it was difficult to distinguish whether that part of the image is water or land, the kernel of the radial basis function Along with the AWEI index, they provided a very good performance. It is worth noting that the extent of the studied area had a positive effect on the approximation of the figures that indicated the classification accuracy in the image. If the studied area covered a smaller and more diverse range of classification classes, the figures related to classification accuracy would be subject to more and different changes.

The most important part of this research is to obtain the most accurate method for identifying and classifying two classes in the image. To evaluate the accuracy of the classification, it is possible to monitor the overall accuracy and kappa coefficient and the level of accuracy. These calculations were done with the help of three different support vector machine kernels. Calculations were made for the years 2014 to 2023, which gives numerical values as an average of 10 years. These values are listed in Table 2.

Table 2. **Kappa values and overall accuracy of different approaches**

AWEI	WRI	NDWI		
94.31	93.25	94.33	KAPPA	**SIGMOID**
97.46	97.04	97.47	OA	**KERNEL**
93.66	92.89	93.57	KAPPA	**LINEAR**
97.21	95.88	97.17	OA	**KERNEL**
94.35	93.36	94.29	KAPPA	**RBF KERNEL**
97.61	97.09	97.48	OA	

Based on the proposed method of this research, combining Landsat bands with water indicators and then classifying the images with the help of different kernels. We come to the conclusion that despite the closeness of the classification accuracy results, the AWEI index in combination with the bands and classification of the target image based on the radial basis function kernel provided the best performance in terms of accuracy.

According to Table 2, the highest accuracy of image classification was in the approach where the kernel of the radial basis function and the AWEI index were combined. Also, the AWEI index had the highest classification accuracy in the sigmoid kernel. But in the linear kernel, the NDWI index had the highest classification accuracy, which was slightly higher than the AWEI index. But overall, RBF kernel with AWEI index provided higher accuracy than other combinations.

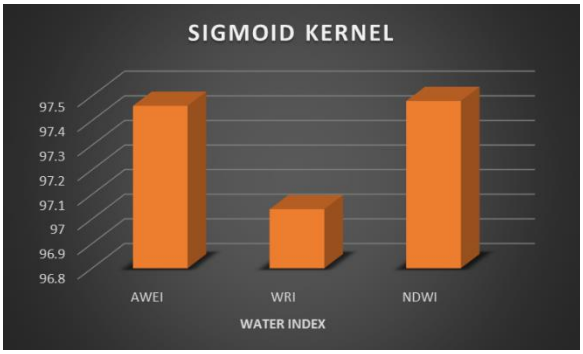

Figure 9. Overall accuracy in sigmoid kernel

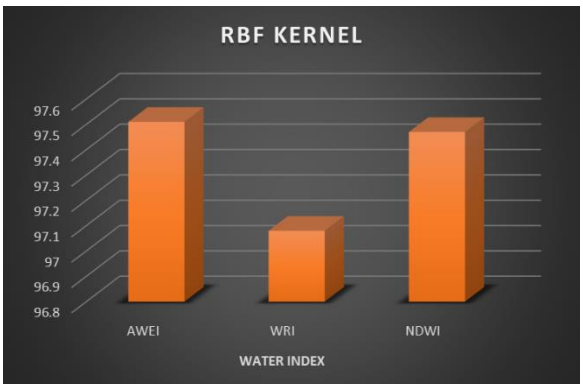

Figure 10. Overall accuracy in RBF kernel

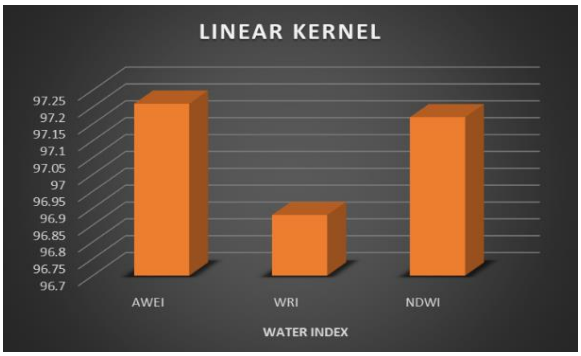

Figure 11. Overall accuracy in linear kernel

In the classification of images, all the combinations of indices and different kernels of the support vector machine worked close to each other in terms of classification accuracy, but visually, especially in sensitive points such as water channels and points where it was difficult to distinguish whether that part of the image is water or land, the kernel of the radial basis function Along with the AWEI index, they provided a very good performance. It is noteworthy that the extent of the studied area had a positive effect on the convergence of the figures that indicated the classification accuracy in the image. If the studied area covered a smaller and more diverse range of classification classes, the figures related to classification accuracy would be subject to more and more different changes.

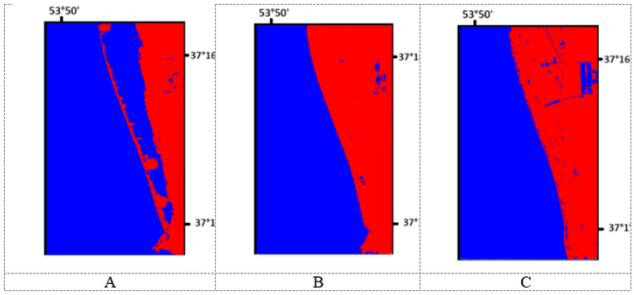

Figure 12. Classified images for study area: (A: 2014, B: 2017 C: 2023)

It can be seen in Figure 12 that with the retreat of Caspian lake water, the coastal wetland has disappeared and turned into a barren land. Also, in 2023, it can be seen that shrimp farms have been built in the east of the study area.

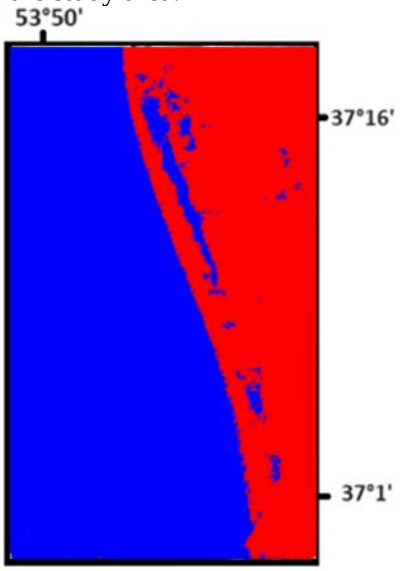

Figure 13. Classified images for study area in 2018

Figure 13 also shows the situation of the studied area in 2018. This year, a flood surrounded the study area and caused some of the water to be discharged into the coastal lagoon.

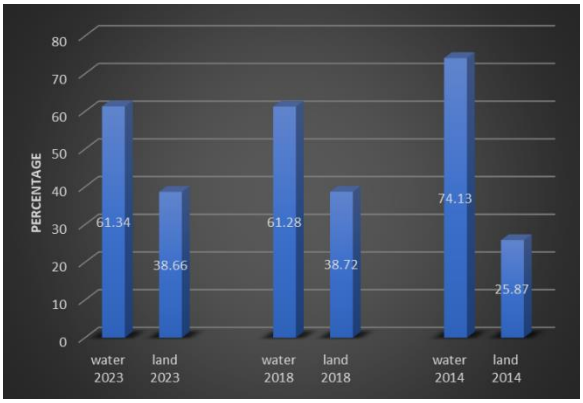

Figure 14. Classified images for study area in 2018

Figure 14 shows the ratio of land and water area of the study area in the beginning and end of the research and

in 2018 when the area was flooded. It is clear that the decrease of the water level has been very intense and the geographical slope of the region is also very low. As a result, the coastal wetland dried up quickly within a few years.

Considering the extensive and general capabilities of MIKE software in the field of monitoring coastal areas such as bays, estuaries and coastal wetlands, a part of this research was devoted to the investigation of the studied area with the help of MIKE software. Which is presented in the following text.

In order to more accurately evaluate the changes in the study area and analyze the main reason for the change in the Gomishan wetland, marine data related to depth, wind, current and waves were prepared from the Ports and Maritime Organization. Then the data was modeled and evaluated. In order to start the modeling process in the marine sector, it is necessary to prepare marine data. The studied environment was meshed and then the bathymetry file was prepared from the target area in the years 2000 and 2022. Then the water depth specifications and other parameters were introduced to the system.

According to the modeling results, the maximum wave period in the offshore area is about 7 seconds and in the coastal area is about 3 seconds. According to the results of the wave propagation model from the deep water area to the coastal area and due to the very gentle slope of the bed in the area, the waves break before reaching the coastal strip. As mentioned earlier, it takes more than 3 kilometers from the sea to reach a depth of 3 meters, and therefore the waves break at a distance far from the beach and the location of the lagoon, and as expected, the current speed caused by the wave in The area of the lagoon is very small. This very low speed does not have the capacity to carry many sediment particles. The evaluations showed that there is currently no possibility of major sedimentation in the studied area, but the decrease in the water level of the Caspian Lake causes drastic changes in the condition of this water area. The monitoring of water bodies, which was discussed during this research, was previously investigated by other researchers (from the current team) and it was mentioned.

Finally, despite the high accuracy of the Mike software, this software sometimes requires accurate data measured in the field. And in the absence of these data, it cannot accurately predict the future conditions of a water body. Therefore, we used the unique capabilities of remote sensing data. Because it covers weak points such as the lack of accurate data. The water body of Gomishan lagoon is one of these cases that have been remotely sensed in this research with the help of satellite data. Remote sensing data provided by Landsat satellites. After processing and implementing the water indicators and combining them with the classification made by the various processing kernels of the support vector machine, two class classification maps were prepared.

6. Conclusions

Monitoring the condition of water areas is one of the important issues in the management of the areas and coastlines of those areas. Until recent decades, monitoring and managing these areas was very difficult and expensive in terms of economics, logistics and time due to the extent of these areas. In recent decades, thanks to the expansion of remote sensing technology and the widespread ease of its use, it helped to manage areas such as water areas. The processing operation for the images of this research, which spanned for a decade, was carried out in the space of Google earth engine. The space of Google earth engine provided the user with fast and accurate processing capabilities. The association of image bands with water indices, which were introduced in order to extract blue areas in the image, greatly improved the quality of image classification. In all the reviewed approaches, the index or processing kernel was different from each other. During this research, NDWI, AWEI and WRI indexes were evaluated with the help of RBF, SIGMOID and LINEAR kernels. The output results were very close. But in all approaches, the AWEI index provided higher accuracy with the help of the RBF processing kernel in the support vector machine.

Finally, the final approach that had the most accuracy among other approaches was selected. And the comprehensive capabilities of this method for monitoring wide study areas were revealed. It was also revealed that the changes and drying of this water area occurred due to the decrease of the water level. For future researches, it is better to use this method to study areas with similar scale but with different depth, such as bays and lakes, which were affected by water level changes.

8. References

[1] Sarp, G., & Ozcelik, M. (2017). Water body extraction and change detection using time series: A case study of Lake Burdur, Turkey. *Journal of Taibah University for Science*, *11*(3), 381-391.

[2] Dezvareh, R. (2019). Application of Soft Computing in the Design and Optimization of Tuned Liquid Column–Gas Damper for Use in Offshore Wind Turbines. *International Journal Of Coastal, Offshore And Environmental Engineering (ijcoe)*, *4*(4), 47-57.

[3] Demir, B., Bovolo, F., & Bruzzone, L. (2012). Updating land-cover maps by classification of image time series: A novel change-detection-driven transfer learning approach. *IEEE Transactions on Geoscience and Remote Sensing*, *51*(1), 300-312.

[4] Salmon, B. P., Kleynhans, W., Van den Bergh, F., Olivier, J. C., Grobler, T. L., & Wessels, K. J. (2013). Land cover change detection using the internal

covariance matrix of the extended Kalman filter over multiple spectral bands. *IEEE Journal of selected topics in applied earth observations and remote sensing*, *6*(3), 1079-1085.

[5] Jawak, S. D., Kulkarni, K., & Luis, A. J. (2015). A review on extraction of lakes from remotely sensed optical satellite data with a special focus on cryospheric lakes. *Advances in Remote Sensing*, *4*(3), 196-213.

[6] Dezvareh, R., & Shafaghat, M. (2020). Predicting the sediment rate of Nakhilo Port using artificial intelligence. *International Journal Of Coastal, Offshore And Environmental Engineering (ijcoe)*, *5*(2), 41-49.

[7] Munizaga, J., García, M., Ureta, F., Novoa, V., Rojas, O., & Rojas, C. (2022). Mapping coastal wetlands using satellite imagery and machine learning in a highly urbanized landscape. *Sustainability*, *14*(9), 5700.

[8] Avcı, C., Budak, M., Yağmur, N., & Balçık, F. (2023). Comparison between random forest and support vector machine algorithms for LULC classification. *International Journal of Engineering and Geosciences*, *8*(1), 1-10.

[9] Zhao, Z., Islam, F., Waseem, L. A., Tariq, A., Nawaz, M., Islam, I. U., ... & Hatamleh, W. A. (2024). Comparison of three machine learning algorithms using google earth engine for land use land cover classification. *Rangeland Ecology & Management*, *92*, 129-137.

[10] Ge, G., Shi, Z., Zhu, Y., Yang, X., & Hao, Y. (2020). Land use/cover classification in an arid desert-oasis mosaic landscape of China using remote sensed imagery: Performance assessment of four machine learning algorithms. *Global Ecology and Conservation*, *22*, e00971.

[11] Leslie, C. R., Serbina, L. O., & Miller, H. M. (2017). *Landsat and agriculture—Case studies on the uses and benefits of Landsat imagery in agricultural monitoring and production* (No. 2017-1034). US Geological Survey.

[12] Li, W., Du, Z., Ling, F., Zhou, D., Wang, H., Gui, Y., ... & Zhang, X. (2013). A comparison of land surface water mapping using the normalized difference water index from TM, ETM+ and ALI. *Remote Sensing*, *5*(11), 5530-5549.

[13] Feyisa, G. L., Meilby, H., Fensholt, R., & Proud, S. R. (2014). Automated Water Extraction Index: A new technique for surface water mapping using Landsat imagery. *Remote sensing of environment*, *140*, 23-35.

[14] Akbari, E., Alavipanah, S. K., Jeihouni, M., Hajeb, M., Haase, D., & Alavipanah, S. (2017). A review of ocean/sea subsurface water temperature studies from remote sensing and non-remote sensing methods. *Water*, *9*(12), 936.

[15] Dodangeh, P., Ebadi, H., & Kiani, A. (2021). Identification of flooded areas using time series statistical calculations and based on integrating radar and optical data. *Iranian journal of Ecohydrology*, *8*(3), 623-639.

[16] Karimi, M., Vali Samani, J. M., & Mazaheri, M. (2018). Evaluating the Hydrodynamic and Morphology of Sefidroud River Delta Using 2D Simulation and Remote Sensing Data. *Journal of Oceanography*, *9*(33), 1-12.

[17] Chegoonian, A. M., Mokhtarzade, M., Valadan Zouj, M., & Bolouki, M. (2016). Accuracy assessment of the coral reef mapping using landsat-8 imagery-Case study: Persian Gulf. *Journal of Oceanography*, *6*(24), 85-93.

[18] Fallah, M., & Fakheran Isfahani, S. (2016). Impacts of Land Use Changes on Water Quality of Anzali International Wetland. *Journal of Oceanography*, *6*(24), 53-59.

[19] Naimaee, R., Kiani, A., Jarahizadeh, S., Haji Seyed Asadollah, S. B., Melgarejo, P., & Jodar-Abellan, A. (2024). Long-Term Water Quality Monitoring: Using Satellite Images for Temporal and Spatial Monitoring of Thermal Pollution in Water Resources. *Sustainability*, *16*(2), 646.

[20] Farhadi, H., Ebadi, H., Kiani, A., & Asgary, A. (2024). A novel flood/water extraction index (FWEI) for identifying water and flooded areas using sentinel-2 visible and near-infrared spectral bands. *Stochastic Environmental Research and Risk Assessment*, 1-23.

[21] Ebadi, H., & Kiani, A. (2022). Integration of remote sensing and meteorological data to predict flooding time using deep learning algorithm. *Engineering Journal of Geospatial Information Technology*, *10*(2), 19-38.

[22] Dodangeh, P., Ebadi, H., & Kiani, A. (2021). Flood change detection with emphasis on high level automation of image interpretation and based on automatic production of training data.

[23] Tatian, M., Mottahedi, S., Tamartash, R., & Akbarlou, M. (2019). Investigation of Vegetation and Land Use Changes in International Gomishan Wetlands Area. *Environmental Researches*, *10*(19), 107-116.

[24] Qureshi, S., Alavipanah, S. K., Konyushkova, M., Mijani, N., Fathololomi, S., Firozjaei, M. K., ... & Kakroodi, A. A. (2020). A remotely sensed assessment of surface ecological change over the Gomishan Wetland, Iran. *Remote Sensing*, *12*(18), 2989.

[25] Pirali Zefrehei, A. R., Hedayati, S. A., & Sahraei, H. (2022). Long-term dynamic analysis based on Landsat imagery in the Gorgan Bay-Gomishan Wetland, Iran. *Caspian Journal of Environmental Sciences*, *20*(4), 721-727.

[26] Khoshravan, H., Poursafari Yekrang, P., & Alemi Safaval, P. (2023). Caspian rapid Sea level fluctuation and intensity of shorelines displacement in the Gomishan Lagoon. *International Journal Of Coastal, Offshore And Environmental Engineering (ijcoe)*, *8*(2), 48-55.

[27] Barzegar, M., Ebadi, H., & Kiani, A. (2015). Comparison of different vegetation indices for very high-resolution images, specific case UltraCam-D imagery. *The International Archives of the Photogrammetry, Remote Sensing and Spatial Information Sciences*, *40*, 97-104.

[28] Shafaghat, M., & Dezvareh, R. (2021). Support vector machine for classification and regression of coastal sediment transport. *Arabian Journal of Geosciences*, *14*(19), 2009.

INTERNATIONAL JOURNAL OF
COASTAL, OFFSHORE & ENVIRONMENTAL ENGINEERING IJCOE Vol.9/No. 1/Winter 2024 (67-78)

Available online at: www. Ijcoe.org *Manuscript Type: Original Research Article*

Analysis of the efficiency of crisis management of local communities in the face of floods due to climate change: five selected villages of port Chabahar County, Iran

Mortaza Tavakoli[1], Ali Mokhtari Karchegani[2*]

[1] Associate Professor, Department of Geography and Rural Planning, Faculty of Humanities, Tarbiat Modares University, Tehran, Iran.
[2] PhD student, Department of Geography and Rural Planning, Faculty of Humanities, Tarbiat Modares University, Tehran, Iran; Lecturer in the Department of Spatial planning, Chabahar University, Chabahar, Iran. Member of the board of the Iranian Rural Development Association; Ali_Mokhtari@Modares.ac.ir*

ARTICLE INFO

Article History:
Received: 09 Oct. 2023
Accepted: 29 Jan. 2024

Keywords:
Crisis management of local communities
Floods, climate changes
Selected villages of port Chabahar County

ABSTRACT

The threat of natural hazards in urban areas is normally addressed through land-use zoning and building regulations. The phenomenon of climate change forces rural planners to devise comprehensive measures to conform to common and greater excessive hazards. This paper discusses the capabilities mainstreaming of resilience in disaster in local development programs as a trendy comparative measure. Therefore, the motive of this article is to assess the responsiveness of the crisis management system of local communities in 5 selected villages of port Chabahar County which will deal with floods due to climate change. The current research is written primarily based totally on the descriptive-analytical approach, which is used to acquire the records of the usage of the questionnaire field method. The contributors encompass 380 humans from the local community of 5 selected villages of port Chabahar County, who had been randomly decided on. The findings of the study display that the resilience additives of settlement communities are at a low level, and the foundation of this situation should be especially discovered inside the weak point of rural disaster management. The three predominant indicators representing the resilience components of residential communities are sensitivity to flood risks with a minimum rating of 0.85 discount of exposure to risk and consequences of floods with a minimum score of 0.76 and increased adaptability of selected rural settlements with a minimal rating of 0.72. Therefore, the findings of the study imply the existence of significant gaps in the planning system of rural settlements in the face of floods, which calls for the adoption of multilateral measures.

1. Introduction

Climate change is one of the major elements in inflicting heavy rainfall on a planetary scale, which has introduced negative floods and has immediately and in a roundabout way, affected nearly all nations in any respect ranges of development [1]. According to the United Nations report [2], more than 3351 coastal regions were identified, of which 64% are uncovered to flood dangers as a result of weather change. Most of those regions are a mixture of rural and concrete regions that don't have the right plans or measures to cope with disasters caused by climate change[3]. Interestingly, a huge variety of folks are afflicted by its bad consequences stay in rural regions in less advanced countries [4]. Rural communities in developing countries are closely laid low with floods because of their excessive dependence on rain fed agriculture and their restrained ability to reply to weather-associated disasters [5]. Rural groups are in particular at risk of those dangers because they rely on herbal resources, restricted infrastructure, and socio-monetary constraints, so that floods resulting from weather alternate have devastating outcomes on the livelihoods of rural communities [6]. These results are multifaceted and large and affect now no longer simplest the short-term monetary

wellness of villagers but additionally their long-time period resilience and capacity to conform to dynamic environmental conditions [7].

Since rural groups depend closely on agriculture, floods can spoil crops, livestock, and infrastructure [8], [9], [10]. Also, lack of earnings and livelihood can result in food insecurity, growth in poverty, and social unrest [11] [12] in a manner that its social effects can cause displacement of the population, lack of social networks, and growth in social vulnerability. Considering this fact, lowering the damage resulting from floods has usually been one of the issues of human societies [13]. This is regardless of the reality that the problem of flood and its control and harm discount has now no longer been given severe interest inside the country and most effective whilst a detrimental flood happens and a catastrophe happens, the eye of officers and specialists is attracted to it [14], [15].

Based on its natural geography, Iran has usually been subjected to natural disasters including landslides, earthquakes, droughts, and floods [14].

Based on its natural geography, Iran has usually been subject. Chabahar region reviews variable annual rainfall, which performs a tremendous function in the incidence of floods. Consequently, the vulnerability of Chabahar villages to floods because of climate change is a pressing concern [16]. According to the announcement of the National Meteorological Organization, the average annual rainfall in the region has reached 110 mm, in line with reports that have broken the past 40 years' precipitation record. This approach that the province is the maximum critically affected [17]. In recent years, this region has confronted common and devastating floods that have had great economic, social, and environmental effects [18].

According to the statistics of the International Organization of the Red Cross Society, in the last flood of the Chabahar region in 2024, greater than 109 villages have been involved, which affected 11/251 households, which have been equal to 56/255 people. Also, in the first days of the flood, electricity turned into reduced in 73 villages, 69 roads in towns and rural areas have been blocked, more than 20 irrigation canals in the village network have been damaged, the telecommunication system was cut and plenty of homes and agricultural infrastructures have been destroyed. The financial losses resulting from floods in Sistan and Baluchistan had been significant. Recent floods have reportedly precipitated greater than $10 million in damage, usually affecting roads, agricultural fields, and home infrastructure [19]. The floods have also blocked rural roads, destroyed homes, and displaced thousands of people, causing economic losses to agricultural fields, aqueducts, roads leading to farms, livestock units, and fish hatcheries [18]. These damages aren`t constrained to monetary and non-bodily components and encompass social components also.

The social consequences of the flood on this place were enormous and feature brought about a lack of life, and as a minimum 8 human beings were killed inside the latest flood. Flooding has additionally affected water supplies, with reviews of water ranges in dams growing because of heavy rains, which can cause additional flooding [20]. Investigations show that the crisis system of the villages of port Chabahar County is referred to as one of the primary elements because of the inefficiency in handling floods. Lack of effective early warning systems, inadequate infrastructure, and limited resources have hampered society's ability to prepare for and respond to floods [21]. Therefore, its miles vital to expand extra powerful control systems, management systems, and infrastructure to lessen the vulnerability of rural groups to floods and grow their resilience to climate-associated disasters. Therefore, rural crisis management systems are a multifaceted process that can help lessen the vulnerability of rural communities to climate hazards including floods with specific measures, research displays that making plans and edition techniques are a powerful component in growing the resilience of prone rural communities [22]. However, the responsiveness of the disaster management system of local communities specifically demanding situations in rural areas stays in a vital vicinity of research. This study aims to assess the potential of the rural planning framework in Sistan and Baluchistan to put together and respond to the growing risk of floods because of climate change. By assessing the strengths, weaknesses, and gaps in the present planning system, this study presents insights to tell more potent and extra-inclusive adaptation strategies that could better defend rural communities in the port Chabahar County in the face of those environmental shocks.

2. Background

To effectively manage flood risks and adapt to the effects of climate change, it is crucial to first assess

vulnerability. Previous research has highlighted the importance of incorporating climate change and vulnerability assessments into environmental impact assessments for sustainable planning and future development [2], [23],[24]. Rural areas are susceptible to natural disasters, including floods, which must be taken into account in rural development planning[25]. The rural areas require significant attention due to the weak physical infrastructure and financial base of the rural people. Maintaining the production of the agricultural sector and investments made is crucial. In case of any natural disasters like floods, there can be severe financial, physical, and environmental losses. Moreover, in the long term, the sustainable livelihood of the villagers will be affected.

Many studies have examined how rural communities adapt to floods caused by climate change, with a focus on the response of local crisis management systems [26]. It is important to incorporate indigenous coping strategies into local development programs to build resilience in the face of disaster Ahmadi [6] identifies social and economic factors as key determinants of vulnerability and calls for political interventions to increase resilience. Neef [27] highlights the importance of access to resources and local socio-cultural contexts in increasing adaptive capacities. Dano, U. L. et al. [28] emphasize the effectiveness of disaster-resilient design strategies in reducing vulnerability in flood-prone areas. These studies emphasize the importance of a comprehensive and community-based approach to flood adaptation planning. Notably, the research literature rarely includes attitudinal vulnerability in multidimensional assessments.

As a result, by providing a framework for multidimensional vulnerability assessment in rural communities located in the study area, this study sought to address this gap. In addition, the research examined how integrating this framework into disaster risk management strategies can increase efficiency and effectiveness (Shrestha et al, 2023). The study and management experiences of different countries reveal that the first step towards reducing flood vulnerability is to assess the vulnerability of households to flood risk so that based on the results and information obtained through flood management, flood mitigation can be achieved by comprehensive rural planning to prevent harmful effects of flooding [29]. Effective rural management systems can provide "local vulnerability reduction programs", a tool used to guide local authority-level physical development in the face of floods. Contemporary rural planning practices are becoming more participatory as they involve stakeholders in decision-making the text emphasizes the importance of increasing the resilience of local areas through strategic interventions that involve stakeholders to understand inherent resilience. Resilience is the natural potential of people, communities, and habitats to cope with and adapt to catastrophic events [30]. When individuals are aware of their vulnerability to hazards, they can minimize exposure to hazards and strengthen social organizations to cope with recurring hazards. This creates inherent resilience[31].

The civil society's indigenous knowledge about the nature of risks and the methods to deal with them displays remarkable resilience. In the presence of various environmental stresses, such as those caused by climate change, the inherent flexibility and adaptability of civil society act as the first line of defense[32]. In other words, when civil society and its organizations are more aware of their vulnerabilities to risks, reduce their exposure, and strengthen their capacity to cope with risks, they become more resilient to environmental stress [33]. As a result, Matthews et al. [34], Chan et al. [35](2023), Shrestha et al. and Miri et al [36] have pointed out the importance of a participatory approach in the crisis management system of local rural communities in the face of natural hazards and the use of indigenous knowledge of inherent resilience in formulating rural planning strategies to adapt to climate change. However, there is a lack of empirical evidence on rural planning practices and products that take inherent resilience into account or improve it through strategic interventions resulting from the participatory rural planning process. Here, local stakeholders include civil society at large, which represents the demand side of disaster risk reduction, village officials in general, and village planners and managers in particular represent the supply side. The demand side of disaster risk reduction is represented by civil society, while the supply side is represented by village officials, particularly village planners and managers. Ahmadi [6] explains that lack of infrastructure capacity, non-resilient and informal settlements, and construction in vulnerable areas make villages in developing countries particularly

vulnerable to climate change disasters. Azizi et al. [14] point out that Climate change has increased the frequency of disasters, putting more pressure on rural planning and local authorities. Effective disaster response requires rural planning that integrates climate change prevention measures. Failure to do so can lead to devastating consequences for communities, making it crucial for local authorities to prioritize this task. Local government officials must understand how climate change disasters affect vulnerable areas and their resilience. In other words, rural planners and managers need to have a deep understanding of vulnerability and resilience issues. This knowledge facilitates effective decision-making processes and helps ensure that the needs of the rural community are met. Planners and rural managers face challenges in addressing the factors influencing climate change and protecting vulnerable communities due to the vagueness of concepts such as risk, vulnerability, and resilience, insufficient knowledge about the processing of relevant data, and the technical complexity of scientific research [12].

3. Methodology

This section explains the details of the study area and the motive for its selection. Port Chabahar County was chosen as the study area. The sampling plan and statistics series technique also are defined in this segment. Finally, the indicators selected for the study and the technique adopted for data analysis are discussed in detail.

3.1 Areas of the Study

Chabahar is a city located in the Sistan and Baluchistan province of Iran. The city is situated at an altitude of seven meters above sea level, at a longitude of 60 degrees and 37 minutes east, and a latitude of 25 degrees and 17 minutes north. This city is located in southeastern Iran and is bordered by Iranshahr and Nikshahr to the north, Pakistan to the east, Oman Sea to the south, and Kerman and Hormozgan provinces to the west. The latest census indicates that Chabahar city includes three districts, six rural districts, and 135 villages. The rural population of Chabahar has 40,918 households and 170,778 people. Chabahar has a moderately tropical climate, which includes relatively high humidity. It is the hottest part of the country in winter and the coldest southern port of Iran in summer. The climate of this city and its surroundings is always mild and spring-like. "That is why it is called Chabahar. The name derives from the fact that all four seasons in this place are like spring."

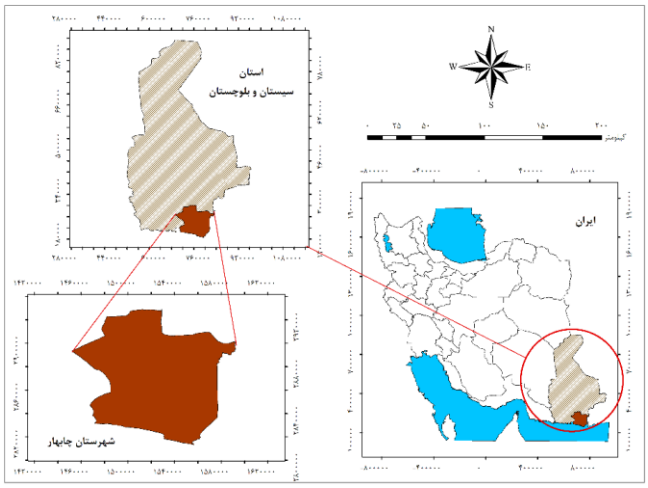

Figure 1. Geographical location of the study area
Source: Authors, 2024

3.2 Method for collecting data

The data collection for this research was done in two stages. The first stage involved library and documentary research, which was used to obtain general information such as definitions and key concepts, the research background, the necessity of the research, description of applications, plans, and indicators, and the theoretical basis. b) This method involves creating questionnaires and interviews, as well as specialized checklists and impressions. Researchers administered a Likert scale questionnaire to collect data from selected villages to determine the statistical population. The five selected villages - Ramin, Owraki Bozorg, Morad Abad, Tis, and Osman Abad - are more vulnerable to floods than other villages in the city and have a larger population. The total population of these villages is 27,525. According to Cochran's formula, the sample size of 380 people was estimated proportionally based on the population of the village and the five selected villages. Also, the participants were selected using a simple random sampling method. A researcher-made questionnaire was used to collect data. An index-based method was used to assess vulnerability. The measurement of vulnerability was based on three components, which are exposure, sensitivity, and adaptive capacity. The indicators were established based on previous studies, and focus group meetings with academic experts and specialists. To weigh the indicators, a questionnaire was prepared by three groups of experts, including university professors, members

of engineering consulting companies, and experts of agricultural jihad. To calculate resilience, it is necessary to express the dimensions of exposure, sensitivity, and adaptive capacity for each sub-index in the range of 0 to 1. Then, using the formula, the total vulnerability was calculated. Cluster analysis was utilized to classify respondents into three groups based on their level of vulnerability: low, medium, and high. In the next step, a one-way analysis of variance was used to identify indicators affecting the vulnerability of rural households .The questionnaire's validity was confirmed by experts. Its reliability was acceptable with a Cronbach's alpha test of 0.84. Data were analyzed using SPSS 20 software.

3.3 Method of Analysis

This research aims to apply the descriptive-analytical method. The analytical framework that was formulated for this study consists of three steps. The initial step was to assess the vulnerability level of rural inhabitants in port Chabahar County by gathering data from respondents' perceptions. To obtain this information, a social survey was conducted using a questionnaire. The survey was conducted in five settlement areas that are most affected by the risk of flooding in the villages of Chabahar (see table 1). The questionnaire not only deals with the vulnerability of the respondents and their houses and properties against flood risks but also with the expectations of the respondents from the management and planning institutions to reduce the vulnerability and improve the resilience of their settlementsIn the second step, the most obvious vulnerability factors were prioritized as well as socio-physical dimensions related to community resilience, based on the responses of the social survey. The findings of steps 1 and 2 were considered on the demand side of disaster preparedness in selected villages of port Chabahar County. For weighting, the weighting method of the average points was used, which was weighted respectively based on the percentage of answers (100% agreement = 1, 75% = 0.75, 50% = 0.50, 25% = 0.25, and 0% = 0, respectively). The ratio Wi/n was calculated using the equation: Wi for the individual weighted score (or 1, 0.75, 0.50, 0.25, and 0) for each question, n is the number of questions) and Wifi/fi for the weighted mean score where Wi is the weighted score and is the frequency of a specific score.

Table 1. Characteristics of the research sample size (statistical population of 2022)

Row	The name of the selected village	population	Population share of the total	number of samples
1	Ramin	3821	13.9	53
2	Owraki Bozorg	1770	6.4	24
3	Morad Abad	12906	46.9	178
4	Tis	6348	23.1	88
5	Osman Abad	2680	9.7	37
Total aggregation		27525	100	380

4. Findings

The analysis of the data presented in this section includes (1) the vulnerability of people and their settlements, (2) socio-physical resilience in the study area, and (3) the response of planners to people's needs to prepare against disasters as reflected in planning interventions.

4.1 Respondents' perceptions of the vulnerability of people and their settlements

Identifying vulnerabilities is a crucial step in increasing the resilience of human settlements against disasters. This article examines the actions that managers and officials of selected villages in Chabahar should take to reduce vulnerability to floods. This index is utilized to measure the degree of vulnerability and sustainability of rural communities. During the survey, participants were presented with a list of possible reasons for making their habitat more resilient. These reasons were selected from theoretical literature on the subject. Table 3 displays the top reasons mentioned by respondents for a multiple-choice question. The responses were weighted using a five-point Likert scale, ranging from strongly agree to strongly disagree. Based on the survey results, the main reason why the villagers consider relocating is the challenges they face during floods. Specifically, the disruption of roads, public transport services, and private vehicles during floods makes life difficult for them. Nearly 63% of the respondents reported that obtaining necessities like food and clean drinking water was extremely problematic during floods. Their ability to move around and access daily essential items is severely impacted due to the breakdown of infrastructure and transportation facilities. The weighted mean score (WMS) for reason number 1 is 0.86 points. This

score indicates that if local authorities fail to address the increasing frequency and intensity of flood hazards and their impact, most respondents will choose to relocate to a different area.

The respondents' answers were used to calculate a weighted average of the scores, which highlights the priority actions that the authorities should take. A weighted mean of 0.75 or higher suggests that authorities should prioritize (1) improving public and private transportation in rural areas, (2) addressing severe flooding in residential areas, and (3) mitigating the fear of loss of life due to flooding by implementing appropriate planning and developmental interventions. Although the reduction of security and environmental health was mentioned in the questionnaire, it was not among the top five reasons for the relocation of villagers. More than 54% of respondents cited the loss of property value, asset value, and reduced agricultural productivity as the primary reasons for migration. During flooding in selected villages of Chabahar, the low quality of life and unfavorable economic conditions have convinced people to seek relocation. This has made the villagers vulnerable and officials have a responsibility to protect their assets and lands. It is important to help them continue their livelihood and gain the trust of civil society by devoting all efforts towards this cause.

Table 2. vulnerability against flood risks and relocation reasons

Row	Reasons to move to a safer area	(%100 = 380 = total) Participant					weighted average score (WMS)
		I Strongly (0) disagree	I Disagree (0.25)	No idea (0.50)	I agree0.7 (5)	I Strongly (1) agree	
1	Disruption of village infrastructure and services	4	15	34	87	239	0.86
2	severe flooding in residential areas	6	8	11	93	262	0.89
3	Disruption of private and public transportation	9	8	15	67	281	0.90
4	loss of value of property and assets	14	15	24	87	239	0.84
5	Reducing the sense of security and environmental health	19	49	65	27	220	0.75
6	Disruption of earning opportunities	15	57	19	53	236	0.79
7	fear of loss of life	0	27	17	87	249	0.87
8	reduced productivity of agricultural land	8	19	15	133	205	0.84

According to Table 2, the participants did not show a significant difference in their perception of the vulnerability aspects of the selected rural areas of Chabahar. However, some aspects were given priority with a slight difference. The respondents expressed their greatest concern about the physical aspects of vulnerability. Then, the psychological aspect such as the fear of losing one's life was the next priority. According to a recent study, economic factors such as loss of income and decrease in agricultural productivity are not the primary reasons for displacement due to floods. Instead, respondents believe that the physical weaknesses in their village planning and infrastructure make their settlements vulnerable to floods. This suggests that they may not have confidence in the resilience of their village economic systems against natural disasters. The residents are aware that their settlements are situated in an area that is prone to flooding. However, they believe that they cannot control the physical effects of vulnerability, and therefore, they expect local officials and planners to play an important role in making the village a safe place. As a result, adapting to disasters should mainly focus on safeguarding vulnerable areas and elements of the villages. Local and provincial authorities should prioritize physical adaptations for settlements to reduce vulnerability and strengthen resilience against flood disasters.

4.2 Analysis of Physical-Social Aspects of Resilience

The social survey aims to gather opinions from respondents about their needs to improve their resilience through rural management planning and interventions. Although villagers may have various needs to enhance their flood resilience, the analysis only considers the views of rural planners. Providing hazard awareness programs for villagers is considered the direct responsibility of local management and not planners. For the analysis, we excluded such needs. In Table 4, the findings were grouped into three dimensions of resilience:

sensitivity to risk, reducing exposure, and increasing adaptive capacity.

4.3 Susceptibility to flood hazards

According to Table 3, the results indicate that 73% of the participants desire rural planners and managers to prioritize risk reduction measures for housing, transportation, infrastructure, and facilities based on the level of risk in each village. They also expect them to be sensitive to the system's needs and make it their priority. Currently, the crisis management structure in the selected villages of Chabahar is inadequate during times of emergency. As a result, the village of Kamb Morad Abad, which is one of the most populous villages in the country, is lacking a village head. According to the survey, the respondents believe that a management system should be in place at the rural district level to assist during times of crisis. This finding is consistent with the concern expressed in Table 2, where severe flooding and residential destruction were identified as the most vulnerable aspects during floods. The survey participants highlighted the importance of ensuring risk mitigation measures are in place for every critical aspect of the village. This includes the provision of rescue routes and emergency evacuation plans, as well as the need for prompt action and timely warnings to raise awareness and ensure the safety of residents in each area.

Table 3. The respondents need resilience improvement

Row	Susceptibility of villagers and planners to flood hazards	Respondent (total = 380 = 100%)					weighted average score (WMS)
		I don't need (0) strongly	I don't need (0.25)	I have no idea (0.50)	I need (0.75)	I strongly need (1)	
1	The need for an emergency rescue and evacuation route system in the village	0	15	16	64	285	0.91
2	Need for risk mitigation measures for housing, transport, infrastructure, and facilities	0	0	26	75	279	0.92
3	Prioritize "safer and safer environments" as a goal for local plan development	0	7	14	102	257	0.90
4	The need to regulate land development according to the level of risks	0	8	34	141	198	0.85

The research suggests that rural officials, as well as village heads, need to be more sensitive to the needs of the villagers to reduce the risks of disasters. However, the findings show that the efforts made by authorities so far have not been satisfactory to the villagers. This dissatisfaction is indicated by an average score of more than 0.66. The descending order of the hierarchy of sensitivity-needs also shows that villagers prioritize risk reduction needs related to housing, transportation, infrastructure, and water and electricity services through effective interventions to integrate risk reduction in targeting and implementing the development plan. The need for land regulation based on the level of risks due to construction records and village population growth has the lowest priority.

4.4 Reducing exposure to flood risk and impacts

During the resilience assessment, the second dimension that was evaluated was the reduction of exposure of villagers and their settlements to the risks and effects of floods. The survey respondents recognized the significance of relocating the construction of residential, industrial, and commercial buildings to safer areas. This is considered one of the crucial needs that rural planners should address to minimize the risk to residents. During disasters, public schools and gymnasiums are often used as evacuation sites and temporary shelters. However, victims face numerous issues due to the lack of available facilities to accommodate them during floods. It has been found that the current public schools are facing issues related to the quality of construction and lack of sufficient space for temporary accommodation. Moreover, these schools lack the necessary facilities for civic purposes.

Respondents have expressed the need for social facilities such as multi-purpose halls like sports halls. These facilities can be utilized during natural disasters effectively without disrupting their primary use.

Table 4. Responders need to improve resilience.

Row	Reducing exposure to flood risk and impacts through planning and development interventions	Respondent (total = 380 = 100%)					weighted average score)WMS(
		I don't need strongly) 0(	I don't need)0.25(	I have no idea) 0.50(	I need)0.75(	I strongly need (1)	
5	Providing social facilities for use as evacuation centers and temporary shelters	0	42	29	33	276	0.86
6	Limit the construction of residential, industrial, and commercial buildings to safer areas	0	0	14	61	305	0.94
7	Regular maintenance of drains, canals, and embankments	4	19	14	147	196	0.84
8	Construction of new flood and water storage ponds	0	53	26	124	177	0.78
9	Recommending protection measures for property and buildings	2	51	76	94	157	0.76
10	Protection of natural slopes, structures, and waterways	54	65	55	53	153	0.62

This finding supports the findings in Table 2, which identify the destruction of living and working areas as a primary factor contributing to residents' vulnerability to flood risks. Therefore, residents are looking for more practical solutions to minimize exposure. This finding supports Table 2, identifying the destruction of living and working areas as a key factor in residents' vulnerability to floods. The local planning authority is expected to take stricter measures to limit construction in flood-prone areas and strengthen defenses through new embankments and drainage channels. An interesting finding is the expectations of residents from planners. This means taking appropriate measures to protect property and buildings. For example, reacting to the selfish actions of some people, such as raising the ground, which increases the vulnerability of their neighbors. This finding implies that rural planners and managers should develop appropriate construction techniques and retrofitting measures to help residents adapt to future climate change floods.

4.5 increasing the adaptation capacity of settlements

The third aspect of resilience was the ability of rural settlements to adapt. As mentioned earlier to reducing the risk of exposure, the respondents believed that the planners and village managers of port Chabahar County should prioritize "enhancing infrastructure, water, and electricity networks for disaster resistance." While rural leadership plans are supposed to allocate a significant portion of land for open spaces and public places, a recent study suggests that the current distribution of land use in certain villages does not meet the public's requirements. Moreover, the respondents of the survey expect that the zoning plan will display hazard zoning maps based on the level of danger. While rural leadership plans aim to reserve a suitable portion of land for open spaces and public areas, a recent study indicates that the current distribution of land use in certain villages does not adequately cater to public demands. Furthermore, the respondents anticipate that the zoning plan will display hazard zoning maps corresponding to the degree of danger.

Table 5. Responders need to improve resilience.

Row	Improving the adaptive capacity of settlements through development planning and interventions	Respondent (total = 380 = 100%)					weighted average score (WMS)
		I don't need strongly (0)	I don't need)0.25(	I have no idea (0.50)	I need (0.75)	I strongly need (1)	
11	Allocation of land for public use for emergency use	17	64	38	97	164	0.72
12	Showing hazard rating measures in the zoning plan (disaster awareness)	0	26	54	184	116	0.76
13	Increasing access to perform daily activities (work, school, business, etc.)	4	28	72	112	164	0.77
14	Improving infrastructure and water and electricity networks to resist hazards	0	0	0	123	257	0.92
15	Establishing laws and regulations in the field of disaster reduction	3	15	64	143	155	0.78
16	Incorporating indigenous knowledge of coping strategies into the local plan	11	34	54	96	185	0.77

According to the results, two key areas require improvement with a weighted mean score exceeding 0.66. These are enhancing accessibility and fortifying flood resilience of rural infrastructure and services. These measures are essential to mitigate the impact of floods induced by climate change in the study regions. However, these measures have not been taken into consideration by the planners of the selected villages of Chabahar. Interestingly, the respondents support showing hazard rating measures in the zoning plan (disaster awareness) with a weighted mean score of 0.76 and introducing specific rules and regulations for disaster preparedness with a weighted mean score of 0.78. This finding indicates that individual adaptation measures are being carried out in an extreme manner that endangers the safety of neighbors as well as the community. According to the responses received, it appears that enforcing strict command and control measures can be an effective approach to prevent individual selfish actions. Additionally, the respondents emphasized the need for planners to be well-versed in local wisdom and indigenous knowledge to better handle hazards and to incorporate these forms of knowledge into their planning processes.

5. Discussion

This study has focused on assessing the response capabilities of local communities in five selected villages of port Chabahar County to manage crises caused by floods resulting from climate change. The results indicate that the resilience of these rural settlements is significantly affected by the inadequacy of their planning system. As a result, their crisis management strategies are in a critical state, and they are unable to respond effectively in critical situations. The management system's policies and strategies for dealing with natural hazards, particularly floods, lack a systematic structure that fails to consider flood risk sensitivity, reduce risk exposure, and increase settlement adaptation. An analysis of the physical and social dimensions of resilience reveals that the local crisis management system overlooks some critical needs of the villagers in its programs. It came as a surprise that the planners had failed to take adequate measures to ensure vital resilience needs such as determining rescue and evacuation routes and implementing risk reduction measures for housing, transportation, infrastructure, and facilities. This lack of action was due to their insensitivity towards flood risk. The findings mentioned are consistent with the studies conducted by Alves et al. in [37], which highlight the importance of having proper infrastructure systems, such as transportation, to reduce the risk of flooding and enhance the flexibility of settlements. Moreover, it is essential to recommend flood protection measures for individual buildings and properties, which have been overlooked by planners. On the other hand, traditional planning measures like determining the planning goals and constructing buildings outside the danger zone are more effective than developing constructions beyond village boundaries and protecting natural ranges. According to a study conducted by JM Bodoque [38], complying with safety regulations and construction rules in rural settlements is crucial for crisis management systems to enhance resilience during floods. The research findings suggest that local planners and managers in the surveyed villages must organize themselves and expand their efforts to minimize rural settlements' vulnerability to natural hazards, such as floods. Increasing knowledge and cooperation between local and extra-local institutions is necessary to make studied communities resilient against natural disasters. This can be achieved by implementing principles that improve the crisis management system of settlements. However, there is a need to incorporate local knowledge of strategies to deal with flood risks in their plans, which has not been given due attention. It has been inferred that over 70% of the respondents believe that indigenous knowledge should be considered an important factor in development plans related to hazard preparedness. It has been observed that local plans have completely ignored indigenous knowledge. This discovery relates to a significant flaw in the follow-up of the participatory planning process that involves local stakeholders. It appears that this flaw is due to the lack of institutionalization of local management institutions. Overcoming this inadequacy is challenging until the planning and institutional capacity at the local level is strengthened. Adapting to hazards caused by climate change at the local level requires the use of indigenous knowledge. Furthermore, this discovery confirms the studies of Harahap [39]; These researchers emphasize that there is a need to include resilience in disaster into local planning practices, as vulnerability reduction and adaptation cannot be achieved by addressing climate change

alone. Vulnerability reduction appears to be the best motion when combined with other planning strategies at the local level. From the point of view of participation in rural planning methods in response to climate change, the study in five villages of port Chabahar County strengthens the argument that resilient rural planning measures should be formulated according to the needs of local people in developing countries and should not be expected to implement physical programs on a larger scale or plan an inter-level structure to guide actions at the local level. This study showed that the local development plan prepared by the federal-level planners was not effective enough to reduce the vulnerability and improve the resilience of the local people in the five villages of Chabahar. A local development plan without the participation of stakeholders and local knowledge will certainly not be very effective. Therefore, this paper calls for the strengthening of participatory planning and capacity development of local authorities to more decisively mainstream disaster resilience in local development plans.

6. Conclusion

Given that villages contribute very little to greenhouse gas emissions, adaptation measures should be prioritized over measures aimed at reducing emissions. The long-term resilience of rural communities heavily relies on their ability to adapt and recover after floods. To reduce the vulnerability of local communities, adaptation strategies such as early warning systems, flood-resistant infrastructure, and legal and institutional measures against floods can be implemented. However, the effectiveness of these strategies depends on the availability of resources, the capacity of local governments, and the participation of local communities. Therefore, adapting to global climate change requires relevant and effective local measures. Local adaptation measures should be integrated with existing hazard preparedness measures, rather than being separate and exclusive measures. When adaptation to climate change becomes part of general hazard preparedness measures in a local development planning process, it is automatically included in the development plan. Sectoral structured development programs tend to ignore cross-cutting issues such as disaster preparedness and climate change adaptation or divide them into specific development sectors such as housing and social welfare. This study demonstrated that the failure to institutionalize the crisis management principles of local communities is the main reason for the physical, social, and economic resilience of the settlements of port Chabahar County. Therefore, this article recommends that a prerequisite for resilient settlement construction in these areas is the institutionalization of local crisis management systems. Local development should be prepared based on the important issues facing civil society in the respective area. Indigenous knowledge should be the basis of such local development programs.

To improve the responsiveness of the local crisis management system in the face of floods caused by climate change, it is suggested that the management institutions of the rural planning system be effective in responding to natural disasters such as floods, measures such as creating a system of rescue routes and emergency evacuation in villages, implementing risk reduction measures for Prioritize housing, transportation, infrastructure, and facilities, and prioritize the creation of safer and more secure environments in local development plans. Also, to increase the physical resilience of rural settlements put the zoning policies of risk areas and adhere to them in new constructions effectively. On the other hand, the use of rural social capacities to improve the adaptation capacity of the settlement, such as integrating programs with local knowledge and creating a collaborative environment in preparing programs, should be put on the agenda. Finally, these measures help to improve the adaptive potential of rural settlements to discount the risks of floods caused by climate change.

7. References

[1] Jerin, T., Azad, M. A. K., & Khan, M. N. Climate change-triggered vulnerability assessment of the flood-prone communities in Bangladesh: A gender perspective. *International journal of disaster risk reduction*, *95*, 103851. (2023)

[2] Udie, J., Bhattacharyya, S., & Ozawa-Meida, L. A conceptual framework for vulnerability assessment of climate change impact on critical oil and gas infrastructure in the niger delta. *Climate*, *6*(1), 11. (2018)

[3] Ghosh, M., & Ghosal, S. Climate change vulnerability of rural households in flood-prone areas of Himalayan foothills, West Bengal, India. *Environment, Development and Sustainability*, *23*, 2570-2595. (2021)

[4] Gaisie, E., & Cobbinah, P. B. Planning for context-based climate adaptation: Flood management inquiry in Accra. *Environmental Science & Policy*, *141*, 97-108. (2023)

[5] Jamshed, A., Birkmann, J., Feldmeyer, D., & Rana, I. A. A conceptual framework to understand the dynamics of

rural–urban linkages for rural flood vulnerability. *Sustainability, 12*(7), 2894. (2020)

[6] Ahmed, Y., Jamil, M., & Ashraf, M. Z. Monitoring & Evaluation Matrix For Disaster Risk Reduction In Rural Settlements Of Punjab-An Analysis Of Economic & Land Use Enclaves. *Webology, 19*(2). (2022)

[7] Islam, M. M., Ujiie, K., Noguchi, R., & Ahamed, T. Flash flood-induced vulnerability and need assessment of wetlands using remote sensing, GIS, and econometric models. *Remote Sensing Applications: Society and Environment, 25*, 100692. (2022)

[8] Opoku, S. K., Filho, W. L., Hubert, F., & Adejumo, O. Climate change and health preparedness in Africa: analysing trends in six African countries. *International Journal of Environmental Research and Public Health, 18*(9), 4672. (2021)

[9] Musacchio, A., Andrade, L., O'Neill, E., Re, V., O'Dwyer, J., & Hynds, P. D. Planning for the health impacts of climate change: Flooding, private groundwater contamination and waterborne infection–A cross-sectional study of risk perception, experience and behaviours in the Republic of Ireland. *Environmental Research, 194*, 110707. (2021)

[10] Othman, A., El-Saoud, W. A., Habeebullah, T., Shaaban, F., & Abotalib, A. Z. Risk assessment of flash flood and soil erosion impacts on electrical infrastructures in overcrowded mountainous urban areas under climate change. *Reliability Engineering & System Safety, 236*, 109302. (2023)

[11] Yin, J., Yu, D., & Liao, B. A city-scale assessment of emergency response accessibility to vulnerable populations and facilities under normal and pluvial flood conditions for Shanghai, China. *Environment and Planning B: Urban Analytics and City Science, 48*(8), 2239-2253. (2021)

[12] Lu, X., Chan, F. K. S., Chen, W.-Q., Chan, H. K., & Gu, X. An overview of flood-induced transport disruptions on urban streets and roads in Chinese megacities: Lessons and future agendas. *Journal of Environmental Management, 321*, 115991. (2022)

[13] Nourali, Z., Shortridge, J. E., Bukvic, A., Shao, Y., & Irish, J. L. Simulation of Flood-Induced Human Migration at the Municipal Scale: A Stochastic Agent-Based Model of Relocation Response to Coastal Flooding. *Water, 16*(2), 263. (2024)

[14] Azizi, E., Mostafazadeh, R., Hazbavi, Z., et al. Spatial distribution of flood vulnerability index in Ardabil province, Iran. *Stochastic Environmental Research and Risk Assessment, 36*(12), 4355-4375. (2022)

[15] Akbari, M., Neamatollahi, E., Memarian, H., & Alizadeh Noughani, M. Assessing impacts of floods disaster on soil erosion risk based on the RUSLE-GloSEM approach in western Iran. *Natural Hazards, 117*(2), 1689-1710. (2023)

[16] Tavakoli, M., & Mokhtari Karchegani, A. Analysis of factors affecting the structure of rural settlements in Makran coastal region in the face of climate change. *Journal of Oceanography, 13*(52), 131-144. (2023)

[17] Pazhuhan, M., & Amirzadeh, M. Community flood resilience assessment of Saadi neighborhood, Shiraz, Iran. *Journal of Risk Research, 27*(1), 21-45. (2024)

[18] IRCS. The International Federation of Red Cross and Red Crescent Societies (IFRC) and the International Committee of the Red Cross (ICRC). (2020)

[19] https://dolat.ir/detail/445213. (2023).

[20] Miri, M., Raziei, T., Zand, M., & Kousari, M. R. Synoptic aspects of two flash flood-inducing heavy rainfalls in southern Iran during 2019–2020. *Natural Hazards, 115*(3), 2655-2672. (2023)

[21] Zainudini, M. A., & Sardarzaei, A. Flood causes, consequences, protection, measures and management in Kaserkand, Sarbaz and Dashtyari Districts, Makoran, Iran. *Glob. J. Eng. Technol. Adv, 10*, 94-102. (2022)

[22] aMokhtari Karchegani, A., & God bless you, A., Morteza. The pattern of livelihood adaptation of rural communities in Iran in the face of climate change. *Geography and environmental hazards*, -. (2023); bMokhtari Karchgani, A., Tavakoli, M., Barzo, G., & Yar Ahmadi, K. Prospects for smart villages and sustainable territorial development: a bibliometric analysis and systematic review. (2024)

[23] He, H., Li, R., Pei, J., Bilodeau, J.-P., & Huang, G. Current overview of impact analysis and risk assessment of urban pluvial flood on road traffic. *Sustainable Cities and Society*, 104993. (2023)

[24] Ha-Mim, N. M., & Hossain, M. Z. (2022). Application of GIS and AHP-Based Integrated Methodology for Mapping and Characterizing Socioeconomic Vulnerability to Natural Hazards: A Case Study of Southwestern Coastal Bangladesh *A System Engineering Approach to Disaster Resilience: Select Proceedings of VCDRR 2021* (pp. 187-203): Springer.

[25] Yang, D. Y., & Frangopol, D. M. Physics-based assessment of climate change impact on long-term regional bridge scour risk using hydrologic modeling: Application to Lehigh river watershed. *Journal of Bridge Engineering, 24*(11), 04019099. (2019)

[26] Gyekye, K. A., & Darko, P. K. Assessing Community Coping Strategies in Sustainable Flood Management. A Case Study of Kaemibre and Walantu in Kasoa. *Ghana Journal of Geography, 14*(3), 211-251. (2022)

[27] Neef, A. (2021). *Tourism, land grabs and displacement: The darker side of the feel-good industry*: Routledge.

[28] Dano, U. L., Abubakar, I. R., AlShihri, F. S., Ahmed, S. M., Alrawaf, T. I., & Alshammari, M. S. A multi-criteria assessment of climate change impacts on urban sustainability in Dammam Metropolitan Area, Saudi Arabia. *Ain Shams Engineering Journal, 14*(9), 102062. (2023)

[29] Zhang, N., & Alipour, A. Flood risk assessment and application of risk curves for design of mitigation strategies. *International Journal of Critical Infrastructure Protection, 36*, 100490. (2022)

[30] Loli, M., Kefalas, G., Dafis, S., Mitoulis, S. A., & Schmidt, F. Bridge-specific flood risk assessment of transport networks using GIS and remotely sensed data. *Science of the Total Environment, 850*, 157976. (2022)

[31] Waseem, H. B., & Rana, I. A. Floods in Pakistan: A state-of-the-art review. *Natural Hazards Research*. (2023)

[32] Williams, P. A., Simpson, N. P., Totin, E., North, M. A., & Trisos, C. H. Feasibility assessment of climate change adaptation options across Africa: an evidence-

based review. *Environmental Research Letters, 16*(7), 073004. (2021)

[33] Gori, A., Gidaris, I., Elliott, J. R., et al. Accessibility and recovery assessment of Houston's roadway network due to fluvial flooding during Hurricane Harvey. *Natural hazards review, 21*(2), 04020005. (2020)

[34] Matthews, V., Longman, J., Berry, H. L., et al. Differential mental health impact six months after extensive river flooding in rural Australia: a cross-sectional analysis through an equity lens. *Frontiers in public health, 7*, 367. (2019)

[35] Chan, F., Wang, Z., Chen, J., et al. Selected global flood preparation and response lessons: implications for more resilient Chinese Cities. *Natural Hazards, 118*(3), 1767-1796. (2023)

[36] Shrestha, D., Basnyat, D. B., Gyawali, J., et al. Rainfall extremes under future climate change with implications for urban flood risk in Kathmandu, Nepal. *International journal of disaster risk reduction, 97*, 103997. (2023)

[37] Alves, A., Gersonius, B., Kapelan, Z., Vojinovic, Z., & Sanchez, A. Assessing the Co-Benefits of green-blue-grey infrastructure for sustainable urban flood risk management. *Journal of Environmental Management, 239*, 244-254. (2019)

[38] Bodoque, J. M., Amérigo, M., Díez-Herrero, A., et al. Improvement of resilience of urban areas by integrating social perception in flash-flood risk management. *Journal of Hydrology, 541*, 665-676. (2016)

[39] Harahap, G. Y. Instilling Participatory Planning in Disaster Resilience Measures: Recovery of Tsunami-affected Communities in Banda Aceh, Indonesia. *Budapest International Research in Exact Sciences (BirEx) Journal, 2*(3), 394-404. (2020)